國立中山大學材料科學研究所

博士論文

高性能鎂/碳纖/聚二醚酮夾層及奈米粉體強化聚二醚酮複材之製備與特性分析

Fabrication and Characterization on High Performance Mg/Carbon-Fiber/PEEK Laminates and Nanoparticle/PEEK Nanocomposites

研究生：郭木城 撰

指導教授：黃志青 博士

中華民國 九十四 年 一 月

國立中山大學研究生學位論文審定書

本校材料科學研究所博士班
研究生 郭木城（學號：8936805 ）所提論文

高性能鎂/碳纖/聚二醚酮夾層及奈米粉體強化聚二醚酮複材之製備與特性分析

經本委員會審查並舉行口試，符合博士學位論文標準。

學位考試委員簽章：

高伯威教授
國立中山大學材料科學研究所

陳　明教授
國立中山大學材料科學研究所

任明華教授
國立中山大學機械與機電工程學系

呂傳盛教授
國立成功大學材料科學與工程學系

洪伯達教授
國立台灣科技大學高分子工程系

指導教授

黃志青教授
國立中山大學材料科學研究所

所長

曾百亨教授
國立中山大學材料科學研究所

博碩士論文授權書

（國科會科學技術資料中心版本，93.2.6）

本授權書所授權之論文為本人在　國立中山大學　材料科學研究所　九 十 三 學年度第 一 學期取得　博　士學位之論文。

論文名稱：高性能鎂/碳纖/聚二醚酮夾層及奈米粉體強化聚二醚酮複材之製備與特性分析

■同意　□不同意　（政府機關重製上網）

本人具有著作財產權之論文全文資料，授予行政院國家科學委員會科學技術資料中心(或其改制後之機構)、國家圖書館及本人畢業學校圖書館，得不限地域、時間與次數以微縮、光碟或數位化等各種方式重製後散布發行或上載網路。

本論文為本人向經濟部智慧財產局申請專利(未申請者本條款請不予理會)的附件之一，申請文號為：＿＿＿＿＿＿，註明文號者請將全文資料延後半年後再公開。

■同意　□不同意　（圖書館影印）

本人具有著作財產權之論文全文資料，授予教育部指定送繳之圖書館及本人畢業學校圖書館，為學術研究之目的以各種方法重製，或為上述目的再授權他人以各種方法重製，不限地域與時間，惟每人以一份為限。

上述授權內容均無須訂立讓與及授權契約書。依本授權之發行權為非專屬性發行權利。依本授權所為之收錄、重製、發行及學術研發利用均為無償。上述同意與不同意之欄位若未鈎選，本人同意視同授權。

指導教授姓名:黃志青

研究生簽名:　　學號:8936805

(親筆正楷)　　(務必填寫)

日期:民國　94　年　1 月　25　日

---

1. 本授權書（得自http://sticnet.stic.gov.tw/sticweb/html/theses/authorize.html 下載或至http://www.stic.gov.tw首頁右下方下載）請以黑筆撰寫並影印裝訂於書名頁之次頁。
2. 授權第一項者，請確認學校是否代收，若無者，請個別再寄論文一本至台北市(106)和平東路二段 106 號 1702 室　國科會科學技術資料中心　黃善平小姐。(電話:02-27377606　傳真：02-27377689)

TABLE OF CONTENTS

LIST OF TABLES

LIST OF FIGURES

ABSTRACT

Magnesium alloys have attracted considerable attention owing to its low density of ~1.7 g/cm^3. On the other hand, the carbon fiber (CF) reinforced polyether ether ketone (PEEK) polymer composites possess extraordinary specific strength and stiffness along the longitudinal (or fiber) direction. It follows that the combination of Mg/CF/PEEK would offer an alternative in forming a high specific strength and stiffness composite. In the first part of this study, the low density and high performance Mg-based laminated composites were fabricated by means of sandwiching the AZ31 Mg foils with the carbon-fiber/PEEK prepreg through hot pressing. Proper surface treatments of AZ31 sheet using CrO_3 base etchants are necessary in order to achieve good interface bonding characteristics. The resulting Mg base laminated composite, with a low density of 1.7 g/cm^3, exhibits high modulus of 75 GPa and tensile strength of 932 MPa along the longitudinal direction. The experimentally measured tensile modulus and strength data along both the longitudinal and transverse direction are within 90-100% of the theoretical predictions by rule of mixtures, suggesting that the bonding between layers and the load transfer efficiency are satisfactory. The flexural stress and modulus along the longitudinal direction are 960 MPa and 54.6 GPa, respectively, suggesting a sufficiently high resistance against bending deflection. The peel strengths are about 2.75 and 4.85 N/mm along the longitudinal and transverse directions, respectively, superior to that of the epoxy-resin-adhered and carbon-fiber-reinforced aluminum laminated composites.

Polymer nanocomposites have attracted considerable attention during the past decade due to their versatile and extra-ordinary performances. The polymer nanocomposites can be prepared by the well-known sol-gel method. It is well known that PEEK is a good solvent resistant polymer. Hence, it is impossible to fabricate the PEEK nanocomposite by means of sol-gel method. In the second part of this study, the PEEK nanocomposites filled with nano-sized silica or alumina measuring 15-30 nm to 2.5-10 weight percent were fabricated by

vacuum hot press molding at 400^{o}C. The resulting nanocomposites with 5-7.5 wt% SiO_2 or Al_2O_3 nanoparticles exhibit the optimum improvement of hardness, elastic modulus, and tensile strength by 20-50%, with the sacrifice of tensile ductility. With no surface modification for the inorganic nanoparticles, the spatial distribution of the nanopartilces appears to be reasonably uniform. There seems no apparent chemical reaction or new phase formation between the nanoparticle and matrix interface. The crystallinity degree and thermal stability of the PEEK resin with the addition of nanopartilces were examined by X-ray diffraction, differential scanning calorimetry, and thermogravity analyzer, and it is found that a slight decrease in crystallinity fraction and a higher degradation temperature would result in as compared with the prestine PEEK.

中文提要

鎂合金由於俱低密度 (1.7-1.8 g/cm^3) 的特性，故可做為輕量化金屬結構材料方面之應用，因此在這幾年廣獲青睞。眾所周知，碳纖維 (CF) 強化聚二醚酮 (PEEK) 高分子複合材料 (CF/PEEK) 在其縱向俱有超高之比強度與比剛性；故Mg/CF/PEEK複合材料將是製備一高比強度及比剛性複合材料之另一方式。本研究第一部分將以三明治堆疊方式利用AZ31 鎂薄板與CF/PEEK預浸布在真空熱壓機中壓製低密度及高性能鎂基夾層複合材料。為獲致良好的界面接著性能，在熱壓前鎂板需利用CrO_3行表面處理。真空熱壓製得之Mg/CF/PEEK鎂基夾層複合材料俱低密度 (1.7 g/cm^3) 之特性，且在縱向之彈性模數及最大抗拉強度分別高達 75 GPa及 932 MPa。而不論是縱向及橫向之彈性模數及最大抗拉強度更高達 90 至 100%的理論值，顯示其界面接著及負荷傳遞是非常有效且充分。在Mg/CF/PEEK鎂基夾層複合材料之撓曲及剝離性質方面，在縱向撓曲模數及應力也分別高達 54.6 GPa及 960 MPa，顯示此鎂基夾層複合材料俱有很高的抗彎曲特性。再者，在縱向及橫向之剝離強度也分別達 2.75 及 4.85 N/mm，優於環氧乙烷接著之鋁基碳纖維強化夾層複合材料。

高分子奈米複合材料由於俱多樣化及超高性能之特性，在過去這十年來也吸引眾多注目的眼光；眾所周知，高分子奈米複合材料可利用溶膠-凝膠法製得。PEEK因俱耐溶劑特性，因此，無法利用溶膠-凝膠法製備PEEK奈米複合材料。本研究第二部分將利用熱壓成型法在 400^{o}C真空熱壓機中製備PEEK奈米複合材料，並利用 15 及 30 奈米大小的氧化矽及氧化鋁作為強化相，此強化相之重量分率在 2.5 至 10%之間。經實驗證實，氧化矽及氧化鋁含量在 5 至 7.5 之重量百分率時，PEEK奈米複合材料之硬度、彈性模數，及最大抗拉強度可提高百分之 20 至 50，但其斷裂伸度則下降。在無任何的奈米粉體表面改質下，氧化矽及氧化鋁奈米粉體在PEEK基材中之分散還算均勻；且經X-ray繞射證實，氧化矽及氧化鋁奈米粉體與PEEK高分子間並無明顯的化學反應產生。氧化矽及氧化鋁奈米粉體的添加對PEEK高分子結晶性及熱穩定性的影響則利用示差掃瞄卡計

(DSC) 及熱重分析儀 (TGA) 檢測之，實驗證實經氧化矽及氧化鋁奈米粉體強化之PEEK奈米複合材料的結晶度會稍微下降，而熱裂解溫度則會較諸純PEEK提高約 40^{o}C。

致謝

人的一生總是會經歷許許多多的抉擇，這些抉擇到最後就會印證當初決定的正確與否。當初，承蒙恩師 黃志青教授的恩慈與啟示，使我由高分子組，毅然地跨到金屬組，當時也不知這決定是否正確；不過，經歷了這三年半在恩師的教導、關心與鼓勵當中，讓我能夠一直充滿信心，並順利取得博士學位。有了當時恩師的開導與啟示，使我在這博士學涯中才得以克服種種困難，我要再次說聲：老師，謝謝您，您辛苦了。

我也要由衷地感謝本所陳明與高伯威教授，由於您們的指導、鼓勵與幫助，使我實驗的進行才得以更加順利；還有機電所的任明華教授，由於您的協助，使我的實驗進行順利。

最令我難忘的是黃幫所有成員，在這個大家族中，大家互相幫助，相互討論，彼此鼓勵，這種體驗是很難得的。凱琳學姐在 TEM 上的幫忙，建超的鼓勵，佩如學姐、鉉凱、英博、敬仁、小明在實驗上的協助與金屬材料知識的開示，子翔、志溢、宇庭、政信、家豪、海明、世儒在實驗上的協助，炎暉在口試時的幫忙，謝謝您們。另外，我也要感謝庾忠義學長與吳玉娟同學在 Instron 及 SEM 上的教導與協助，機電所曾育鍾同學在實驗上的熱心協助。

最後，我要將這一份喜悅獻給我年邁的母親，由於您時時的鼓勵與支持，使我才有足夠的毅力與信心，完成博士學位。我也要向我三位可愛又乖巧的子女，鈺菁、筱娟、哲昇說聲對不起，爸爸這幾年沒能全心全力地照顧你們。在天國的父親，願您也能感受到兒子的這一份小小的成就。

謝謝所有關心我的大家。

Chapter 1 Background and Research Motive

1.1 Light-weight magnesium based alloys

1.1.1 Characteristics of magnesium alloys

Magnesium alloys have attracted considerable attention and interest worldwide during the past five years, due to the improvement of casting and processing techniques. Magnesium is the 8th most abundant element; the earth crust and ocean consist of 1.93 and 0.13 mass percents of magnesium, respectively [1]. In 1808, almost two hundreds year ago, magnesium was first extracted into a pure form by Davy [2]. Through extensive basic studies over the years, the chemical and physical properties of magnesium are well established. It is noted that Mg is the lightest structural metals on earth; Li and Be are indeed even lighter but the former cannot be present in individual metal form and the latter is extremely toxic. Because of its low density of ~1.7 (similar to or only slightly above the densities of most polymers and polymer composites), as shown in Table 1-1 [3], this metal raises the possibility of weight saving in metallic structures, and particularly in aircraft, vehicles and transportation equipment. Moreover, magnesium alloys have been, or have potential to be, applied by their characteristic natures of high specific strength and stiffness, superior damping capacity, high thermal conductivity, high dimensional stability, and good machinability [4].

Magnesium can be alloyed with various solute elements, including aluminum, zinc, lithium, thorium, silver and several rare earth elements such as cerium, neodymium and yttrium [2,5,6]. The addition of aluminum can largely increase the alloy strength through solution and precipitation strengthening, while a small amount of Zn will improve the cast capability. The designation of magnesium alloys is based on the abbreviation of the including

solute elements and their contents in weight percent. For example, the AZ31 alloy is referred to the magnesium base alloy added with nominally 3 wt% of aluminum (A) and 1 wt% of zinc (Z).

Since magnesium has fairly low plastic formability and limited ductility because of its HCP (hexagonal close-packed) crystalline structure, the fabrication of magnesium products are usually proceeded by die-casting or thixomolding [7]. This is distinctly different from the case of aluminum alloys, for which the wrought-typed aluminum alloys are more frequently applied; and the wrought alloys generally exhibit higher fracture toughness than the cast alloys. For commercial wrought magnesium base alloys currently available, it is still difficult to manufacture structural components. Recently, the plastic forming of magnesium alloys can be greatly improved by means of (1) the reduction of impurities during extraction metallurgy and casting routine, and (2) the structure control through secondary thermomechanical processing treatments in order to refine mainly the grain size. As a result, numerous Mg alloys were processed to exhibit superplasticity at elevated temperatures of ~0.5-0.8 T_m, where T_m is the material melting point expressed in Kelvin. Thus, new processing means, such as superplastic forming, press forming, and injection molding, are gradually becoming more important techniques to fabricate a hard-to-form material into complex shapes [8-10].

In 1999, press forming of the AZ31 magnesium sheets was conducted under a more economical condition, i.e., proceeding at a speed and temperature faster and lower than the superplastic forming practice [11]. It is known that a small grain size can improve the superplasticity performance of alloy, the smaller the grain size will lead to better ductility and higher optimum strain rate for superplasticity. Therefore, hot extrusion and powder metallurgy methods have been utilized to produce superplastic microstructures [12,13]. The AZ91 and AZ31 alloys with grain sizes of ~5 μm, hot extruded at a reduction ratio of 100:1,

exhibited tensile elongations of 350% at 3×10^{-4} s^{-1} and 200°C and 620% at 10^{-4} s^{-1} and 325°C, respectively [12,13]. And the AZ91 and ZK61 alloys processed by powder metallurgy showed tensile elongation over 300% at high strain rates of 10^{-2} s^{-1} to 10^{-1} s^{-1} [13]. Equal channel angular extrusion (ECAE), recently, has been developed to produce ultra-fine grains of 0.7 μm in the AZ91 alloy [14], resulting in a maximum elongation of 660% obtained at 6×10^{-5} s^{-1} and a relatively low temperature of 200°C.

With the improvement of Mg alloy processing, the properties of Mg alloys have gradually reached the requirements for high functionalities of mass products such as automobiles and electronic devices. Undoubtedly, Mg alloys are the extra light metals in the 21st Century.

In the past decade, electronics industry has made giant growth, especially in computer and communication areas. Due to the considerations of weight-saving, damping, electric and magnetic shielding, better heat dissipation, environmental stability, and recycling ability, the use of Mg alloys over polymers or polymer composites is under steady growth. It is apparent that, as a structural material, magnesium has numerous advantages over aluminum and engineering plastics. Therefore, Mg alloys have become more and more attractive for the design of new lines of video or photo graphic equipment, portable personal computers and notebooks, cellular and satellite cell phones, personal LCD projectors, and portable communication equipment. Another new field of application for Mg alloys is the medical uses, such as an implant material for surgery [15]. Magnesium offers a low dosage that is an essential element and does not harm the tissue; moreover, magnesium promotes the healing of the bone. Furthermore, the elastic modulus of magnesium is closely to that of the corticalis and the ultimate tensile strength (UTS) is higher than those of polymers. In addition, polymer based biodegradable implants would provoke a rejection by the body but magnesium would

not.

Magnesium matrix composites reinforced mostly by ceramic particulates may become structural materials for vehicles and aerospace applications because of their high specific mechanical properties. It was shown that magnesium matrix composites revealed increased hardness [16-18] and elastic modulus [16-19], and even low temperature superplasticity [20]. They can be fabricated by casting or powder metallurgy techniques and by deposition of matrix from semi-solid or vapor phase.

Nano-particle reinforced magnesium composites have been shown to enhance the mechanical properties [21,22]. Hwang and Nishimura [23] synthesized the Mg-TiC nanocomposite by mechanical milling. It was shown that the as-milled Mg-TiC nanocomposite contained magnesium matrix grain size ranging from 25 to 60 nm with a dispersion of ultra-fine nano-sized ceramic TiC particles (3-7 nm). It was also shown that Mg-TiC nanocomposite exhibited remarkably high ductility [23].

1.1.2 The properties of AZ31 magnesium alloy

It is well-known that Mg alloys show poor plastic formability due to the HCP structure. Except for this structural limitation, however, it is often difficult to fabricate large Mg products with high strength and high ductility by the casting process because of coarse grain size. In view of plastic formability and post-deformation mechanical properties, it has been reported that hot deformation process such as extrusion and ECAE can account for grain refinement [24-26] owing to the dynamic recrystallization in Mg alloys [27-29]. Higashi et. al. [24] conducted their study on the effect of high-strain-rate forming process on the grain refinement of commercial AZ31 (Mg-3wt%Al-1wt%Zn-0.2 wt%Mn) alloy. There were

various processes being conducted including (a) extruding the cast alloy with a high ratio of 100:1, (b) severe plastic deformation through ECAE, (c) powder metallurgy (P/M) procession of machined chip [24].

For process (a), the grain size of AZ31 was refined from initially ~15 μm to an equiaxal grain structure with the average size of ~5 μm at an extrusion temperature of 350^{o}C. On the other hand, the grain size developed by process (b) at 160 to 220^{o}C was varied from 0.5 to 3 μm according to the extrusion temperature. In addition, process (c) developed grain size varying from 2 to 4 μm at a temperature ranging from 210 to 430^{o}C. In view of superplasticity, the grain size must be refined to 0.5~2 μm for a target strain-rate range of 10^{-2}~10^{0} s^{-1} for mass production. Accordingly, the sub-micron grained structures can be achieved by process (b) ECAE of the cast AZ31 alloy.

Mukai et al. [26] also conducted their study on the ductility enhancement in AZ31 Mg alloy by controlling its grain structure. Two different processed AZ31 alloys were inspected in this study, one was the as-ECAE processed alloy, initially of grain size ~1 μm, which was followed by annealing (AZ31-ECAE/annealed) process to coarsen the grains to a grain size ~15 μm, the other was the conventionally extruded AZ31 alloy having grain size ~15 μm in average. In terms of tensile mechanical properties, the yield stress of AZ31-ECAE/annealed exhibited a half value compared with that of the as-extruded alloy owing to the difference of texture in the two alloys. However, the ultimate tensile strength of AZ31-ECAE/annealed revealed almost the same value as the as-extruded alloy; exhibiting a remarkable strain hardening and a large uniform elongation as compared with the as-extruded alloy. It is well known that cast magnesium alloys exhibit higher specific strength than those of steels due to their lower densities [30,31]. On the other hand, the values of elongation-to-failure for the Mg alloys also exhibit remarkable low values compared with the structural steels. According

to the study conducted by Mukai et al. [26], AZ31-ECAE/annealed exhibited a similar value of specific strength compared with the cast-magnesium alloys and a large value of elongation-to-failure (up to 50 %), similar to steels. Accordingly, the AZ31-ECAE/annealed alloy has a high potential in structural uses.

As shown in Table 1.2 [32], for extruded alloy, AZ80 exhibits comparable tensile strength as Al alloy 6061, but with less ductility. However, Mg sheet metal, such as AZ31 alloy, provides slightly lower strength but a higher ductility than commonly used 5XXX series Al sheet alloys. Also shown in Table 1.2 are the physical properties of PC/ABS plastics. Mg alloys are slightly heavier than the plastics, but they are much stiffer due to elastic modulus of magnesium is almost 20 times over a plastic material such as PC/ABS.

1.2 Thermoplastic high temperature polymer PEEK

1.2.1 The properties of PEEK

The high performance polymer poly(ether-ether-ketone) (PEEK) was firstly prepared by Bonner in 1962 [33]. It is a derivative of poly(aryl-ether-ketones). The PEEK polymer was reported to be synthesized by a nucleophilic aromatic substitution reaction, using dephenyl sulfone as solvent, at temperatures approaching the melting point of the polymer [34].

PEEK is chemically recognized as a linear poly(aryletherketone) and is a melt processable aromatic polymer; the melting point T_m is between 330 and 385 ^oC, depending on the relative proportion of ether-ketone groups linking the phenylene rings [34]. It is highly crystalline. Dawson and Blundell [35] reported the values for the lattice constants of the annealed isotropic samples and other parameters of chain conformations, as shown in Table

1-3.

The bulk properties of PEEK, compared with those for 'Victrex' polyether sulphone, are shown in Table 1-4 [34]. The crystallinity of PEEK and its lower glass transition temperature T_g highlight the major differences between these high temperature performance thermoplastics. As shown in Table 1-4, PEEK has a lower heat distortion temperature, just above its T_g. However, it maintains useful long-term mechanical strength up to 200^{o}C, due to its high T_m. According to the DMA (Dynamic Mechanical Analyzer) measurement conducted on PEEK and polyethersulphone [34], the polytehersulphone loses all mechanical strength at 200^{o}C. However, PEEK remains some rigidity until significant melting of the crystallites occurs near 300^{o}C.

Also shown in Table 1-4 is the resistance to solvent stress cracking for PEEK as compared with the polyethersulphone. And it is also derived from the crystallinity of PEEK. PEEK has good resistance to many organic solvents. Nevertheless, PEEK can be dissolved in concentrated H_2SO_4 and CH_3SO_3H, as shown in Table 1-5 [36]. It is believed that the protonation of PEEK, when dissolved, gives rise to repulsive electronstatic forces which can overcome the strong attractive forces in this highly crystalline polymer. Accordingly, the dissolution of PEEK in various sulfonic acids, followed by recovery of the polymer, provides a route to a new type of ionomer [37].

Morphologically, neat PEEK resin, similar to other semicrystalline polymers, possesses a spherulite structure as cooled from its melt. The degree of crystallinity of the polymer highly depends on its thermal histories and on the processing conditions, such as the cooling rate and annealing treatments. And in turn the degree of crystallinity of the processed PEEK imparts a very significant effect on the material properties and mechanical behaviors of the

resulting composites. Gao and Kim [38] found that the interface bond strength decreased with increasing cooling rate; the tensile strength and elastic modulus of PEEK resin decreased, while the ductility increased, with increasing cooling rate through its dominate effect on crystallinity and spherullite size. Accordingly, a slower cooling rate will result in polymers more brittle in nature than those fabricated by faster cooling from its melt state.

Thermoplastic polymers have been considered as substitutes for thermosetting matrices for high-performance composite materials. They offer advantages such as higher processability, easier repair and bonding operations, and reprocessabilies. Aromatic Polymer Composites (APC) based on continuous carbon fibers embedded in PEEK matrix represent one of the most developed high-performance thermoplastic composites. As well-known, some of the principal limitations of thermosets are their relative brittleness and water sensitivity. However, PEEK and APC have been turned out to be a good impact behavior and very low water absorption compared with high-performance epoxy systems [39-42].

1.2.2 Applications of PEEK

PEEK is a semicrystalline polymer and capable of providing many of the unique properties in terms of temperature and solvent resistances. High-performance microfiltration membranes from PEEK were prepared [43] for the application in large internal diameter hollow fiber (tubule) form, resulting in the highest cross-flow efficiency. The resulted membranes are a polymer blends and their pore sizes vary from approximately 0.12 μm at 16% PS (polysulphone) to approximately 0.3 μm at 25% PS for a given PEEK content, in which PS provides sufficient melt strength to the extruding blend. It was also shown that PEEK membranes provide superior performance to a PS membrane upon exposure to a warm surfactant/oil stream. However, the porosity of PEEK/PS membranes is about 5%, due to

membrane shrinkage during the leach step.

Furthermore, extrusion of film-microfiltration membranes of PEEK was also conducted [44], and the maximum pore size of the resulting membranes was less than 0.05 μm. In view of porosity of the membranes, however, it was reported that the ultrafiltration film membranes from PEEK, a 14% PEEK and 18% PS blend, yields a porosity of 79%.

PEEK has been shown to be environmental resistance and passive biocompatibility, i.e., absence of toxicity and biological inertness [45,46]. The native PEEK film was found to be a very poor substrate for cell cultivation, extremely reluctant to allow cellular adhesion [47]. Increasing of the surface hydrophilicity by introduction of polar groups has been investigated to improve the bioadhesion [48,49]. Surface carboxylated PEEK films were prepared from PEEK-OH films which are common key-intermediate, and these films revealed surface functionalities such as grafting of bioactive molecules like proteins and peptides [50]. Surface amination of the PEEK film [51], on the other hand, also proceeded by the grafting of glutamine, and this film displayed α-amino acid motifs fixed on the polymer backbone via a short spacer-arm. The surface fluorination of PEEK film has been successfully prepared [52]. It was realized to be a blood compatible material. Sulphonated PEEK films [53] have been shown to be capable of ion-exchange, and, as a result, exhibited a high permeability for copper ions due to the presence of fixed negative charges and to their swelling capacity in an aqueous phase.

PEEK polymers reinforced with nanoparticles have been reported [54-56]. The PEEK fine powders, ~100 μm, were fully mixed with Si_3N_4 nanoparticles and subsequently formed by compression molding [54]. As a result, the incorporation of Si_3N_4 nanoparticles into PEEK caused a significant improvement in the tribological characteristics, resulting

considerably in decreased frictional coefficient and wear rate. Furthermore, it was proposed that a thin and uniform transferred film could be formed on this composite during the friction process. Due to the increase of adhesion strength of the transferred film through chemical reaction between Si_3N_4 nanoparticle and the steel substrate [54], consequently, sliding occurred between the composite and the transferred film, resulting in a lower wear rate. In addition, PEEK polymers reinforced with other nanoparticles such as ZnO_2 [55] and SiC [56] were also examined, and similar results were reported.

Through the treatment with a dilute chlorosulfonic acid solution, the inner walls of the PEEK capillaries reveal an increase in surface area, which is suitable for the application of electrosmotically driven open-tubular liquid chromatography (LC) [57].

Among the so many applications of PEEK, the continuous fibers reinforced composites have become the most high-performance and advanced materials over the past decades. Undoubtedly, owing to the potential advantages of high fracture toughness, high temperature resistance, repairability, biocompatibility, and ease of manufacture, fiber reinforced composites of PEEK can extend their influences to many areas including aerospace materials, structural materials, and biomedical materials. Carbon fiber reinforced PEEK composite (CF/PEEK) is a shinny star among the PEEK composites, and is being considered as the candidates to replace the conventional epoxy-based composites for aerospace applications. And we will further discuss in more details in Section 1.3.2.

1.3 Introduction to polymer matrix composites (PMC)

1.3.1 Polymer matrix composites

It is well known that, in the past several decades, polymer matrix composites (PMC) have become advanced materials, and can be applied as engineering structural materials for aircrafts or vehicles, as well as biomedical materials for medical uses [58]. Polymer matrix composites are conventionally classified into two groups: thermoset matrix composites (TSC) and thermoplastic matrix composites (TPC). As shown in Table 1-6, thermoset composites have slightly different properties from the thermoplastic counterparts; the former ones usually exhibit much lower strains to failure.

Composite technology is based on taking advantages of the stiffness and strength of high-performance fibers by dispersing them in a matrix, which acts as a binder and transfers the acting load to the fibers across the fiber-matrix interface. To understand how the properties of a composite originate, it is necessary to know the properties of constituents form a composite system. The mechanical properties of a composite are determined by a number of factors, including the moduli and strengths of the fiber and matrix; aspect ratio, length distribution, volume fraction, uniformity and orientation of the fibers, as well as the integrity of the fiber-matrix interface and the interfacial bond strength [59].

The first generation of composite materials based on the more brittle thermoset matrix offers fracture toughness as low as 100 J/m^2. The development of toughened thermosets and a wide range of high performance thermoplastics have increased this value up to 2000 J/m^2 [60]. Advanced thermoset epoxy composites are now the most often used in high performance applications due to their unique performance-to-cost ratio. They generally possess excellent properties and are suitable for a large number of processing techniques. However, thermoset epoxy composites have been found that the properties of toughness and dimensional stability will decrease as the glass transition temperature T_g of the resin used increases.

In addition, a change in temperature and moisture content could result in moisture-induced stress as well as dimensional change in composite body [61-64]. Furthermore, the recursive changes of internal stresses due to water absorption-desorption processes may induce fatigue damage, and in turn influence long-term durability and performance of composite [65].

Thermoplastic matrix composites present a number of advantages over thermoset composites, including increased fracture toughness, lower moisture absorption, potential for reduced life-cycle cost, good welding property, and recyclability [66,67].

1.3.2 High performance carbon-fiber/PEEK (CF/PEEK) composite

Due to the high fracture toughness, high temperature resistance, repairability and ease of manufacture, thermoplastic matrix composites have been studied extensively [68-73]. Among these, the carbon-fiber/PEEK(CF/PEEK) composite is one of candidates to replace conventional epoxy-based composites for aerospace applications. Because of the short processing time needed, the CF/PEEK composite provides flexibility in adapting various manufacturing technologies to improve the production efficiency. However, the recommended processing condition for the CF/PEEK composite requires a forming temperature of 400℃ and a pressure of 1.4 MPa for 15 min [38], which are much higher than those for the epoxy-based composites. The higher requirement of processing conditions might therefore limit the potential to make use of cost-effective manufacturing technologies for fabricating components from the CF/PPEK composite.

During the past decades, many researches have been conducted to study the processing conditions in order to search for the opportunities of broadening the processing window for

the CF/PPEK composites. An inevitable variation of the processing condition is the cooling rate. Gao and Kim [38] found that the cooling rate controlled the degree of crystallinity which in turn was correlated to the interface adhesion, the crystalline morphology, and the bulk mechanical properties of neat PEEK resin. As a result, the interface bond strength, as well as the tensile strength and elastic modulus, decreased with increasing cooling rate. However, the ductility increased with increasing cooling rate due to its effect on crystallinity and spherullite size. In addition, the interface failure was recognized as brittle debonding in slow-cooled composites. In contrast, the amorphous PEEK-rich interface introduced in fast cooled specimens failed in a ductile manner with extensive plastic yielding.

Morphologically, it was shown that the presence of carbon fibers within the matrix would induce nucleation and growth of crystallites perpendicular to the fiber surface, i.e., transcrystallization, which might impose considerable influence on the fiber/matrix interfacial interaction and the failure behavior in both the matrix and the interface region [70]. In view of the effect of residence time in the molten state of the PEEK reinforced with carbon fibers (APC-2 prepreg by ICI/Fiberite Company, USA) on the number of spherulites present in the bulk matrix, it was found that increasing the residence time would result in a decrease in the number of spherulties, and a well-defined transcrystalline region was subsequently developed on the carbon fiber surface [74]. Consequently, the unidirectional CF/PEEK composite containing a transcrystalline phase showed a higher transverse tensile strength than that of the matrix, owing to a strong interfacial bond between the carbon fiber and the PEEK matrix.

Gao and Kim [75] also conducted a study on the effect of cooling rate on interlaminar fracture toughness of unidirectional CF/PEEK matrix composites. It was shown that the PEEK resin displayed a remarkable 230% improvement in fracture toughness when the

cooling rate was changed from 1 to 80 ^{o}C/min. Furthermore, they also conducted the study on the effect of cooling rate on impact damage performance of CF/PEEK laminates, and compared with CF/epoxy laminates [76]. They concluded that the ability to resist damage initiation upon impact was higher in the order of fast-cooled CF/PEEK, slow-cooled CF/PEEK, and CF/epoxy laminates. Meanwhile, they showed that the threshold impact energy was higher and the compression-after-impact (CAI) strength reduction rate was lower for the fast-cooled laminates than the slow-cooled counterparts, strongly indicating the higher impact tolerance of the former system.

The CF/PEEK composites possess extraordinary strength-to-weight and stiffness-to-weight ratios along the longitudinal (or fiber reinforced) direction, as compared with steel, Al or Ti alloys in Table 1-6 [77]. For this very reason, the CF/PEEK composites can be applied on high-requirement rigid aerospace or aircraft turbomachinery components, such as centrifugal impellers.

In terms of the biomedical applications, the CF/epoxy composite materials can be applied on the external fixation for bone fracture repair because of their lightweight and sufficient strength and stiffness [78]. On the other hand, the CF/PEEK composite materials have been applied on the internal fixation for bone fracture repair by different ways using implants such as wires, pins, screws, plates, and intramedullary nails [78]. Among various materials studied, CF/PEEK composite materials are reported to be biocompatible [79] and have good resistance to hydrolysis and radiation degradation. Except for their high strength and fatigue resistance, the CF/PEEK composite materials have been shown to be biological inertness with no mutagenicity or carcinogenicity. Moreover, the tissue response to CF/PEEK has been described as minimal. In view of the effect of exposure to saline solution (0.9% NaCl) on the flexural and fracture toughness properties of short carbon fiber reinforced PS (polysulfone),

PBT (polybutylene terephalate) and PEEK composites, CF/PS and CF/PBT composites showed significant degradation of mechanical properties following exposure to saline solution [80]. But there was no such reduction for the CF/PEEK composites, due to good bonding between the carbon fibers and PEEK matrix [81]. Animal studies showed that the CF/PEEK composite elicits minimal response from muscular tissue. Both the in vivo and in vitro aging studies confirmed the mechanical stability of CF/PEEK up to 6 months.

1.4 Particulate filled polymer composites

1.4.1 Characteristics of particulate filled composites

It is well known that the environment can significantly influence the mechanical performance of polymer matrix composites, especially for epoxy-based composites. As a result, the combined influence of moisture and thermal history can cause microcracking to develop along with plasticization; reducing the T_g of resin and increasing the dimension and tolerance of the materials [82]. Srivastava and Hogg [83] conducted their studies on the particle filled polymer composites to investigate moisture absorption behavior in 10 μm $Al(OH)_3$ particle and 40 nm PE particle filled GFRP (glass-fiber reinforced epoxy-vinylester resin). It was found that increasing the filler content in GFRP composites resulted in an increase in the equilibrium water uptake and in turn an increase in the effective water diffusivity coefficient. Moreover, the filled $Al(OH)_3$ GFRP composites revealed a higher content of moisture uptake and diffusivity coefficient than those of the PE-filled and unfilled GFRP composites. In terms of toughness of all composites, it was shown that the mode-I delamination toughness increased with increasing moisture content but changed little under mode-II testing. Furthermore, the $Al(OH)_3$ filled GFRP composites exhibited higher values of mode-I and mode-II fracture toughness than those of the PE-filled and unfilled GFRP

composites.

In view of damage performance of particle filled GFRP, with no concern about water uptake, it was shown that the interlaminar toughness (G_{IC} and G_{IIC}), absorbed energy, and residual compressive strength values of the GFRP composites increased with increasing particle content [84], due to stress-concentration induced plastic deformation and crack bridging. Based on this postulate, the PE-filled composites revealed higher values of mode-I, mode-II and impact toughness than those of the $Al(OH)_3$ filled composites.

It is believed that polymers with linear molecules of smooth profile will reveal low shear strength, with "running" films on their own surfaces and transfer films on the counterfaces along the sliding direction in rubbing contacts. This, as a result, offers low sliding friction, but suffers high wearing rates. Inclusion of hard fillers, including metals, ceramics, glass, and special polymers such as polytetrafluoroethylene (PTFE, Teflon) and high density polyethylene can reduce the wear rate by up to three orders of magnitude [85,86]. But the negative effect of such hard fillers is an increase in friction and, more importantly, abrasion of the mating counterface. On the other hand, polymers having bulk side groups, brancher or crosslinks reveal better wear resistance than polymers with linear molecules. Inclusion of hard fillers, on the contrary, can provide friction reduction. Burroughs and Kim [87] found that inclusion of boric oxide particles (150 μm) in PTFE and epoxy composite materials can provide PTFE with a two-order reduction in wear rate against stainless steel surface, and under similar environments, can reduce the friction coefficient of epoxy from $\mu>0.7$ to as low as $\mu=0.07$. Through the application of acid-base interactions on absorption and dispersion of particles in polymer matrix, walllastonite (mineral filler) was successfully incorporated into PMMA (polymethyl methacrylate) polymer matrix [88]. It was shown that the tensile modulus of the composite containing wollastonite and surface-coated wollastonite increased

by 66% and 78%, respectively, as compared with the unfilled PMMA matrix.

The porosity of fillers also imparted an effect on the abrasion resistance of nanoporous silica gel/polymer composites [89]. An organic monomer solution consisted of triethylene glycoldimethacrylate and various initiators was introduced into the silica gel powders which were of different porous structures and their media diameters were 13 μm to form a paste, and subsequently were polymerized inside a glass mold. As a result, it was found that the wear rate of the composites decreased with increasing filler porosity. Through scanning electron microscope (SEM) examinations, it was also suggested that the better wear resistance was associated with fine-scale plastic deformation of the wear surface and the absence of filler particle pullout.

Since the rapid growth of the electronic industry, demand for better packaging materials has become more and more important, especially for those having specific physical properties in combination with electrical insulation. For instance, to improve the life time of organic- light-emitting-diode (OLED) devices, the packaging materials must meet a number of functions, such as heat dissipation, moisture resistance, and electrical insulation. The polymer matrix composites can achieve these conflicting properties. However, the inclusion of ceramic powders into polymer composites was shown to enhance the intrinsically low thermal conductance of the polymers [90-92]. These composites show very different moisture resistance from that of the unfilled polymers [93], due to the presence of polymer filler interfaces. As a consequence, the electrical insulation of the filled polymers will be altered by the presence of the filler phases. To study these issues, Al_2O_3 (20 or 100 μm)/PU, carbon fibers (Φ8×30 or Φ8×100 μm)/PU, and boron nitride (5-11 μm)/silicone polymer composites were prepared [94], and the effects of moisture uptake on thermal conductance and dielectric relaxation were studied. It was found that water molecules were absorbed not

only by the polymer matrix, but also by the interfaces introduced by the fillers, and, in turn, the absorbed water molecules induced the phenomenon of dielectric relaxation for all materials. Among these three composite materials, the boron nitride/silicone composite absorbed the least amount of moistures, and accounted for the highest thermal conductivity value as compared with the other two. It was concluded that the boron nitride/silicone could be the candidate for the packaging materials used in electronic devices that require heat dissipation and moisture resistance, in addition to electrical insulation.

Electric field induced particle alignment has been reported for many electrorheological fluid systems [95-99]. The characterizations of field-induced aligned structures have been limited to optical observations with thin layers being confined between glass plates. On the other hand, field-induced particulate alignments in polymer composites were proposed [100]. Prior to polymerization, particles of different shapes, sizes, and dielectric constants could be aligned in a photopolymerized fluid by an electric field. Urethanedimethacrylate (UDMA) mixed with 1.6-hexanediol dimethacrylate (HDDMA) in a 90/10 ratio, which gave a viscosity allowing particles to align. The inclusion was silica-zirconia in two forms: P50, having a particle size of 0.7 μm in average, and Z100, also having a particle size of 0.7 μm. Applying the photosensitive initiator and accelerator, the particle-aligned UDMA/HDDMA (90/10) resin underwent *in situ* polymerization under a blue light gun. It was found that the rate of alignment depends on both of the dielectric constants of resin and particle, and on the particle size.

It is known that the electrical conductivity of polymers can be significantly improved by the introduction of metals or carbon black. Except for the change of electrical conductivity of polymers, the promising materials made from piezo ceramic/polymer composites can serve as ultransonic transducers for naval sonar devices, medical diagnostic systems, and

non-destructive materials testing [100]. A ceramic tape casting slurry based on lead-zirconium-titanate was cast on a silicon coated PET carrier film [101].

Composite materials containing conducting fillers or ferroelectric particles [102,103] have been studied. The three-component (epoxy resin, barium titanate, and carbon black) composite materials can be effective absorbers for electromagnetic waves due to their high imaginary part of the complex dielectric permittivity which is responsible for the dissipation of electronmagnetic energy and due to their low bulk conductivity. Moreover, these materials can be also applied on sound absorbers and damping materials: the elastic waves interact with ferroelectric particles and electric energy is transformed into electrical energy that is then dissipated in carbon black particle chains.

1.4.2 Characteristics of nanoparticulate-reinforced polymer composites

It was shown that rigid inorganic particles could improve the physical properties of polymers for specific applications. With the inclusion of such particles, increase in stiffness and thermal stability was achieved; but unfortunately reduction in the ultimate fracture strain was inevitable [104,105]. Furthermore, it was also concluded that, for a given filler content, the yield stress of the composites decrease with decreasing filler size [106-110]. This is because that the smaller the size of the fillers, the larger specific surface areas would result in, indicating an increase in probability of aggregation. And the particle aggregation in the matrix would usually lead to the formation of high-order structures (agglomerates). It was believed that the agglomerates could be easily broken apart during external loading [111].

Kim and Lee [112] conducted their studies on the micromechanical deformation processes of ultrafine SiO_2 particle-filled polyethylene composites. The composites were

polymerized in the presence of SiO_2 (250 nm in diameter) inorganic filler particles. It was concluded that agglomerate formations of high-order structures were apparent with agglomerate size of the order of 10-50 μm. The deformation mechanisms are strongly affected by these high-order structures. The agglomerates, holding together by weak adhesive interaction, could impart multiple debonding processes inside the agglomerates and in turn toughen the polymer composites.

Carbon nanotubes (CNT), which was discovered in the early 1990s [113], have been known as the materials that possess not only excellent mechanical properties but also superior thermal and electric properties: thermally stable up to 2800^{o}C in vacuum, thermal conductivity about twice higher than that of diamond, electric-current-carrying capacity 1000 times higher than copper wires [114]. Because of their exceptional properties, carbon nanotubes have motivated many researchers in the field of nanotubes-reinforced polymer composites. Although it is not well developed yet, however, many of these studies have been reported.

Ajayan et al. [115] prepared CNT/epoxy composite materials with aligned carbon nanotube arrays. It was believed that the aligned structures usually have high aspect ratios (1000 or more) and this phase when shrunk to molecular dimensions could create new properties.

Nanometer particles are thought not only to improve the mechanical properties of the polymer matrix, but also to improve the matrix electrical conductivity. It is generally recognized that polymers are, in nature, of good insulation properties. However, polymers may become relatively good conductive materials by the incorporation of metal fillers [116] or carbon black (CB) fillers [117-120]. Balabanov and Krezhov [121] prepared the carbon

black (hemispherical particles of 80 nm in mean diameter) reinforced ultra-high-molecular-weight-ployethylene (UHMWPE, molecular weight = 4×10^6) polymer composites. It was found that, by introducing the fine dispersive carbon black of an amount of 5 vol% in UHMWPE, the specific surface direct-current (dc) conductivity K_s of the composite materials after high-dose irradiation could be drastically changed. And they suggested that the carbon black at moderate concentrations could substantially increase the K_s of these polymer composites.

On the other hand, PET reinforced with carbon black was reported by Connor et al. [122]. They investigated the temperature dependence of the conductivity of carbon black filled PET composites and suggested that, for temperatures greater than 45 K, conduction could be ascribed to thermal fluctuation induced tunneling of the charge carriers through the insulating layer of polymer separating two CB aggregates.

Water-based ferrofluid (Mn-Zn-Gd) having particle size ~6.5 nm was used to prepare a ferrofluid-PVA composite coating on high T_c (=－155.8 ^oC or 117.2 K) superconductor $Bi_2Sr_2Ca_2Cu_3Oy$, denoted as Bi(2223) [123]. Ultrafine particles of high-T_c material was mixed into pre-prepared ferrofluid-polymer solution. The as-mixed films were grown by spinning technique and dried under the condition with and without magnetic field. Through X-ray diffraction (XRD) studies, it was shown that there was an increase in the crystallite size for the film grown under the magnetic field, due to crystallographyically oriented individual domains forming a uniform size of agglomerates. The size of agglomerates was in the range of 30-40 nm. Moreover, films prepared under the influence of magnetic field showed higher magnetization as compared with the films prepared without the influence of magnetic field.

On the other hand, nanometer-metal-particule/polymer composite materials have been prepared. Wizel et al. [124] prepared the cobalt-polymer and iron-polymer composites by means of ultrasound radiation. The amorphous cobalt and iron particles measuring 10-30 nm and 50-90 nm in size, respectively, were mixed with distilled methylacrylate or methylmethacrylate (MA or MMA) monomers in dry N, N'-dimethylformamide (DMF) using sonication cell without exposure to air [125]. The sonication product was a colloidal solution, and the polymer was precipitated from the colloidal solution by adding, under N_2 atmosphere, an excess of cold methanol at the end of the sonication. In view of the magnetic properties of these nanoparticles reinforced polymer composites, it was found that the Fe-PMMA (Fe-Poly(methyl methacrylate)) composite shows superparamagnetic behavior due to single-domain particles. Moreover, the Fe-PMMA did not show saturation of the magnetization and also lacked hysteresis in its magnetization loops. The Co-PMA also showed the same behavior. But the magnetization values measured for the cobalt particles were always lower than those of the iron.

1.4.3 Silica nanoparticle reinforced polymer composites

Silica (SiO_2) has been becoming important as reinforcing filler for rubbers, compared with carbon black. In tire treads, silica can yield a lower rolling resistance at equal wear resistance and wet grip than carbon black [126]. Non-porous silica with a surface area of 130 m^2/g and a primary particle diameter of 16 nm was incorporated into the thermoplastic polymers (EVA, PP, PS) by mechanical mixing under the molten state of polymers [127]. It was found that the silica particles could cluster themselves into a network structure in the molten polymer state. Due to the small size and high specific surface area, nanosized-silica particles are favorable to form self-aggregation and a three-dimensional network structure in the molten polymer matrix [127]. As a consequence, the Payne effect [127], i.e. the decrease

of modulus with increasing deformation ratio, can be generally explained in terms of the breakdown process occurring in the agglomerates. Moreover, it has also been proposed that the silica network structure in molten state has the memory of the silica structure in solid state. As a consequence, a complete volumetric expansion of the resulting composite does not allow to undergo unless a large strain amplitude being applied during dynamic mechanical testing.

Lee et al [128]. incorporated the hydrophobic silica filler of 12 nm in diameter into the blends of liquid crystalline polymers (LCPs) and polypropylene (PP) by mean of twin-screw extruder. It is found that the nanofiller could act as a fibrillation enhancer for in-situ LCP/PP composites. As a consequence, the inclusion of nano-sized silica by mean of twin-screw extruder could induce high aspect ratio LCP fibrils through shear flow. Moreover, the resulting composites exhibited better tensile strength and modulus accompanied with only a small reduction in failure strain.

Musto et al [129]. reported that the morphology of the silica/polyimide hybrid could be controlled by using a coupling agent such as γ-glycidyloxypropyltrimethoxysilane (GOTMS). Conventionally, micro-sized particulate composites could be produced in the absence of GOTMS. However, nano-structured and co-continuous nanocomposites would be obtained by introducing the coupling agent in the precursor solution for the silica phase. It is found that the presence of the inorganic phase reduces the extent of plastic flow of the polyimide phase and, as a result, fracture takes place at progressively lower strain with increasing silica content. In addition, the silica/polyimide composites with the use of compatibilizing agent (GOTMS) can increase their tensile stress at the silica contents up to 15 – 20% by weight. As expected, a co-continuous phase morphology with high adhesion between the phases could bring about significant improvements of the tensile properties. Through SEM observations,

morphologically, the introducing GOTMS can form fine interconnected or co-continuous phases morphology. It is known that in polymeric composites the external stress is transferred from the continuous polymeric matrix to the discontinuous reinforcing phase. As a result, the ultimate properties of the composite materials are dependent on the extent of bonding between the two phases.

Organic/inorganic hybrid polymer composites can also be prepared by polymerization compounding [130]. Ultra fine fumed silica particles, with the specific surface area (BET), particle size and density of ~390 m^2/g, 7 nm, and 2.3 g/cm^3, respectively, were firstly attached with tert-butyl hydroperoxide to impart the surface activation of the modified silica particles. Then, the monomers and the initiator were grafted onto the activated silica sites. By means of radical polymerization, the polymer chain segments could in situ grow up at the activated sites of the porous silica. Accordingly, this polymerization compounding method could obtain polymers with narrow molecular weight distribution as well as block copolymers. Moreover, because of the growth of polymer chain segments onto the porous and activated silica particles, little agglomeration could be occurred. Consequently, through polymerization compounding technique, polymers or copolymers can be successfully grafted on the silica surface. With a more controlled morphology, such as tethered chains, polymer 'brushes' or patterned film could be obtained.

On the other hand, modified nano-sized silica particles could react with a silane-coupling agent, such as 3-(trimethoxysilyl) propyl methacrylate, and therefore graft this coupling agent on the silica particles [131]. It was proved that the amount of the grafted coupling agent on the silica particles was about 2 molecules per nm^2. Mixing these grafted silica particles with poly((meth)acrylate) and then coating this mixture on the substrate of polycarbonate would increase the hardness of poly((meth)acrylate) film. TEM (transmission

electron microscope) images taken from the silica-(meth)acrylate hybrid coating show the coating film having a separated and clear-cut domain of silica particle. In addition, Tan et al. [132] also used the above silane-coupling agent to react with polyethercarbonate via a free radical reaction to obtain thealkoxysilane-containing copolymer precursors, which could be used in subsequent sol-gel process to result in the polyethercarbonate-silica nanocomposites.

In addition to layer clay, nanoscale colloidal silica has been considered as inorganic fillers for the preparation of polymer nanocomposites by means of the sol-gel process [133-136] or in situ polymerization technique [130]. Even since the sol-gel technique was applied to result in polymer nanocomposites, silane coupling agents were commonly employed to improve the inorganic-organic interfacial compatibility [129]. However, during the curing stage such as epoxy compound, the evaporation of solvent and the gelation reaction of the hydrolyzed alkoxysilane occurred simultaneously. As a consequence, the solution process of sol-gel technique is not practical in the processing of epoxy molding compounds. The simultaneously released volatiles from the gelation of alkoxysilane sol would certainly bring about undesirable effects to the epoxy resin, as well as difficulties during epoxy curing reaction. Another drawback in using the sol-gel process in polymer-silica nanocomposites is its harm to the initial thermal stability of the resulting nanocomposites. This effect is mainly due to the residual of the silanoxy group in the resulting polymer-silica nanocomposites, and these silanoxy groups might perform dehydration reaction at high temperatures in the processing or service period of the nanocomposites.

1.4.4 Effect of the incorporation of nanofillers on the crystallization of polymer chains

It is well understood that the physical, chemical and mechanical properties of the

crystalline or semi-crystalline polymers will greatly depend upon the morphology, the crystalline structure, and the degree of crystallization of polymers. In order to control the rate of crystallization and the crystallinity of polymer and in turn to bring the desired morphology and properties into play, a great deal of effort has been devoted into the study of crystallization behaviors of polymers and the change in material properties. Wengui et al. [137] have made their effort on the crystallization and melting behaviors of nylon 6/foliated graphite (FG) nanocomposites. The foliated graphite particles having an average thickness of about 50 nm and an average diameter of about 12 μm were incorporated into the molten state of ε-Caprolactam monomer. After homogeneous mixing and ultrasonic irradiation, polymerization was carried out. The resulting nylon 6/FG nanocomposite contains 1.50 wt% FG, as expected. The isothermal and non-isothermal crystallization analyses were conducted [137]. It is found that the process of crystal nucleation and growth for pristine nylon 6 is a 3D process, but it is a 1D process for that of the nanocomposite under isothermal conditions. At each crystallization temperature, the crystallization half-time for the nanocomposites is lower than that of the nylon 6. However, the opposite results were found for the total crystallization time and the crystallization rate parameters. In other words, there might have more nuclei invoked for the nanocomposite, as compared with those for neat nylon 6, and the spherulite impingement would occur at later stage. The activation energy value of isothermal crystallization for the nanocomposite is higher that that of the neat nylon 6. In view of cooling scans, the peak crystallization temperature (T_{cp}) for the nanocomposite is found to be higher than that of neat nylon 6 by ~4^{o}C under different cooling rates, while the enthalpy of crystallization for the nanocomposite shows a lower value compared to the neat nylon 6. On account of the melting behaviors, the peak melting temperature (T_{mp}) for neat nylon 6 shows a higher value. Consequently, evidences show that the addition of the foliated graphite nanosheets might hinder the motion of the nylon 6 molecular chains, leading to less perfection of the crystals.

Nevertheless, Fornes and Paul [138] proposed that a very low level of clay could result in dramatic increases in crystallization kinetics relative to the extruded pure polyamide. However, increasing the content of clay beyond these levels (~ 3-5 wt% as reported) retards the rate of crystallization. As compared to the report just mentioned above, the incorporation of clays could slightly lower both the melting and the crystallization temperatures, but the heat of fusion, heat of crystallization, and crystallinity were found no obvious change in magnitudes. It is also suggested that nanocomposites containing commercially relevant concentrations of clay, i.e. ~3-5 wt%, have comparable crystallization times and temperatures as the pure polyamide with a similar processing history.

However, poly(ethylene 2,6-naphthalate), PEN, filled with nano-sized silica (hydrophilic fumed silica ~ 7 nm) was found to be of significantly enhancing the crystallinity of the resulting silica-filled PEN nanocomposites [139]. The PEN nanocomposite can increase its crystallinity from 22.3% for the pristine PEN to 36.8% for PEN with 0.9 wt% silica-incorporated. On account of non-isothermal crystallization scans, it is found that the crystallization temperature decreases as the cooling rate increases, and the crystallization time required is significantly reduced as the silica introduced, indicating heterogeneous nucleation occurrence while the nano-scaled silica existed in the PEN. Moreover, the crystallization exothermic peak shifts to a higher temperature as the silica content increases.

1.5 Laminated composites

Among the developments of metal matrix composites, graphite-fiber/aluminum composite was one of the early developed material. Owing to the poor wetting between aluminum and graphite fibers, there have been numerous attempts to produce graphite-fiber/aluminum composites including liquid infiltration [140], electroplating [141],

chemical vapor deposition [140], powder infiltration, and hot-forming [142], but none of these resulting composites could fully utilize the fiber properties in accordance with the rule of mixtures (ROM). Since the contact angle between the graphite fiber and liquid aluminum is greater than 90^{o} at temperatures near the melting point of aluminum, as a consequence, wetting is not spontaneous. However, liquid-metal infiltration has been successfully conducted on the coated graphite fibers in order to promote wetting with the molten aluminum. Liquid sodium coating process which is conducted in a helium atmosphere at temperature above 450^{o}C [143] can serve as a pretreatment for making a variety of graphite-fiber metal-matrix composites. Using this technique, the strength of graphite-fiber/ aluminum composite materials was typically ~ 680 MPa for 28 vol% Thornel 50 (i.e., rayon for its precursor) fibers, corresponding to about 100% ROM [144]. Furthermore, the stability of the coating was shown to be satisfactory with no significant decrease in tensile strength at test temperatures as high as 500^{o}C. Titanium-boron coating process can impart a sufficient low wetting angle with molten aluminum to permit spontaneous infiltration, and it has been applied to a variety of graphite fibers, including rayon-, PAN- and Pitch-based precursors. Because of the sodium contamination that can occur during processing, the titanium-boron process has become more extensively used.

Continuous carbon fiber (copper coated) reinforced copper-matrix composites prepared by diffusion bonding technology were proposed [145]. It was concluded that diffusion bonding is a very promising technology for producing continuous carbon-fiber reinforced copper-matrix composites with high thermal conductivity. And consequently, the carbon-fiber/copper composites could serve to dissipate heat generated during the operation of many currently used electronic systems containing a high concentration of microchips and powerful parts.

Carbon fiber reinforced aluminum laminates (CARALL) have been developed [146] to offer the superior fatigue crack growth resistance. Lin and Kao [146] conducted CARALL by sandwiching carbon-fiber/epoxy prepreg between aluminum sheets. It was shown that not only the CARALL can offer high modulus, high tensile strength and lower density than those of the 2024-T3 aluminum alloy in the longitudinal direction, but these laminated composites, as expected, show superior fatigue crack propagation resistance about two orders of magnitude better than that of the 2024-T3 aluminum alloy.

Carbon fibers reinforced magnesium composites have been recognized as new promising structural materials, due to their high specific strength and stiffness, high electrical and thermal conductivities. The main problem of fabricating these materials is that the molten magnesium does not wet or bond to carbon fibers. As a result, it is impossible to achieve load transfer from the matrix to the fibers in accordance with ROM. There have been many developments proposed to solve this problem including titanium-boron coating by CVD on carbon fibers [147] or coating of silicon dioxide on carbon fibers [148,149]. Katzman [149] successfully fabricated graphite-magnesium composites. Composites with wire shape showed 80 to 95% of the ROM values at room temperature. On the other hand, SiC coating on graphite fibers to improve the welting behavior between graphite fibers and molten magnesium has been conducted. Wu et al. [150] conducted their studies in analyzing the interface of graphite-fiber/Mg composites. It was found that the interface in these composites showed a multi-layer microstructure and an amorphous SiC coating which was found in the area between the coating and matrix, and some MgO platelets were also present in the matrix. The presence of MgO in the matrix was believed to impart a good bonding between the coating, MgO and the matrix.

Unlike the metal-made internal engines, polymer/metal composites could provide an

internal supply of polymeric lubricant during the extended service of an engine [151]. It is believed that such composites provide internal sources of polymeric materials which flow to the surface so as to provide boundary/surface lubrication. Except for the lubrication effect, these composites also offer the advantage of self-healing function to heal the damaged area on the surface. These promising composite materials consist of a matrix material of INCONEL 625 and 3-7 vol% of PEEK [152]. However, It was shown that such composites might be susceptible to fatigue damage under severe thermomechanical environments.

1.6 Motive of research

As mentioned above, Mg alloys possess high specific strength and stiffness, superior damping capacity, high thermal conductivity, high dimensional stability, good electromagnetic shielding characteristics, and biocompatibility. Due to the improvements of various forming process, Mg alloys can reach the requirements for high functionalities of mass products.

Carbon fiber reinforced Mg metal matrix composites have been proposed [147-149]. According to ROM, incorporation of 20 vol% of carbon fiber (high modulus carbon fiber) reinforcement can improve the stiffness and tensile strength of Mg alloys to about 170% and 150% [147], respectively. So far, Mg/CF composites were mainly fabricated by means of liquid metal infiltration, chemical vapor deposition, powder infiltration, and hot-forming, but none of the resulting composites could fully utilize the fiber properties.

It is well known that fiber-reinforced aluminum laminates (FRALL) have been successfully fabricated and commercialized. The aramid fiber-reinforced aluminum laminates (ARALL) were marketed by the Aluminum Company of America for the applications such as

aircraft lower wing skin, fuselage and tail skins. Moreover, carbon fiber-reinforced aluminum laminates (CARALL) show a superior crack propagation resistance under tension-tension fatigue. All the above developed FRALLs contain epoxy-resin polymer, consisting of alternating layers of thin aluminum sheets bonded by layers of high-strength fiber/epoxy prepreg. The service temperature is not expected to exceed 100^{o}C.

Carbon fiber reinforced PEEK polymer matrix composites, as mentioned early, have become advanced structural materials, extending their influence to aerospace ultilities and biomedical applications. The fabrication of CF/PEEK composite, as reported, needs a temperature ~ 400^{o}C and a pressure ~1.4 MPa for about 15 min. These fabrication conditions are somewhat severer than those for epoxy-based composites. However, it was shown that CF/PEEK composite can offer better toughness and ductility than those of CF/epoxy composites.

Based on the previous studies on Mg and PEEK matrix composites, it would be interesting to explore the feasibility of the laminated Mg/CF/PEEK composite by means of laminating the CF/PEEK prepreg (APC-2 by ICI/Fiberite Company) with the sheets of Mg alloy, as the developments of FRALL, ARALL, and CARALL, i.e., merely through laminating Mg sheets and the APC-2 prepreg in vaccum hot-press. This part of study is aimed mainly at the further strengthening for Mg alloys. Commerical wrought Mg alloys usually exhibit UTS levels around 300 MPa at room temperature, and CF/PEEK prepreg itself (with 61 vol% CF) will reach strength levels to 2130 MPa. Thus, the coupling of Mg with ~39 vol% CF/PEEK into the Mg/CF/PEEK laminated composites, might double the strength level. For this part of study, the Mg remains to be base matrix, and the CF/PEEK acts as the strengthener. The major applications are still for light-weight structural purpose. The density will be around 1.7 g/cm^{3}, and the specific strength may reach above 500 MPa・

cm^3/g, two times over the commercial steel, Al, Mg, or Ti structural alloys.

Meanwhile, nanoparticle reinforced composite materials have also attracted attentions because of their unique characteristics. Nanoparticle reinforced polymer composites have been fabricated for various specific applications including promoting the mechanical properties and electric conductivity. It is also worth conducting our study on the nanoparticle/PEEK composites for the purpose of mechanical enhancement. For this part of study, the low-priced nanoparticles, such as SiO_2 or Al_2O_3 measuring ~15-30 nm in diameter, will be added in small amount (~0-10 wt%) into the polymer matrix first. Strengthening by these particles is expected, provided that uniform dispersion is achieved by proper processing. The inclusion of much cheaper (in comparison with CNF or CNT) nano SiO_2 or Al_2O_3 particles (with diameters ~15-30 nm) into PEEK is of basic interest for the purposes of processability and mechanical enhancement. The present study is focused on the simple compression molding to fabricate the PEEK nanocomposites containing 0-10 wt% nanometer sized silica or alumina particles without any surface modification for the sake of economic concern. The mechanical property improvement and the interaction between the filled particles and the PEEK matrix are under examination. Moreover, the effects of the nanoparticle inclusion on the non-isothermal crystallization of PEEK chain segments and on the enhancement of thermal stability of PEEK composite are also under investigation.

The framework of this study is illustrated in Fig. 1.1, and the following works are aimed.

A. For the Mg/CF/PEEK laminated composites

(1) To fabricate the Mg/CF/PEEK laminated composites by means of hot pressing.

(2) To study the effect of processing parameters on the mechanical properties, interface bonding of the laminated composites.

(3) To investigate the major mechanical properties at room and elevated temperatures for the

laminated composites, including the tensile, bending, and peeling aspects.

(4) To analyze the data in overall views, including the strengthening effects, deformation mechanism, interface bond-strength, and failure analysis.

B. For the silica or alumina particles filled PEEK composites

(1) To prepare the silica or alumina nanoparticles filled PEEK composites by means of compression molding.

(2) To estimate the reinforcing effect of the fillers on PEEK mechanical properties.

(3) To study the dispersion of the fillers in the PEEK matrix.

(4) To determine the interface interaction between the nanoparticle and the PEEK polymer.

(5) To investigate the effect of the inclusion of filler on the crystallization behaviors of the PEEK segments.

(6) To estimate the effect of the incorporated fillers on the thermal stability of the PEEK polymer.

Chapter 2 Experimental Methods

2.1 Materials

The as-received AZ31 (Mg-3wt%Al-1wt%Zn-0.2wt%Mn) Mg sheets, 2 mm in sheet thickness and 34 μm in average grain size (Fig. 2.1), were supplied by CDN Genova Ventures LTD., Canada.

The prepreg used in this study is the AS-4 continuous carbon fiber reinforced PEEK prepreg, designated as APC-2 and fabricated by the ICI/Fiberite Company, USA. It contains ~61 vol% or ~68 wt% of continuous AS-4 carbon fiber (diameter ~ 7 μm and density ~ 1.77 g/cm^3), and the density of the prepreg is about 1.6 g/cm^3. The matrix of APC-2 is a tough, ductile, and semicrystalline thermoplastic PEEK polymer with T_g and T_m of 143 and 343^{o}C, respectively. The thickness of the prepreg is 120-150 μm.

The PEEK powders (grade Victrex 450P, diameter ~2-3 mm) were purchased from the ICI Company, USA, and were further grinded into fine powders measuring 100 μm. The density of PEEK polymer is 1.30 g/cm^3. The SiO_2 and Al_2O_3 nanoparticles with diameter ~30 or 15 nm and purity ~99.9% were purchased from the Plasmachem Gmbh Company, Germany/Russian. The amorphous SiO_2 particles are nearly spherical in shape with an aspect ratio near 1, and the crystalline Al_2O_3 powders are basically irregular, as shown in Fig. 2.2. The density is 2.65 g/cm^3 for SiO_2 and 3.98 g/cm^3 for Al_2O_3, as shown in Table 2.1.

2.2 Mg/CF/PEEK laminated composites

2.2.1 Preparation of Mg/CF/PEEK laminated composites

The as-received 2 mm AZ31 Mg sheets were further rolled to about 0.5 mm thick at 300^{o}C. Prior to laminating with the APC-2 prepreg, the slimmed AZ31 sheets were subjected to abrasion with #100 SiC abrasive papers, and then to CrO_3/Na_2SO_4 chemical etching in order to create the rough surfaces for better bonding with the APC-2 prepreg.

Various layers of the APC-2 prepreg were sandwitched with the AZ31 sheets to produce Mg/CF/PEEK laminated composites. The stacking sequence was AZ31/APC-2/AZ31/ APC-2/AZ31 in unidirectional array, as shown in Fig. 2.3. Processing of the Mg/APC-2 composite was conducted by means of vaccum hot pressing at 400^{o}C under a pressure of 1.4 MPa for 15 min [38]. If there are five laminate layers, then the overall thickness of the Mg based laminated composite would be ~2.5 mm, and there are ~61 vol% Mg alloy and ~39% CF/PEEK.

2.2.2 Tensile tests of Mg/CF/PEEK laminated composites

Tensile tests were conducted in accordance with the ASTM standard E8M-89. The gauge length is set to be 40 mm, as shown in Fig. 2.4. The loading direction is parallel to the longitudinal or transverse fiber direction, and the loading strain rate is ~$4x10^{-4}$ s^{-1}. A strain gage was attached on the gauge for the measurement of elastic modulus and failure elongation. In order to estimate the dependence of tensile properties on working temperature, three sets of testing temperatures, including room temperature, 100^{o}C, and 150^{o}C, were adopted to perform. The fractured specimens are observed by a JEOL JEM-6400 scanning electron microscope (SEM), operating at 20 kV.

2.2.3 Flexural and T-Peel tests of Mg/CF/PEEK laminated composites

The flexural properties of the Mg/CF/PEEK laminated composites were explored by the three-point bending tests in this study according to the ASTM D790-02 specification. The dimensions of specimens were 100 mm in length, 12.7 mm in width, and 2.8 mm in thickness, as shown in Fig. 2.5. The longitudinal and transverse specimens of the Mg/CF/PEEK laminated composites were both tested, with a span-to-depth ratio of 28:1 at a strain rate of $1.7x10^{-4}$ s^{-1}.

T-peel tests of the Mg/CF/PEEK composites were conducted according to the specification of ASTM D1876-95. In order to reveal the bond strength between the Mg and APC-2 layers, a three-layer Mg/APC-2/Mg laminate was specially fabricated for this purpose. The thicknesses of the AZ31 Mg and APC-2 prepreg were both about 0.6 mm, as shown in Fig. 2.6. The longitudinal and transverse specimens of the Mg/CF/Mg laminates were both tested. The crosshead speed of 4.2 mm/s was applied, corresponding to a bond separation rate of 2.1 mm/s. To examine the bonding characteristics, the tested specimens were observed by optical microcopy (OM) or scanning electron microscopy (SEM).

2.2.4 Identification for interface bonding between Mg sheet and APC-2 prepreg

In order to investigate the interface bonding occurring between the Mg sheet and the APC-2 prepreg, the FT-IR spectroscopy was applied to characterize whether the interface bonding could be chemical or physical.

For FT-IR characterization, a Biorad FTS 6000 FT-IR spectrometer with ATR (Attenuated total reflection) objective was applied. The Mg/CF/PEEK laminated composites were peeled along the interface between Mg sheet and APC-2 prepreg, and these freshly peeled faces, including the CrO_3 etched or non-etched Mg sheets and the APC-2, were scanned by the FTS

6000 FT-IR spectrometer.

2.3 Nanoparticle/PEEK composites

2.3.1 Preparation of nanoparticle/PEEK composites

Since it is not possible to measure the volume amount for the nanoparticles when they are in powder forms, the addition of nanoparticles was measured by weight percent (wt%), from 2.5 to 10 wt%. Owing to the higher densities of SiO_2 and Al_2O_3 than that of PEEK, the transformed volume percent (vol%) would be lower, as summarized in Table 2.1. Note that the Al_2O_3 particles were added in lower amounts in volume as compared with the SiO_2 counterparts. Meanwhile, the maximum amount in volume fraction was 4.9 vol% for SiO_2 and 3.3 vol% for Al_2O_3, considerably lower than the 15 to 50 vol% for the conventional polymeric or metallic composites. This means that the current nanocomposites would not alter much the processability or density of the PEEK matrix.

PEEK nanocomposites were fabricated by means of vaccum compression molding, as shown in Figs. 2.7 and 2.8, at 400^{o}C under a load of 60 MPa. Prior to compression molding, the fine PEEK powders (~100 μm) were completely mixed with the nanoparticles (SiO_2 or Al_2O_3) through ultrasonic vibration in alcohol medium, and then the well-dispersed sol was dried at 80^{o}C to remove the excess alcohol.

2.3.2 Room temperature tensile tests of nanoparticle/PEEK composites

Room temperature tensile testing was conducted in accordance with the ASTM standard E8M-89. The gauge length was set to be 40 mm, as shown in Fig. 2.9, and the crosshead

speed was 1 mm/min, corresponding to a strain rate of $4x10^{-4}$ s^{-1}. Strain gauge was attached to the gauge for measurements of elastic modulus and failure elongation.

2.3.3 Microhardness tests of nanoparticle/PEEK composites

A Shimadzu HMV-2000 Vickers microhardness tester was applied to evaluate the microhardness enhancement. The specimens were subjected to a load of 50 g for time duration of 15 s.

2.3.4 SEM energy dispersive spectrometry (EDS) and X-ray diffraction

A JEOL-JSM 6400 scanning electron microscope (SEM) equipped with energy dispersive spectrometry (EDS) was used to evaluate the nanoparticle dispersion condition. Also, a Siemen D5000X X-ray diffractometer with Cu K_α radiation was applied to investigate the effects of the filled nanoparticles on the crystallization degree of the PEEK resin.

2.3.5 TEM observations on nanoparticle/PEEK composites

A JEOL 3010 transmission electron microscope (TEM) was used to evaluate the nanoparticle dispersion condition. The thin foil TEM specimens were prepared by microtome with a diamond knife, and examined in TEM operated at 150-200 kV. For better TEM image quality, all the ultra thin films were cut to be 50 nm in thickness.

2.3.6 Thermal analysis of nanoparticle/PEEK composites

The effects of the filled nanoparticles on the crystallization behaviors of the PEEK polymer were evaluated using a Perkin-Elmer differential scanning calorimeter (DSC Pyris 1). The weights of all samples were about 3-5 mg, and these samples were heated to 410^{o}C at a heating rate of 10^{o}C /min under nitrogen atmosphere, and held for 5 min to remove the previous thermal history. Non-isothermal crystallization was investigated by cooling the samples from 410 to 50^{o}C at various cooling rates of 2.5, 5, 10, 15, 20, 25, and 30^{o}C/min.

The effect of the filled nanoparticles on thermal stability of PEEK was estimated using a Perkin-Elmer thermogravity analyzer (TGA Pyris 1), running from 25 to 700^{o}C at a heating rate of 10^{o}C/min under nitrogen atmosphere.

Chapter 3 Experimental Results

3.1 Mg/CF/PEEK laminated composites

3.1.1 Fabrication of Mg/CF/PEEK laminated composites

Initially, the fabrication of the Mg/CF/PEEK laminated composite encountered numerous difficulties. It took more than six months to render this composite into a level to expose its high performance potential. As mentioned in Chapter 1, CARALL has been successfully fabricated by simply laminating the aluminum alloy and the carbon fiber prepreg [146]. The exploration of the Mg/CF/PEEK laminated composite was, initially, conducted following the routes for aluminum base composites. Firstly, the fabrication of this composite was carried out by means of merely laminating the AZ31 alloy sheet with the APC-2 prepreg without any pretreatment. AZ31 Mg sheets, 2 mm in thick initially, were rolled to the thickness of about 0.5 mm. Two to four layers of APC-2 prepreg were stacked closely to form an APC-2 layer of ~0.5 mm, and then packed with Mg to a sequence of Mg/APC-2/Mg. Varying in the number of layers of APC-2 prepreg was performed in order to estimate the relationship between the bonding ability and the amount of PEEK resin present. The temperature of lamination was set to be 400^{o}C under a pressure of 1.4 MPa [38] during vacuum hot pressing. No roughening on the AZ31 surface and no surface etching were applied initially. Due to the poor bonding characteristics between the Mg alloy and the carbon fiber, large differences in surface energies intrinsically, the resulting laminated Mg based composite shows the severe delamination at the interface between the APC-2 prepreg and the Mg sheet, as well as outflow of PEEK resin and carbon fibers. It is conceivable that the poor bonding issue and the large difference of coefficient of thermal expansion (CTE) should be responsible for the delamination. The improper and non-uniform pressuring during lamination was the main clue

for the outflow of PEEK resin and carbon fibers.

A rough surface could result in better bonding between the Mg alloy and the PEEK resin. Accordingly, the AZ31 alloy was roughened with a #100 SiC abrasive paper to make a rough bonding surface and to remove the oxides present at the Mg surface prior to laminating with APC-2 prepreg. Consequently, the resulting laminated composite revealed a slight improvement in the interface bonding, as compared with the laminated composite without any surface pretreatment, but the problem of delamination still occurred.

In order to overcome the delamination problem, a polyolefin-based adhesive was firstly tried. Three layers of polyolefin adhesive films with a layer thickness of ~0.1 mm were placed between the AZ31 sheet and APC-2 prepreg to act as a binder. The AZ31 sheets were also roughened with SiC abrasive paper prior to lamination. The forming temperatures were kept low at 200^{o}C in preventing from adhesive decomposition, with the same forming pressure of 1.4 MPa and time duration of 15 min. It was shown that the Mg/APC-2 laminate bonded with a 3-layer polyolefin adhesive at 200^{o}C showed no delamination at the interface, but the adhesive would be squeezed by the forming pressure and flow out of the sheets. The viscous flow of the adhesive could result in sliding of the AZ31 sheet and the APC-2 prepreg with each other under a pressure of 1.4 MPa at 200^{o}C. A lower holding temperature coupled with a lower forming pressure would reduce the sliding problem, but the bonding quality became degraded. The adhesive seemed to offer a bonding with minimum delamination; however, the bonding strength was found to be low. It appears easy to tear off the lamina from the interface. Meanwhile, the service temperature of the bonded laminated composite with adhesive would be again lower than 100^{o}C.

In addition to the use of polyolefin-based adhesive, chemical etching on Mg alloy seems

to be important to produce a surface with affinity to PEEK resin. With this concern, the picric acid ($(NO_2)_3C_6H_2OH$) based etchant was applied to enhance the interface affinity. The fabrication of the laminated composite was, again, carried out without any application of polyolefin-based adhesive, except that the Mg sheets were etched by the picric acid. As a result, this etchant could yield better bonding, but partial delamination still occurred from the composite edge. Except for the use of picric acid and many acid chemicals tried in follow, it was later found that the CrO_3/HNO_3 based coupling agent could result in satisfactory bonding. The laminate pretreated by this coupling agent reveals no delamination throughout the processing and subsequent storage. As shown in Figs. 3.1 to 3.7, the poor bonding aspect was improved by such proper pretreatments, including surface roughening and chemical etching. But the main problem was still present, that is the outflow of PEEK resin and carbon fibers during lamination. In Figs. 3.1 to 3.7, the bonding temperature was kept at 400^{o}C, and the pressures were varied from 0.7 to 1.4 MPa. The other changes in the fabrication conditions were the number of plies in the APC-2 layer and the stacking sequence. It is shown that no matter how the changes in the conditions of fabrication, there is still a problem of outflow in PEEK resin carbon fibers.

It was later advised by Professor Kao [146] that the outflow of PEEK resin and carbon fibers could be solved completely by proper and uniform pressuring on the laminated composite during fabrication. Thus, the follow-up was conducted in Professor Jen's lab, Department of Mechanical and Electro-Mechanical Engineering, NSYSU, using another kind of vacuum hot press suitable for laminating polymer based composites. And the etchant was changed to be the combination of CrO_3 and Na_2SO_4. The stacking sequence was finalized to Mg/APC-2/Mg/APC-2/Mg. At first trial on this FRP-suitable vacuum hot press, the Mg/CF/PEEK laminated composite was successfully fabricated. It reveals no delamination and no resin or fiber outflow. The bonding characteristics between the Mg alloy and the

APC-2 appear satisfactory.

The laminate pretreated by this promising coupling agent, i.e. CrO_3/Na_2SO_4, revealed no delamination throughout the processing, subsequent machining and tensile loading. The possible postulated reactions are below:

$$CrO_3 \xrightarrow{H_2O} H_2CrO_4 \qquad (3.1)$$

$$H_2CrO_4 + Mg^{2+} \longrightarrow MgCrO_4 + 2\,H^+ \qquad (3.2)$$

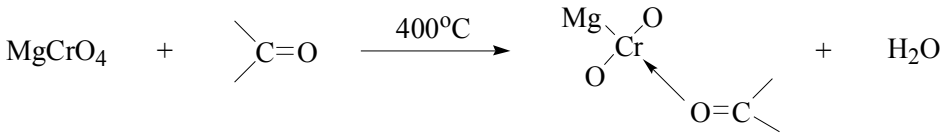

PEEK Coordination (3.3)

The electron configuration of chromium might account for the unique characteristics of the CrO_3 based coupling agent; the unoccupied d orbital in the electron configuration of the chromium atom could make its ion characteristically forming coordination compounds [153]. In this case, the oxygen atom in the backbone of PEEK has lone-paired electrons and, consequently, this oxygen atom may be able to form a ligand bonding to the chromium ion, resulting in coordinate covalent bond. Instead of the week van der Waals bonding formed between Mg and PEEK when using other surface echants, the laminate pretreated with chromium oxide base coupling agent could impart a characteristic coordinate covalent bond at the interface between the APC-2 prepreg and Mg phase. As a consequence, this laminate exhibited a good bonding and no delamination along the interface during slow or rapid cooling, as well as following aging and machining.

Figure 2.3 shows the enlarged schematic drawing of the resulting Mg based laminated composite, containing five layers. The thickness of the resulting laminated composites depends on the layer number. For example, a five layer composite containing three Mg foils (each ~0.55 mm thick) and two APC-2 plies (each ~0.55 mm thick with 4 APC-2 layers) will measure ~2.7-2.8 mm in thickness. In that case, the resulting Mg bases composite after hot pressing would contain 61 vol% AZ31 Mg and 39 vol% APC-2 prepreg (i.e., ~24 vol% carbon fibers and ~15 vol% PEEK polymer).

3.1.2 Room temperature tensile properties

The room temperature ultimate tensile stress-strain curves loaded at $4x10^{-4}$ s^{-1} for the longitudinal and transverse specimens are shown in Figs. 3.8(a) and 3.9(a), respectively. The enlarged view of the elastic portion is shown in Figs. 3.8(b) and 3.9(b), in which the Young's modulus for the Mg/CF/PEEK laminated composite was calculated. Table 3.2 lists the data on the experimentally measured mechanical properties of the AZ31 Mg matrix, the reinforcement layer (CF/PEEK) and the Mg/CF/PEEK composite.

As shown in Table 3.2, the laminated Mg composite exhibits anisotropic behavior. The ratios of the stiffness and tensile strength along the longitudinal and transverse directions are 2.4 and 4.9, respectively. Along the longitudinal direction, the stiffness increases from 45 GPa of the AZ31 Mg base alloy to 75 GPa of the composite; and the strength increases from 290 MPa of AZ31 to 932 MPa of the composite, both significant increments. It appears that the current fabrication method for the Mg/CF/PEEK laminated composite is feasible, effective, and easy-to-process, as compared with the liquid metal infiltration method mentioned above. As for the transverse properties, the composite offers a Young's modulus of 31 GPa and a tensile strength of 188 MPa, which are lower than the base metal AZ31 Mg.

This is typical for uniaxially continuous fiber reinforced composites. But the transverse properties are still superior to the PEEK polymer, especially for the modulus.

The longitudinal specific stiffness and specific strength, with the consideration of density, of the Mg/CF/PEEK laminated composite are about 2-3 times of those of AZ31 (Table 3.2). In other word, when applied as a long beam or long plate, the Mg/CF/PEEK laminated composite provides a much more promising material than the Mg alloys for the purpose of weight-saving structural characteristics. Even for the transverse specific stiffness and specific strength, the composite also possesses reasonable specific properties.

3.1.3 Elevated temperature tensile properties

As mentioned above, the Mg/CF/PEEK laminated composites possess excellent tensile properties at room temperature. In order to investigate the upper service temperature of the composites, the composites were tensile-tested at elevated temperatures. It is well known that the PEEK polymer has a glass transition temperature of 143^{o}C. Accordingly, the tests were carried out at temperatures of 100 and 150^{o}C, below and above T_g.

As shown in Table 3.3 and Figs. 3.10 to 3.11, for both the longitudinal and transverse directions, the UTS data decrease with the increasing loading temperature. Furthermore, the UTS decrement degree with increasing temperature for the longitudinal composite is significantly lower than the transverse counterpart, being -5.9% for the longitudinal specimen and -23.4% for the transverse one at 150^{o}C. The reason accounting for this difference is that the PEEK resin plays the predominately important role in bonding the Mg and carbon fibers along the transverse direction. PEEK is more sensible to temperature than the Mg alloy. The same effect can also be found for the trend of the tensile elongation.

It was reported that the UTS of AZ31, grain size 5.0 μm, at room temperature and 150^{o}C are 290 and 150 MPa, respectively, under a strain rate of 1x10^{-4} s^{-1} [154]. Accordingly, the UTS of AZ31 alloy at 100^{o}C could be estimated to be around 230 MPa. The UTS decrements of AZ31 alloy at 100^{o}C and 150^{o}C, based on the UTS at room temperature, are -20.7% and -48.3%, respectively. As shown in Table 3.3, the decrements on the Mg base laminated composites at 100^{o}C and 150^{o}C along the longitudinal direction are only -2.4 and -5.9%, respectively. Obviously, the UTS decrement in the Mg base laminated composite are much lower than that of the pristine Mg alloy when the temperature is up to 150^{o}C.

Consequently, the carbon fibers in the Mg base laminated composites play the very important role, enduring predominantly the tension load. On account of the PEEK resin, it is supposed that the PEEK resin could play the role that binds the two phases, Mg and carbon fiber, closely together. As shown in Table 3.3, the UTS values of the laminated composites at elevated temperatures are still as high as 900 MPa, which are about 3, 4, and 6 times the neat Mg alloy at room temperature, 100^{o}C, and 150^{o}C, respectively. It is obvious that the interface bonding is sufficient even the service temperatures are up to 150^{o}C, slightly higher than the glass transition temperature of the pristine PEEK.

3.1.4 SEM observations

As shown in Fig. 3.12(a), there are fiber pull-out and carbon fiber broken phenomena in the APC-2 layer under the longitudinal tensile loading, accounting for the load transfer of tensile stress from matrix to carbon by means of interfacial shear stress. In Fig. 3.12(b), it is apparent that the failure positions of Mg and fibers are closely related. Good bonding between APC-2 and Mg is evident. Occasional de-bonding of PEEK resin and carbon fibers within APC-2 can also be seen in Figs. 3.12(b) and 3.12(c). The ductile behavior of the AZ31

Mg matrix can be realized by the abundant dimples in Fig. 3.12(d). It seems that the overall failure of the laminated composite, under longitudinal loading, starts from Mg failure, and ends with carbon fiber broken and pull-out. Multiple failure modes were observed, also evident from the multiple jerky steps in Fig. 3.8(a). The load transfer from the Mg matrix to continuous fiber seemed to be highly efficient.

On the other hand, much simpler failure was observed when loaded along the transverse direction. The fracture surfaces of both Mg and APC-2 are flat, as shown in Fig. 3.13(a) and the flow stress curve in Fig. 3.9(a) is also smooth until near overall fracture. Occasional delamination between Mg and APC-2 can be seen in Fig. 3.13(b), and this delamination behavior seems to be responsible for the sudden drop of flow stress at e~0.02-0.026 in Fig. 3.9(a). As tilted to near edge-on for the fibers, debonding between carbon fiber and PEEK has been found, as indicated by arrows in Fig. 3.13(c). The fiber itself would carry no load under transverse tests. The fracture mode in Mg in Fig. 3.13(d) appears the similar for both the transverse and longitudinal specimens. The final failure at ~188 MPa seems to correspond to the fracture of Mg matrix, since it partitions the same ratio of load (188 MPa over 290 MPa for the UTS of the Mg matrix, i.e. 188/290 or ~65%) as its volume fraction (~61%).

Figures 3.14 to 3.17 show the fracture behaviors at elevated temperatures. In Fig. 3.14(a), the longitudinal laminated composite loaded at 100^{o}C exhibited fiber breakage and pull-out. In Fig. 3.14(b), the positions of the fiber failure and the micro-crack are closely related to the Mg phase. Near the fracture tip-point where Mg alloy started to fail, the tensile load was transferred to the carbon fiber through shear stress, which finally resulted in carbon fiber breakage and pull-out. These fracture sequences are basically similar to the composites loaded at room temperature. It is can be seen that the transfer of the shear force through the

interface between the APC-2 and Mg phases is still effective and satisfactory even at a service temperature of 100^{o}C. Accordingly, the effective and satisfactory shear force transfer could account for the very minor decrement in UTS at 100^{o}C.

In view of the fractured specimen tested at 150^{o}C, as shown in Fig. 3.15, the similar fiber breakage and pull-out can also be seen. In Fig. 3.15(a), the fracture of the laminated composite seems to be somewhat more severe, as compared with that of the specimens tested at room temperature and 100^{o}C. Nevertheless, the transfer of the shear force through interface did not seem to be degraded much even the service temperature up to the T_g of the PEEK resin.

As for the transverse laminated composites, Figs. 3.16(a) and 3.16(b) show the interface delamonation between the Mg and the APC-2 phases at 100^{o}C. As shown in Fig. 3.16(a), the dimples in the Mg phase indicate the ductile fracture behavior when the composite is subjected to a tensile load. For the transverse specimen, the Mg alloy carries the most of tensile load, as shown in Fig. 3.16(a), and the carbon fibers in the APC-2 phase just play a role of filler. These carbon fibers are bonded together with Mg phase by means of the PEEK resin, and they should carry no load. There are cracks present at the Mg and APC-2 phases, as shown in Fig. 3.16(b), indicating the tensile load was shared by Mg matrix and the PEEK resin.

Figures 3.17(a) and 3.17(b) show the failure of the interface between the Mg and the APC-2 phases, and the de-attachment of the carbon fiber, respectively, at 150^{o}C. In Fig. 3.17(a), the fracture points in interface are zigzag and scattered. It is evident that the fracture behavior at 150^{o}C seems to be more ductile as compared with the counterparts at room temperature. The ductile fracture characteristics are present not only in the Mg phase but also

in the APC-2. Also in Fig. 3.17(a), the failure points in APC-2 could not only take place at the fracture zigzag interface, it could also occur just close to the interface, about 100 to 200 μm away from the interface.

3.1.5 Room temperature flexural and peel properties

3.1.5.1 Room temperature flexual properties

It is well known that the hybrid laminated composites exhibit highly anistropic characteristics and cause a mismatch in mechanical properties between individual laminae within the laminate. Such anistropic natures could in turn produce delamination initiation and propagation. The three-point bending loading for the current composite beam can provide the information such as the apparent interlaminate shear strength (ILSS). According to the specification of ASTM D790-02, the flexural stress σ_f can be estimated by

$$\sigma_f = 3PL/2bd^2, \tag{3.4}$$

where P, L, b, and d are the ultimate load, free span, width and depth of the beam tested, respectively. And the flexural strain ε_f can be also determined by

$$\varepsilon_f = 6Dd/L^2, \tag{3.5}$$

where D is the maximum deflection of the center of the beam.

Figures 3.18 and 3.19 show the flexural stresses and moduli of the longitudinal and transverse specimens of the laminated Mg/CF/PEEK composites. As shown in Fig. 3.18, the

flexural modulus, stress and strain along the longitudinal direction of the Mg based laminated composite are 61.8 GPa, 960 MPa and 0.03, respectively. These high flexural stress and modulus might be due to the sound interfacial bonding between Mg and APC-2. On the other hand, the flexural modulus, stress and strain along the transverse direction of the Mg based laminated composite are 36.5 GPa, 318 MPa and 0.07, respectively. It is obvious that the carbon fibers arrayed in the longitudinal configuration could impart significant contribution in carrying the load, and effectively enhancing the bending resistance of the laminated composite. However, the fibers in the transverse configuration seem to play a much more minor role. The flexural properties revealed are basically a reflection from the behavior of the AZ31 Mg sheets, similar to the tensile case. In comparison with the CF/PEEK prepreg polymer composite [155], the Mg/CF/PEEK Mg based composite shows a slightly lower flexural and tensile modulus and strength along the longitudinal direction, but appreciably higher modulus and strength along the transverse direction, due to fact that Mg is still much stronger than the PEEK matrix.

To account for the large differences in the flexural properties along the longitudinal and transverse directions, the fractured specimens were carefully examined, as shown in Fig. 3.20. In Fig. 3.20(a), it suggests that the interface bonding between Mg sheet and APC-2 prepreg is sufficiently strong. The failure behavior in the longitudinal specimen was found to be of multiple modes and an overall failure phenomenon. Carbon fibers were broken and delaminated inside the APC-2 layer of the laminated composite. The outer Mg layer was completely fractured, and the inner Mg layer was squeezed convexly. The interface just adjacent to the failure position of the outer Mg layer showed no apparent delamination. However, delamination occurred at the inner layer counterpart. In contract, the fractured phenomena in the transverse configuration are significantly different to those of the longitudinal counterpart, as shown in Fig. 3.20(b). It is a more simple failure behavior. The

composite showed much higher flexural strain, and until flexural strain of 0.07 only the outer Mg sheet APC-2 layers were fractured. The carbon fibers in the outer APC-2 layer of the transverse specimen were simply separated each other. Overall, the interface bonding between APC-2 and Mg appears to be sufficient, as evident from the flexural and tensile tests.

3.1.5.2 Room temperature peeling properties

It was proposed earlier that the interfacial bonding strength between the APC-2 prepreg and the Mg sheet would be strongly affected by the surface treatment during the fabrication processes. It is meaningful to estimate the interfacial bonding strength of the current laminated composites and to compare with the epoxy-resin-adhered Aluminum/CFRP composites [156].

In this study, the T-peel method was adopted to determinate the interfacial strength. For the T-peel specimens, the right-angled tabs were adhesively bonded to the ends of the Mg/APC-2/Mg laminated composites. The APC-2 layer contains five foils of the APC-2, or CF/PEEK, prepregs with the carbon fibers undirectionally stacked within the PEEK matrix. Three tests were applied for both the longitudinal and the transverse specimens. The longitudinal and the transverse specimens were determined to be 2.75 ± 0.25 N/mm (2.90, 2.86, 2.49 N/mm) and 4.85 ± 1.5 N/mm (4.18, 3.73, 6.63 N/mm), respectively. The typical peel test results of the CrO_3 treated composites are shown in Fig. 3.21. The higher peel strength for the transverse specimens might be due to the higher resistance to be peeled when the peel path is perpendicular to the aligned carbon-fiber direction. The peel strength variation for the transverse specimens is also higher. These peel strength values are lower than the diffusion or fusion bonding in metallic systems (~30 N/mm) [156], but superior to

adhesive bonding of the epoxy-resin-adhered Aluminum/CFRP composites (~1 N/mm) [157].

The OM micrographs taken from the peeled specimens show that there are many carbon fibers stuck on the Mg foil after peeling, Fig. 3.22 (b). And this can be attributed by the sound interfacial bonding characteristics between the Mg sheet and the APC-2 prepreg. In comparison of the pretreatments of Mg foil with or without CrO_3, Fig. 3.22(a) and 3.22(b), it is apparent that the Mg foil pretreated with CrO_3 etchant shows much better interfacial bonding characteristics.

3.1.6 Characterization on interface bonding between Mg sheet and APC-2 prepreg

It is apparent that there is a sufficiently strong interface bonding occurred between the Mg sheet and the APC-2 prepreg, and this strong interface bonding in turn imparts the high mechanical properties, including the highly improved elastic modulus, UTS, and flexural strength, in the resulting Mg/CF/PEEK laminated composites. It is interesting to characterize the bonding nature at the interface between Mg and APC-2 prepreg. Accordingly, a Biorad FTS 6000 FT-IR spectrometer with ATR (attenuated total reflection) objective was applied to characterize whether a coordination bonding was resulted in between the CrO_3-etched Mg sheet and the PEEK resin.

Figure 3.23 shows the chemical structure of the PEEK polymer, and it is well known that there are many carbonyl groups (C=O) in its backbone. Accordingly, there should be plenty of lone-paired electrons present around the oxygen atoms. As the previous postulate, mentioned in Sec. 3.1.1, the electron configuration of chromium might account for the unique characteristics of the CrO_3 based coupling agent; the unoccupied d orbital in the electron configuration of the chromium atom could induce its ion to characteristically form

coordination compounds [153].

The four specimens examined by FT-IR are the AS-4 prepreg, the etched and unetched CF phases peeled from the laminated composites, and the etched Mg-phase peeled from the laminated composite. All the characterizations the IR beams were struck on the localized PEEK-rich phase. The characteristic absorption frequencies associated with the four specimens are listed in Table 3.4. As shown in Table 3.4, there is no significant difference on the characteristic absorption frequencies among the four specimens.

It is well known that a saturated aliphatic ketone has an absorption frequency about 1715 cm^{-1} [158]. Conjugation with a C=C bond results in delocalization of the π electrons of both unsaturated groups. Delocalization of the π electrons of the C=O group reduces the double-bond character of the C-O bond, causing absorption at lower wave-numbers (or longer wavelengths). Conjugation of carbonyl group with an alkene or phenyl group causes absorption in the 1685-1650 cm^{-1} range. As shown in Table 3.5 and Fig. 3.24, the native AS-4 prepreg has the C=O stretching absorption at about 1653 cm^{-1}. Intermolecular coordination bonding between a ketone and a chromium ion will cause a slight decrease in the absorption frequency of the carbonyl, i.e. the wave-number of the carbonyl group will shift to a lower ones.

However, as shown in Figs. 3.24(a) to (d) and Table 3.4, the characteristic absorption frequencies of carbonyl groups in the four specimens make no significant difference. In other word, there is no apparent evidence to confirm the previous postulate that the oxygen atom may be able to form a ligand bonding to the chromium ion, resulting in coordinate covalent bond. Therefore, it is supposed that the physical intermolecular entanglements may be responsible for the sufficient interface bonding.

3.2 PEEK composites reinforced by nano-sized SiO_2 and Al_2O_3 particulates

3.2.1 Microhardness measurements

As shown in Fig. 3.25 and Table 3.6, the H_v microhardness readings increased all the way from 21.7 of the pure PEEK polymer to 32.5 in the 10 wt% 15 nm SiO_2 filled composites, implying a maximum increment percentage of 50%. It has been shown that a composite with a higher hardness value will be accompanied with a lower wear rate and friction coefficient [54-56]. Note that the hardness increment in the SiO_2 filled composites is consistently higher than that in the Al_2O_3 filled ones. However, the intrinsic hardness of the SiO_2 (Mohs scale of 7, and H_v scale around 1000) in glass phase is generally considerably lower than that of Al_2O_3 (Mohs scale of 9, and H_v scale around 1500). The lower H_v for the Al_2O_3 filled composite is thought to result partly from the lower Al_2O_3 volume fraction (Table 2.1). The same trend will also be seen from the elastic modulus measurement. Meanwhile, in comparison with the same SiO_2 particles but with different sizes of 15 and 30 nm, the composites with finer nano particles show a continuous and linear hardness increment even at the highest SiO_2 content of 10 wt%. It seems that the finer 15 nm particles could be more uniformly distributed and contributed the continuous hardness improvement, as discussed later on the base of modulus and UTS data.

3.2.2 Room temperature tensile properties

The variations of the average data on the Young's modulus (E), ultimate tensile strength (UTS), and failure elongation (e) as a function of nanoparticle content are shown in Fig. 3.26. The continuous increasing trend of the elastic modulus up to 10 wt% nanoparticles, as depicted in Fig. 3.26(a), resembles to that for the hardness. The highest increment occurs in

the silica composites with 10 wt% 30 nm SiO_2; raising the PEEK modulus of 3.9 GPa up to 5.3 GPa (or an increment percentage of 36%, Table 3.6). In comparison, the 30 nm Al_2O_3 nanoparticles provide a slightly lower improvement in the elastic modulus, the same as the situation in hardness, presumably due to the lower volume fraction. As for the SiO_2 nanoparticles with a finer size of 15 nm, the modulus increment was further lower, suggesting that extrafine particles might not be able to elaborate their full strengthening capability in stiffness enhancement. Nevertheless, the more uniform spatial distribution of the finer particles might result in higher strengths as seen later, and higher hardness as mentioned early. The lower modulus should not be owing to a severer nanoparticle clustering since the tensile elongation of this composite is appreciably higher, and the hardness and UTS show continuously increasing trend. It seems that, with the same amount of nanopartilces, finer ones would result in more free volume space between the filled particles, and the polymer chain segments would in turn deform themselves in a more mobile manner, accounting for the lower Young's modulus and higher failure strain.

As for the UTS, there shows a maximum peak for all three composites, occurring at a SiO_2 or Al_2O_3 content of 5.0-7.5 wt%, as depicted in Fig. 3.26(b) and Table 3.6. The 15 nm SiO_2 composites behave better, with nil decrement in the 10 wt% samples, suggesting the best spatial distribution at high filler contents. With a greater amount of nanoparticles, the strength starts to decrease due to local particle clustering and pre-matured failure. Even the Young's modulus and hardness are still increasing at 10 wt%, the UTS reveals the reversed trend. The highest UTS improvement occurs in the composites with 7.5 wt% 30 nm Al_2O_3 to 108 MPa, or an increment percentage of 21% (Table 3.6).

Nevertheless, the tensile failure elongation continuously drops from the 12% of the unreinforeced PEEK to 4-6% in the 10 wt% nanocomposite, as depicted in Fig. 3.26(c) and

listed in Table 3.6. Composites with the 15 nm nanoparticles consistently exhibit higher tensile elongations than the 30 nm counterparts, suggesting a lower degree of particle clustering and particularly a higher flexibility of PEEK matrix deformation, as discussed above. Note that in Fig. 3.26(c) the elongation data on the 30 nm Al_2O_3 filled composites are all higher than those on the 30 nm SiO_2 counterparts, and might be restricted to the lower Al_2O_3 volume fraction.

3.2.3 SEM observations

It is well known that the nanoparticles would agglomerate together in the polymer matrix, and in turn decrease the reinforcing effects. The nanoparticles are difficult to be well resolved by the secondary or back scattering electron images under SEM, since the contrast is generally weak. With the help of EDS, it is possible to roughly estimate the dispersion condition of the nanoparticles. Figure 3.27 shows the Si or Al EDS mappings for the 5 and 7.5 wt% 30 nm nanocomposites. It is seen that the dispersion condition of silica and alumina nanoparticles in the PEEK matrix are reasonably uniform in the 2.5 and 5 wt% composites. Nevertheless, the agglomeration degree increases with increasing nanoparticle content, particularly for the 10 wt% ones. This is postulated to be caused by the greater viscosity of the PEEK/nanoparicles mixture at higher nanoparticle contents during the hot press processing.

By closer examinations, the local clustering effect is less severe in the Al_2O_3 composites. This is postulated to be caused by the lower volume fraction of Al_2O_3 making the particle flow and dispersion in the PEEK matrix to proceed more smoothly. It is also consistent with the observation that the 30 nm SiO_2 composites start to decline in UTS at 7.5 wt%; while the Al_2O_3 composites still show strengthening at 7.5 wt% (Fig. 3.26(b) and Table 3.6).

Meanwhile, the agglomeration is also less pronounced in the 15 nm composites. It follows that the UTS of the 15 nm SiO_2 composites remain its high level even at 10 wt%. It is conceivable that, with further improvement of nanoparticle clustering via particle surface modification, though more expensive, the mechanical properties can be further upgraded. However, for wear rate reduction, the current simple processing route appears to be adequate.

3.2.4 TEM observations

Systematic examinations on the dispersion of the nano SiO_2 or Al_2O_3 particles in various composite specimens have been conducted. Figures 3.28 to 3.30 present some typical examples of the TEM micrographs taken from the silica or alumina filled PEEK composites. Although there are occasionally clustering occurrences for two to night nanoparticles to cluster or align together, but the majority of the nanoparticles were seen to disperse semi-homogeneously in the PEEK matrix.

As shown in Fig. 3.28, the dispersion of the 15 nm silica particles in PEEK matrix appears to be reasonably well. There are some nanoclusters, 8-10 aligned together in maximum, in the PEEK matrix. However, there are also many isolated particles or smaller nanoclusters with 2-4 particles aligned together. Hence, the overall dispersion of the 15 nm silica particles in PEEK is fair, and the agglomeration of nanoparticles did not be severe.

The dispersion of the 30 nm silica or alumina in PEEK resembles the case of the 15 nm silica, as shown in Figs. 3.29 and 3.30, respectively. Figure 3.31 shows the dispersions of 15 nm silica and 30 nm alumina particles in PEEK polymer. As shown in Fig. 3.31, there are nanoparticles scattered individually. However, the most particles dispersed in 3-5 particles aligned together.

The relatively satisfactory dispersion of the current SiO_2 or Al_2O_3 particles, independent of 15 or 30 nm in size, may be due to the sound mixture through ultrasonic vibration in alcohol medium, as well as the high load applied during the forming. The latter would force the highly viscous PEEK polymer to flow, during the intensive flow the nanoparticles would be forced to disperse separately.

3.2.5 X-ray diffraction analysis

For better understanding of the possible chemical interactions between the nanoparticles and the PEEK matrix, X-ray diffraction was applied to determine the effect of filler content on the *d*-spacing of the crystalline PEEK. With the addition of silica or alumina nanoparticles from 2.5-10 wt%, there is no extra peak created or disappeared as compared with those of the pure PEEK, as shown in Fig. 3.32. The SiO_2 or Al_2O_3 diffractions are too low to be resolved in Fig. 3.32. It appears that there is no apparent interaction that would result in appreciable new interfacial phases. The weaker diffraction intensity in composites with a high amount of nanoparticles was mainly due to the smaller PEEK crystallites, coupled with the lower PEEK weight fraction. For the composites with a high fraction of nano particles (e.g. 10%), a lower degree of crystallization might sometimes occur, since the PEEK matrix filled with abundant SiO_2 or Al_2O_3 would decrease the mobility of the polymer chain segments during the period of crystallization [159-161], as further discussed in the next section.

3.2.6 DSC analysis on nonisothermal crystallization

The nonisothermal crystallization behaviors of the nanocomposites were studied by DSC, cooling the samples from 410 to 50^{o}C at constant cooling rates of 2.5, 5, 10, 15, 20, 25, and 30^{o}C/min. As shown in Figs. 3.33 to 3.37, the crystallization initiation, peak, and finishing

temperatures, T_{ci}, T_{cp}, and T_{cf}, shift to lower temperatures, for both the PEEK and nanoparticle-filled PEEK, as the cooling rate increases. The faster the cooling rate, the more supercooling is required to initiate the crystallization of the PEEK chain segments, since the motion speed of the PEEK chain segments could not catch up the cooling rate [137]. Following the cooling step, the subsequently heating step of the PEEK nanocomposites shows no significant change on the melting points, T_m, of both the filled and unfilled specimens in the DSC diagrams, as shown in Figs. 3.38 to 3.42. The melting temperatures are mostly scattered within 338 ± 2^oC, in the typical range of $330\text{-}385^oC$ for the PEEK resin [162, 163]. As for the addition of nano particles on the crystallization of PEEK, there are several factors involved; some of them are counteracting each other making the net effect obscure sometimes. For example, in terms of heterogeneous nucleation of PEEK on the nano particle interfaces, the crystallization initiation and peak temperature might increase. However, the obstacle effect from the nano particles on the PEEK mobility and crystallization would lower the crystallization temperatures. Tables 3.7 to 3.9 summarize the data on T_m, T_{ci}, T_{cp}, T_{cf}, and the crystallization enthalpy, H_c, for the pure PEEK and nanocomposites.

It is suggested [138,139] that the inclusion of inorganic fillers would lower the crystallization temperature of the resulting nanocomposites under non-isothermal crystallization process. There are two major effects acting simultaneously when the inorganic particles filled polymer undergoes crystallization. One is the decrease in mobility of the chain segments, and the other is the heterogeneous nucleation. Lowering in molecular mobility would play a reverse effect on the perfect crystallite and in turn lower the T_{cp} and $T_{m,}$ as a consequence. However, the heterogeneous nucleation would accelerate the deposition of polymer molecules and in turn increase the T_{cp} and T_m. It should be noted that, while with a lower T_{cp} for a polymer based materials during solidification, the T_m during subsequent heating would be lower in consequence. This is because the crystalline spherulites formed at

a lower temperature tend to be smaller and possess more defects, leading to a lower T_m in subsequent heating. It follows that the trends for T_{cp} and T_m tend to be parallel.

As show in Fig. 3.43, the T_{cp} temperatures of the nanocomposites are found to be all lower than that of the neat PEEK. Overall, the role of decreased molecular mobility seems to be more dominant. It is expected that the nanoparticles in the PEEK matrix could more or less hinder the motion of the polymer chain segments, and in turn impart the smaller and more defects spherulites to the resulting nanocomposite, as compared with the homogeneous crystallization of pristine PEEK. As shown in Figs. 3.43(b), the 0.8 vol% alumina filled PEEK nanocomposite reveals the lowest T_{cp}. It appears that a very small amount (0.8 vol%) of nanoparticles would result in the greatest reduction in polymer chain mobility and thus in the greatest lowering in T_{cp}. With increasing nanoparticle amount, the heterogeneous nucleation effect would gradually evolve, providing more sites for nucleation and accelerating the deposition of polymer molecules; both in turn increasing T_{cp}. Hence, as shown in Fig. 3.43, the T_{cp} temperatures for all the nanocomposites would again shift to higher temperatures as the filler contents increase. However, even at 10 wt% or ~5 vol%, the T_{cp} temperatures for all the nanocomposites are still slightly lower than that of the pure PEEK.

Another factor affecting the T_{cp} of the nanocomposite could be the thermal conductivity of the inorganic fillers. This factor has not been carefully considered before. The thermal conductivities of the PEEK, silica, and alumina at room temperature are reported to be 0.2, 1, and 30 $Wm^{-1}K^{-1}$, respectively [59]. It is obvious that the thermal conductivities of the ceramic fillers are higher than that of the PEEK polymer, and in turn the thermal conductivity of the PEEK polymer would be enhanced when the inorganic filler was incorporated. With the higher thermal conductivity for the PEEK based nanocomposites, the temperature of the

PEEK polymer could reach the set temperature earlier during DSC cooling. Accordingly, the PEEK nanocomposite would crystallize at a higher crystallization temperature when the filler contents are sufficiently high. That could also be one of the reasons why T_{cp} of the nanocomposites show increasing trend with increasing nanoparticle content. This might also the reason that the alumina-filled PEEK composite, even with a lowest T_{cp} at 0.8 vol%, exhibits greater increasing tendency in T_{cp} at higher filler contents.

Therefore, the joint effects from the lowering of the PEEK molecule mobility, the enhancement of heterogeneous nucleation at higher filler contents, and the increases in thermal conductivities of the nanocomposites might be concurrently responsible for the lower extremas in T_{cp} at the filler content of 2.5 wt%, as shown in Fig. 3.43.

As expected, the addition of inorganic filler could result in more defects in crystallites when the nanoparticle-filled PEEK underwent crystallization during cooling stage, and the crystallization defects would lower the melting temperature T_m of the resulting PEEK nanocomposite. In addition, the spherulites in smaller size or of more defects could be molten at lower melting temperature T_m, as compared with the homogeneous crystallization in the neat PEEK. On the other hand, the nanoparticles would offer the sites for heterogeneous nucleation [139]. Hence, the higher nanoparticle content might impart the higher T_{cp}, T_m, and a higher degree of crystallinity to the resulting nanocomposites when the filler content increases. However, as shown in Tables 3.7 to 3.9 and Figs. 3.43 to 3.44, as the filler content increases, there is a decreasing trend for both T_{cp} and T_m, as compared with those of the neat PEEK, due to mainly the hindrance in molecular mobility. The heterogeneous nucleation effect was shadowed somewhat. It is well known that the polymer molecules could rearrange and re-crystallize at the heating stage. Hence, the maximum decrements for the T_m of the PEEK nanocomposites (in Fig. 3.44, about -8^{o}C) would be

smaller than those of the T_{cp} (in Fig. 3.43, about -30^{o}C).

In literature, it was proposed [164] that the inclusion of nano-sized zinc oxide filler (2 wt% in amount and 40 nm in size) into the isotactic polypropylene would increase the T_{cp} by about 3^{o}C and the heat of crystallization. This crystallization study [164] was conducted isothermally. It was concluded that the enhancement in T_{cp} could be attributed to the increase in specific surface area provided by zinc oxide nanoparticles, where the polymer chain segments would deposit on and crystallize.

Nevertheless, in the sense of non-isothermal crystallization, Kim et al. [139] suggested that the inclusion of the nano-sized silica into the poly(ethylene 2,6-naphthalate), PEN, would lower the T_{cp} by about 4 to 9^{o}C as the filler content increases from 0.3 to 0.9 wt% at a cooling rate of 10 ^{o}C/min. However, the T_m was found to only slightly increase by 0.5 to 0.9^{o}C. The increase in filler content would lower the T_{cp} of the PEN nanocomposite. As expected, the decrease in T_{cp} might be attributed to the less mobility of the PEEK chain segments when the nano-sized silica was introduced. The current study appears to follow along the line of this paper, with the effect in lowering polymer mobility being stronger than the heterogeneous nucleation effect.

It is possible to investigate the effects of cooling rate and filler content (wt% or vol% in Table 2.1) on the overall crystallization time, t_c, of the nanoparticles filled PEEK polymer, as shown in Figs. 3.45 and 3.46, respectively. The overall crystallization time can be defined as follows [139]:

$$t_c = \frac{\left|T_{ci} - T_{cf}\right|}{R_c}, \tag{3.6}$$

where R_c is cooling rate. As shown in Fig. 3.45, as expected, the increase in cooling rate would significantly lower the overall crystallization for both the pristine PEEK and the nanoparticles filled PEEK composites. At the same cooling rate, it is shown that the smaller size of 15 nm silica nanoparticles would contribute the more crystallization time to the PEEK polymer, as compared with that of the 30 nm silica, when the filler contents were increased from nil to 10 wt%, Fig. 3.46(a). The same trend could be also seen in Fig. 3.46(b), which the filler content is expressed in terms of volume fraction.

From the DSC curves, the absolute crystallinity fraction X_c at different cooling rates can be estimated by relating to the heat of fusion of an infinitely thick PEEK crystal, ΔH_f^o, as [162],

$$X_c = \frac{\Delta H_c}{\Delta H_f^o W_{polymer}} \times 100 , \tag{3.7}$$

where ΔH_f^o is ~130 J/g [163] and $W_{polymer}$ is the weight fraction of polymer matrix. As shown in Tables 3.7 to 3.9 and Fig. 3.47, it is obvious that a slower cooling rate would result in a slightly higher crystallinity value, as a result of more sufficient time for crystallization. Furthermore, the inclusion of nanoparticles, irrespective of silica or alumina, would result in slightly lower crystallinity fractions of the resulting PEEK composites on the basis of same cooling rate, as compared with the pristine PEEK. However, irrespective of the silica or the alumina filled into the PEEK polymer, the resulting nanocomposites with a nanoparticle content of 5 wt% show an extrema in crystallinity: the maximum X_c values for the prestine PEEK, silica-filled PEEK (15 and 30 nm SiO_2), and alumina-filled PEEK (30 nm Al_2O_3) at a cooling rate of 2.5^{o}C are 39.1, 39.6, 39.3, and 39.8, respectively. As a result, the inclusion of nanoparticles is found no significant enhancement on the crystalllinity of the resulting nanocomposite. On the contrary, the inclusion of nanoparticles into PEEK matrix could more

or less lower the crystallinity of the resulting PEEK nanocomposite at low cooling rates. The more the content of the nanoparticles in PEEK, the lower the crystallinity of the PEEK segments would be, as shown in Tables 3.7 to 3.9 and Fig. 3.48.

As stated early, the filler in polymer matrix do affect the molecular mobility when the molecules start to crystallize. As a consequence, the crystallinity of the polymer would decrease with the filler content up to the contents level of 2-5 wt%, as shown in Fig. 3.48(a). The same trend could be also found in Fig. 3.48(b) when the filler content is presented in terms of volume fraction. It seems that the smaller nanoparticles would result in a higher crystallinity.

The DSC results, coupled with the XRD patterns, suggest that there has been minimum chemical interaction between the PEEK polymer and ceramic nanoparticles occurred at the forming temperature of 400^{o}C. But the crystallization temperature and of the crystallinity fraction X_c of the PEEK matrix would be affected by the amount of nanoparticles, with the melting temperature T_m of PEEK matrix unchanged.

3.2.7 TGA measurements

It has been proposed that a polymer resin reinforced with nano-sized inorganic particulates would improve its thermal stability, including the resistances of thermal degradation and flammability. Therefore, it is desired to estimate the resistance of thermal degradation of the current PEEK composites. Figure 3.49 shows the TGA results. It can be seen that with increasing nanoparticle content, the degradation temperature T_D of the PEEK polymer continuously increases. With a silica content of 10 wt%, T_D can be raised by nearly

40^{o}C. It is considered to be an a reasonable improvement of the thermal stability.

Chapter 4 Discussions

4.1 Rule of mixtures on the Mg/CF/PEEK laminated composites

4.1.1 ROM on room temperature tensile properties

Theoretical predictions for the elastic modulus were done according to the well-known ROM [59].

$$E_L = V_f E_f + (1 - V_f) E_m \quad , \tag{4.1}$$

and

$$E_T = \frac{E_f E_m}{E_f (1 - V_f) + E_m V_f} \quad , \tag{4.2}$$

where E_L and E_T are the modulus for the longitudinal and transverse directions, V_f the fiber volume fraction, E_f and E_m the fiber and matrix modulus. These equations were first applied to calculate the theoretical modulus and strength for the APC-2 pregreg. The values for the Mg/APC-2 can be simply evaluated by Eq. (4.1) using their corresponding data.

As for the tensile strength, another set of equations were used [59] for the strength of the APC-2 prepreg.

$$\sigma_L = V_f \sigma_f + (1 - V_f) \sigma_m \, , \tag{4.3}$$

and

$$\sigma_T = \sigma_m (1 - 2\sqrt{\frac{V_f}{\pi}}) \quad . \tag{4.4}$$

The final strength for combining the Mg and APC-2 was simply calculated by Eq. (4.3).

From Table 4.1, it can be seen that both the measured stiffness and strength of the laminated composite are very close to the calculated values. Basically, the agreement between the experimentally obtained and theoretically predicted values (based on ROM) is

above 90%. Longitudinally, the measured values for UTS and stiffness of the laminated composite show 92 and 90% of the ROM values. It should be noted that the composite fails at a much lower tensile elongation (3-5%) than that typically for the AZ31 Mg alloy (15-25%). Thus the matrix Mg never reaches its full UTS value σ_m of 320 MPa. By using a lower flow stress σ'_m for the AZ31 Mg at the failure strain, namely around 250-280 MPa, in the modified ROM equation,

$$\sigma_L = V_f\sigma_f + (1 - V_f)\sigma'_m, \tag{4.5}$$

the theoretical prediction would be even closer to the experimental data. In other words, the measured UTS values actually approach to nearly 100% of the ROM prediction. On the other hand, those values along the transverse direction are all 100% based on the ROM theory. It indirectly suggests that there exists a sufficiently strong interface bonding between Mg and APC-2 prepreg. The load transfer was efficient across the interface.

In comparison with other metallic alloys, such as Mg, Al, Ti, and steel, the current Mg based laminated composite also exhibited much higher specific modulus and tensile strength in the longitudinal direction, as compiled in Table 4.2. In general, the specific properties of the current Mg based composite along its longitudinal direction are around double or triple of those for the metallic alloys.

Finally, it should be noted that the high tensile strength of 932 MPa for the Mg base composite is also much higher than the 'ultrahigh strength' of 610 MPa for the newly developed Mg-Zn-Y alloys [165].

4.1.2 Comparison with previous results on ARALL and CARALL

Previous efforts have resulted in promising aluminum base laminated composites [166-168], such as the aramid fiber-reinforced aluminum laminates (ARALL) and carbon fiber-reinforced aluminum laminates (CARALL). The aluminum matrix used was typically the high strength aircraft-used 2024-T3 Al, with a density of 2.77 g/cm^3 and tensile modulus, YS, UTS and elongation of 71 GPa, 355 MPa, 445 MPa, and 12%, respectively [169], and the polymer matrix of the prepreg is epoxy. Table 4.3 compares the current results on AZ31Mg/CF/PEEK with previously reported data on 2024Al/AF(CF)/epoxy [167,168,170], with similar fiber volume fractions.

It can be seen that the current Mg base laminate composite possesses the lowest density, but the highest longitudinal tensile strength. The longitudinal specific modulus and specific strength of Mg/CF/PEEK are both much higher than those of the aluminum counterparts. Nevertheless, due to the Mg matrix alloy used in this study is the relatively lower strength AZ31 Mg alloy, with a lower tensile modulus, YS, and UTS of 45 GPa, 220 MPa, and 290 MPa (much lower than those of 2024 Al), the transverse properties of Mg/CF/PEEK are slightly inferior to those of ARALL and CARALL. Since the transverse properties are basically determined by the matrix material, it is postulated that improvement can be made with the replacement of AZ31 by other higher strength Mg base alloys.

4.2 The effect of temperature on UTS of Mg/CF/PEEK laminated composites

In view of the effect of temperature on AZ31 magnesium alloy, it was reported that the UTS of AZ31, grain size 2.5-5.0 μm, at room temperature and 150^{o}C are 290 and 150 MPa, respectively, under a strain rate of 4x10^{-4} s^{-1} MPa [154]. Accordingly, the UTS of AZ31 alloy at 100^{o}C could be estimated to be 230 MPa, as shown in Table 4.4. The UTS decrements of AZ31 alloy at 100^{o}C and 150^{o}C, based on the UTS at room temperature, are 20.7% and

48.3%, respectively. And the decrement percentage for PEEK resin at 100°C and 150°C are 14.1% and 50%, respectively. As shown in Table 4.5, the decrements on the Mg/CF/PEEK laminated composites at 100°C and 150°C along the longitudinal direction are only 2.4% and 5.9%, respectively. Obviously, the UTS decrement in the Mg base laminated composite are much lower than that of the pristine Mg alloy when the temperature is up to 150°C, suggesting that the load transfer from the Mg matrix to the carbon fibers through interface is effective and sufficient. The continuous carbon fibers would not degrade their strength up to ~500°C.

It is well known that the glass transition temperature (T_g) of PEEK is 143°C. Accordingly, it is supposed that the performance of the physical entanglement occurred between the PEEK segments will become mobile and easier to carry out a viscous flow when the loading temperature exceeds the T_g of PEEK. Moreover, it is believed that the higher the loading temperature the more heat energy will be obtained by the PEEK segments, and the segments would basically behave themselves in a more ductile manner when the loading temperature is over T_g. As shown in Table 4.5, the UTS of the laminated composites will decrease as the testing temperature increases. Nevertheless, there was no drastic drop in strength at 150°C, slightly above T_g. The longitudinal specimens show a decrement of -5.9% at 150°C, while the transverse specimens reveal -23.4%. The very minor decrement for the longitudinal specimens directly reflects the fact that the major load was carried mostly by the strong carbon fibers (24% in volume fraction), as well as the Mg layer which occupies 61% in volume fraction. The smaller amount (15% in volume fraction) of the PEEK polymer seems to play a minor role when the loading temperature is slightly above the PEEK T_g temperature. As for the transverse specimens, the -23.4% degradation at 150°C is mainly a reflection of the loss of Mg strength.

In parallel, the increase in failure elongation of the laminated is also found to be minor when the testing temperature overpasses the T_g of the chain segments. It might be expected that the failure elongation of the composite should undergo a significant change as the testing temperature exceeding the T_g of the chain segments. It seems obvious that the physical entanglement of PEEK segments was not strongly responsible for the failure strain behavior of the laminated composites.

In view of the effect of temperature on the decrement of the UTS along the longitudinal direction, it is assured that the degradation of the Mg/CF/PEEK laminated composites at 100 and 150^{o}C would be much lower than that observed for the Mg alloy and PEEK resin. The addition of continuous carbon fibers appreciably raises the service temperature.

4.3 Comparison on the flexural properties of the Mg/CF/PEEK laminated composites with those of the CF/PEEK composites

It is interesting to compare the flexural properties of the Mg base laminated composites with the carbon fiber reinforced PEEK (CF/PEEK) composites in order to estimate the performance of the Mg/CF/PEEK laminated composites on the flexural load. As shown in Table 4.6, the flexural moduli of CF/PEEK along the longitudinal and transverse directions were reported to be 128 and 10.5 GPa, respectively [155]. However, those values on the Mg/CF/PEEK laminated composites are 61.8 and 36.5 GPa, respectively. The flexural modulus on the CF/PEEK composite along the longitudinal direction is twice of that of the Mg/CF/PEEK laminated composite. On account of the flexural stress values along the longitudinal direction between the CF/PEEK and the Mg/CF/PEEK, the CF/PEEK is about 1.8 times of that of the Mg/CF/PEEK. Obviously, the carbon fibers play the predominant and important role, enduring the most flexural load along the longitudinal direction. On the other

hand, the flexural modulus and stress on the Mg/CF/PEEK laminated along the transverse direction are 36.5 GPa and 318 MPa, respectively, as compared with those values of 10.5 GPa and 165 MPa, respectively, on the CF/PEEK composite. Accordingly, the Mg alloy should be the predominant when the flexural load acts transversely. In view of the anisotropic behaviors of the CF/PEEK and Mg/CF/PEEK composites, it is found that the ratio of the flexural modulus and stress along the longitudinal and transverse directions are 1.7 and 3.0, respectively, for the Mg/CF/PEEK composites, but they are 12 and 10.6, respectively, for the CF/PEEK composites, as shown in Table 4.6. It seems that the insertion of the base Mg alloy would significantly reduce the anisotropic effect of the carbon fibers.

It is well known that the fractured behavior of the hybrid composite on the flexural load is more complex than on the tensile load. As expected, there is shear stress prevailed on the interfacial layers. So, it is difficult to make a sufficient correlation between the flexural and tensile load on the hybrid composites. However, it is possible to estimate the performance of the reinforcement on the hybrid composite subjected to a tensile or flexural load. As a result, referring to Tables 4.1 and 4.6, the increments of Mg/CF/PEEK laminated composites on the tensile modulus and stress along the longitudinal direction, compared with the base Mg alloy, are 166 and 320%, respectively. And the increments on the flexural modulus and stress are 137 and 330%, respectively. It is apparent that the reinforcing effects of the carbon fibers on the tensile and flexural properties behave similarly.

4.4 ROM on the micro-hardness, Young's modulus, and UTS predications of the PEEK/nano-particle

Since there is no widely accepted addition rule for the nanocomposite hardness (or modulus and strength), it is simply evaluated by the modified rule of mixtures for

discontinuous reinforcement [59], as described in Eq. 4.6. i.e.,

$$X_c = \eta X_p V_p + X_m V_m, \tag{4.6}$$

where X can be hardness, modulus, or tensile strength, V is the volume fraction, and c, p, and m represent the composite, particle, and matrix. The strengthening efficiency coefficient η would decrease rapidly with decreasing reinforcement aspect ratio [59]. The maximum predicted composite modulus E_c would be ~4.1 for the 10 wt% (4.9 vol%) SiO_2 filled composite and ~5.0 for the 10 wt% (3.3 vol%) Al_2O_3 filled composites, using the modulus data of 3.9, 73, and 393 GPa [171] for PEEK, SiO_2, and Al_2O_3. The experimentally obtained data are again somewhat higher than the predicted ones (Table 4.7). Theoretically, the modulus for the Al_2O_3 filled composites should be higher, but the experimental data did not reveal such a trend. The predicted strength values in Table 4.7, based on Eqn. (4.6), are ~92 for the 10 wt% (4.9 vol%) SiO_2 filled composite and ~93 for the 10 wt% (3.3 vol%) Al_2O_3 filled composites, using the strength data of 89, 1500, and 2000 MPa [171] for PEEK, SiO_2, and Al_2O_3.

Extending the values for short fibers with aspect ratios of 10-100 to the range for nanoparticles with an aspect ratio of ~1, η is assumed to be ~0.1. With the best estimations for the Vicker microhardness H_v for the PEEK, SiO_2, and Al_2O_3 to be 21.7, 1000, and 1500, the maximum H_v readings would be 25.5 for the 10 wt% (4.9 vol%) SiO_2 filled composite and 25.9 for the 10 wt% (3.3 vol%) Al_2O_3 filled composites. The experimentally measured H_v data of 28.2-32.5 are slightly higher than such predicted values, but the variation trend is consistent. The comparisons between the theoretical and experimental microhardness data on various nanocompoistes, as well as the increment percentage with respect to the unfilled PEEK, are also presented in Table 4.7.

4.5 The tribology characteristics of the PEEK composites filled with nanoparticles

It has been claimed [54] that the wear resistance of PEEK composites filled with larger ZrO_2 nanoparticles measuring 86 nm became worse than that of the unfilled PEEK because of the discontinuous thick transfer film and the weak mutual adhesion. In contrast, the addition of much finer ZrO_2 measuring 10 nm could form a thin, uniform and tenacious transfer film on the counterpart steel surface during the wearing process, leading to a lower frictional coefficient and wear rate of the filled PEEK. It seems that the smaller fillers are more effective in increasing the hardness and lowering the wear rate, as also observed or expected in the current 15 nm SiO_2 composites. For the present PEEK composites containing both 15 and 30 nm nano particles and both exhibiting appreciable hardness increment, it is conceivable to expect satisfactory wear improvement in composites filled with 7.5 to 10 wt% nanoparticles.

4.6 The effect of inorganic nano fillers on the tensile properties of PEEK

As shown in Fig. 3.26(a), the elastic modulus of the nanoparticles filled PEEK composites would increase linearly with the content of the filler, but the UTS would not. It was reported that the elastic modulus of the resulting composites, no matter what the matrix and the filler were, would enhance linearly with the content of the inorganic fillers [129]. In the present study, the same trend in the improvement of modulus is also found.

Improving the performance of polymer products by incorporating inorganic fillers has long been an important industrial activity, and traditionally this has been achieved by using materials such as carbon blacks, clays, talc and silica. More recently, the modification of polymer composites using nano-scaled fillers, with their high surface to volume ratios, has

been of increasing interest. It is meaningful to examine the reasoning for the linear improvement in elastic modulus. The following reports provide some insights.

In an extensive study, Tsagaropoulos and Eisenberg [159,160] reported that a range of vinyl polymers exhibit an additional maximum in tanδ about 50^{o}C above the main a relaxation occurring at the glass transition T_g; and similar behavior has been observed also for poly (dimethylsiloxane) [172]. This additional relaxation was described by Tsagaropoulos and Eisenberg as a 'second glass transition' and the model they proposed to account for its presence, envisaged three regions around a nanoparticle; an inner tightly bound layer in which polymer motion is severely restricted by interactions with the surface, an intermediate but more loosely bound layer, and finally the unrestricted bulk polymer. Such a 3-layer model is supported by the NMR data [173], however neutron scattering experiments show only two relaxation times in filled systems [174,175]: a slow process, corresponding presumably to restricted mobility adjacent to the filler surface, and that of the bulk polymer which retains normal segmental dynamics.

According to the proposed model above, polymer reinforced with inorganic fillers would become more rigid close to the interface of the fillers. Accordingly, the resulting polymer nanocomposites would possess higher modulus when the fillers are incorporated. Te mean distance L between the statistically distributed nanoparticles can be roughly estimated by the equation [176],

$$L = d[(F/V_f) - 1] \quad , \tag{4.7}$$

where F is packing factor, 0.64 for mondispersed sphere, and V_f is volume fraction. Applying

the data in Table 2.1 and the above equation, it is possible to estimate the mean distance L between statistically distributed nanoparticles, as shown in Table 4.8. According to Table 4.8, the mean distance between statistically distributed nanoparticles for the 15 nm silica is apparently less than those of the 30 nm silica and 30 nm alumina. However, as shown in Fig. 3.26, the silica (15 nm) filled PEEK composites possess lower modulus and higher failure strain than those of silica (30 nm) and alumina (30 nm).

The value of the modulus associated with the composites filled with 15 nm silica is thought at first to be higher than those of the other two counterparts. But, a reverse effect is observed. Recalling the model proposed by Tsagaropoulos and Eisenberg, the thickness of the immobilized layer existing adjacent to the filler surface was estimated to be about 1.5 nm for silica-filled poly(dimethylsiloxane) [175] , and to be ~5 nm for polybutadiene [177]. Therefore, the main factors attributing the reverse effect in 15 nm silica might be:

1. The thickness of the immobilized layer is too minor, as compared with the large spacing between the nanoparticles, to play its role into effect.
2. The smaller the nanoparticles the easer to form agglomeration could be, and this effect could detrimentally and significantly lower the contribution of inter-filler distance.
3. The agglomeration in silica (15 nm) might be locally occurred; hence, the failure strains in silica (15 nm) filled PEEK composites are still higher than those of the other two.

In summary, the current volume fraction of the nanoparticles (less than 5 vol%) might still be too low to justify the above argument, since the interspacing between the nanopartilces is appreciably greater than the particle size. Thus the hardening effect from the thin interface mantle layer around the nanoparticles might be overshadowed by the clustering artifact.

4.7 The effect of inorganic fillers on the crystallization of PEEK molecular chains

As mentioned above, the particle content level at 5 wt% would show a local extrema in crystallinity, and this phenomenon could account for the UTS extrema for the filler contents around 5.0 to 7.5 wt%. As the particle contents are further raised to 7.5 or 10.0 wt%, the X_c values will decrease again to the range of 25 to 30%. It is supposed that the dispersion of the nano-size particles in the PEEK matrix by means of compression molding would result in more or less aggregation in micrometer size. In the interface between PEEK and nanoparticle, a "melt-induced diffusion" phenomenon might occur, and this phenomenon could force the nanoparticles to diffuse into the PEEK matrix, as shown in the TEM images in Figs. 3.28-3.31. The TEM micrographs show that both the isolated nanoparticles and clustering of 5-9 nanoparticles could exist in the PEEK matrix simultaneously. On the other hand, due to the large size difference in the PEEK powders (~100 μm) and the nanoparticles (15 or 30 nm) used in the hot pressing fabrication, there are only partial nanoparticles diffusing into the center of the PEEK powders during melting; the remaining nanoparticles would still be retained in the surrounding area around the micro-sized PEEK powder during melting. It follows that not all nanoparticles could contribute their effects in enhancing heterogeneous nucleation during crystallization, especially for the case with high nanoparticle contents.

The crystallinity was found to be 39% for the pure PEEK at a cooling rate of 2.5 ^{o}C/min, as shown in Tables 3.7 to 3.9. However, irrespective of the content of particles, the kind of particles, or the size of the particles under investigation, the crystallinities of silica or alumina filled PEEK nanocomposites were found to have the X_c values ranging from 34-40% at the cooling rate of 2.5 ^{o}C/min. It was reported [139] that a small amount (0.3-0.9 wt%) of 7 nm silica could increase the crystallinities from 22% for the pristine PEN (poly(ethylene 2,6-naphthalate) to about 37% for the 0.9 wt% silica filled PEN composite. There is a

significant effect on the promotion of crystallinity of the polymer matrix according to the above-mentioned study [139]. However, in the present study on the PEEK polymer with 2.5-10 wt% silica or alumina, this effect was not seen. This might be partly related to the much higher level of particle content used in the current study. It is supposed that the higher the particle content in the polymer matrix, the less the mobility of the polymer chain segments would be. And the less mobility in polymer chain segments could, more or less, hinder the growth of the polymer spherulites. Another factor is the fact that the maximum crystallinity fraction of the PEEK polymer can only be 48% [178], and the crystallinity of the pure PEEK used in this study is already 39%. The increment by adding nanoparticles might be very limited.

As shown in Tables 3.7 to 3.9 and Fig. 3.45, the inclusion of nanoparticles could lower the required time for crystallization of PEEK segments. The time required for crystallization on PEEK segments at a cooling rate of 2.5 ^{o}C/min is 11.2 minutes; and it is only 5-8 minutes for the silica or alumina filled PEEK composites at the same cooling rate. It is obvious that the heterogeneous nucleation prevailed when the nanoparticles are introduced. Meanwhile, at high cooling rates (15-30 ^{o}C/min), the crystallization time will show no significant difference between pristine and the nanoparticle-filled PEEK segments. It seems the effect attributed by heterogeneous nucleation would be gradually diminished when the cooling rate is faster than the magnitude of the required crystallization time.

As shown in Table 4.8, a polymer filled with finer particles would result in smaller spacing between particles, and in turn the smaller spacing that would hinder the growth of the PEEK crystallites. It follows that a lower crystallinity of PEEK polymer is expected. However, in comparing the X_c values for composites filled with the same amount of SiO_2 nano particles but with different sizes of 15 and 30 nm, the finer particles would lead to a

slightly higher crystallinity, as shown in Tables 3.7 to 3.9. Also referring to Fig. 3.46, the PEEK polymer filled with finer filler, silica 15 nm, appears to require longer crystallization time to the PEEK segments. This effect seems to contradict the above argument. Nevertheless, it should be born in mind the small the particle would also provide a larger specific surface area in which the PEEK molecules could deposit and crystallize, in the sense of heterogeneous nucleation. The nearly spherical surface of silica, as shown in TEM images, Fig. 2.2, could be the favorable sites for crystallization. As a result, the PEEK segments should have more time to crystallize, as expected.

As for the effect from the volume fraction, the 30 nm alumina composites would possess a lower volume fraction than the other two, resulting in larger spatial distances, as shown in Table 4.8. Moreover, the irregular surface of alumina, as shown in Fig. 2.2, would result in more sites for polymer molecules to deposit and crystallize. Consequently, the PEEK polymer filled with 30 nm alumina nanoparticles would bring about higher crystallinity, as shown in Fig. 3.47, as compared with that of the 30 nm silica.

4.8 Closing remarks

Through the extensive studies on the fabrications of the Mg/CF/PEEK laminated composites and the nanoparticulate filled PEEK composites, there are a number of new findings. Firstly, on the fabrication of the Mg/CF/PEEK laminated composites, it reveals that the fabrication by means of sandwiching the APC-2 prepregs and the Mg sheets could offer an effective and easy-to-process route to design the carbon fiber reinforced Mg laminates, as compared with that fabricated by the liquid metal infiltration Mg laminates. The successfully fabricated Mg/CF/PEEK laminated composites can reach near 100% ROM values for tension or bending. Moreover, the laminated composites can sustain their tensile strength up to

150^{o}C.

Secondly, on the fabrication of the nanoparticules filled PEEK composites, it is proved that the incorporation of the silica or alumina nanoparticles can improve the elastic modulus, UTS, and H_v values of the resulting PEEK nanocomposites by 20-50%, with the sacrifice of tensile elongation. Moreover, the dispersion of the nanoparticles in the PEEK matrix reveals reasonable dispersion, and there is no apparent interaction between the nanoparticle and the PEEK matrix. The PEEK nanocomposites with filler contents ranging from 2.5 to 10 wt% show minor variation in T_m, which ranges between 332 and 340^{o}C. And the larger variation of T_c was found to range from 295 to 260^{o}C. It is also shown that the overall crystallization time, t_c, and the crystallinity, X_c, would be decreased as the filler incorporated.

Chapter 5 Conclusions

5.1 Conclusions on Mg/CF/PEEK laminated composites

1. For better bonding between Mg and APC-2 prepreg, proper surface treatments, including roughening and special etching, of the AZ31 Mg alloy are necessary.

2. The resulting Mg/CF/PEEK laminated composite can effectively enhance the tensile stiffness and strength of AZ31 Mg alloy to nearly 100% ROM values.

3. With the addition of 39 vol% APC-2 prepreg, the Mg/CF/PEEK laminated composite can triple the UTS of AZ31 Mg alloy to as high as 932 MPa.

4. Based on SEM examinations, the interfacial bonding between APC-2 and Mg alloy is satisfactory. As a result, the tensile load transfer can be prevailed by means of shear stress occurring on the interface.

5. The final failure of the composite under longitudinal loading is due to the failure of carbon fibers; while that under transverse loading is due to the Mg fracture.

6. The current Mg base laminated composite possesses much higher longitudinal specific modulus and strength than metallic Mg, Al, Ti alloys and steel, as well as other Al base laminated composites such as ARALL and CARALL.

7. The Mg/CF/PEEK Mg based laminated composites were successfully fabricated through a simple hot pressing method. This promising method can fabricate high performances and

low density laminated composites in terms of tensile as well as flexural properties.

8. The flexural modulus, stress and strain along the longitudinal and transverse directions of the Mg based laminated composite are 61.8 GPa, 960 MPa and 0.03; and 36.5 GPa, 318 MPa and 0.07, respectively. The current laminated composite shows sufficiently high resistance to bending deflection.

9. Multiple fracture modes are observed in the longitudinal flexural specimen, while a more simple behavior is seen in transverse counterpart.

10. The peel strength of the Mg/APC-2/Mg laminate is superior to that of the epoxy-resin-adhered Al/CFRP laminated composites.

11. Tensile testing at elevated temperatures of 100 and 150^{o}C, lower and slightly higher than the Tg temperature of the PEEK polymer revealed that the tensile strength of the Mg/CF/PEEK laminated composite can sustain its high level with at most 6% degradation along the longitudinal direction.

12. Pretreatment of the Mg sheets with or without CrO_3 etching shows significant differences in terms of the resulting interfacial bonding between Mg and APC-2.

13. The physically intermolecular entanglements may be responsible for the satisfactory interface bonding.

5.2 Conclusions on PEEK composites reinforced by nano-sized SiO_2 and Al_2O_3 particulates

1. Irrespective of silica or alumina particles filled, the PEEK based nanocomposites can improve their hardness, elastic modulus, and tensile strength by 20-50%, with the sacrifice of tensile elongation. The maximum increment percentages with respect to the unfilled PEEK are 50%, 36%, and 21% for hardness, elastic modulus, and UTS, respectively.

2. The optimum strengthening improvement occurs in composites filled with 5.0-7.5 wt% (or 2-4 vol%) nanoparticles. With a greater amount to 10 wt%, the clustering problem would start to lower the tensile strength, but still continuously upgrade the hardness and elastic modulus. In terms of wear applications, a higher nanoparticle content is desired.

3. Theoretically, the harder nanopartilces with a spherical shape would lead to more uniform spatial dispersion and more efficient strengthening. Extrafine nanoparticles measuring around 15 nm seem to elaborate a lower strengthening efficiency in stiffness than the 30 nm ones, but providing a more uniform spatial distribution and a lower loss of the ductility.

4. The modified rule of mixtures originally for short-fiber reinforced composites can provide a rough strengthening trend for the nanocomposites, but the predicted values are typically lower than the measured data.

5. With no surface modification on the silica or alumina nanoparticles, the dispersion of these nanoparticles in the PEEK matrix reveals reasonably good dispersion.

6. With further improvement of nanoparticle clustering via proper nanoparticle surface modifications, the mechanical properties are expected to be more pronouncedly upgraded.
7. There is no apparent interaction occurred between the nanoparticles and the PEEK matrix

during the hot pressing at 400^{o}C, based on the XRD and DSC results.

8. The inclusion of silica or alumina nanoparticles to limited amounts will lower both the T_{cp} and T_m of the resulting PEEK nanocomposites, and slightly decrease in the degree of crystallinity, as compared with the pure PEEK polymer. The inclusion of silica or alumina nanoparticles can also significantly decrease the crystallization time.

9. The inclusion of the inorganic filler into PEEK matrix can improve the thermal stability of the resulting nanocomposites by 40^{o}C.

References

1. I. J. Polmear, Light Alloys 3rd ed., Edward Arnold, London (1995) 17.
2. G. V. Raynor, The Physical Metallurgy of Magnesium and Its Alloys, Pergamon Press, London, (1957) 1.
3. K. G. Kgeider, ed., Composite Materials, **Vol. 4**, L. Broutman and R. Krock, eds., Metal-Matrix Composites, Academic Press, Inc., New York, 1974.
4. Y. Kojima, Materials Science Forum, **350-351** (2000) 3.
5. I. J. Polmear, Materials Science and Technology, **10** (1994) 1.
6. I. J. Polmear, Materials Transactions, JIM, **37** (1996) 12.
7. S. Kamado and Y. Kojima, Materia Japan, **38** (1999) 285.
8. H. Watanabe, T. Mukai, M. Kohzu, S. Tanabe, and K. Higashi, Materials Transactions. JIM, **40** (1999) 809.
9. H. Watanabe, T. Mukai, and K. Higashi, Scripta Materialia, **40** (1999) 209.
10. H. Watanabe, T. Mukai, M. Mabuchi and K. Higashi, Scripta Materialia, **41** (1999) 209.
11. H. Somekawa, M. Kohzu, S. Tanabe, and K. Higashi, Materials Science Forum, **350-351** (2001) 177.
12. M. Mabuchi, T. Asahina, H. Iwasaki, and K. Higashi, Materials Science and Technology, **13** (1997) 825.
13. K. Kubota, M. Mabuchi, and H. Higashi, Journal of Materials Science, **34** (1999) 2255.
14. M. Mabuchi, K. Ameyama, H. Iwasaki, and K. Higashi, Acta Materialia, **47** (1999) 2047.
15. H. HaferKamp, M. Niemeyer, R. Boehm, U. Holzkamp, C. Jashik, and V. Kaese, Materials Science Forum, **350-351** (2000) 31.
16. M. Gupta. L. Lu, M. O. Lai, and H. H. Lee, Materials Research Bulletin, **34** (1999) 1201.

17. W. C. Harrigan Jr., Materials Science and Engineering, **A244** (1998) 75.

18. D. J. Towle and C. M. Friend, Materials Science and Technology, **9** (1993) 35.

19. S. Lim and T. Choh, Journal of Japan Light Metals, **42** (1992) 772

20. H. Watanabe, T. Mukai, T. G. Nieh, and K. Higashi, Scripta Materialia, **42** (2000) 249.

21. J. M. Wu, and Z. Z. Li, J. Alloys Compound, **2999** (2000) 9.

22. G. J. Fan, M. X. Quan, Z. Q. Hu, J. Echert, and L. Schultz, Scripta Materialia, **41** (1999) 1147.

23. S. Hwang and C. Nishimura, Scripta Materialia, **44** (2001) 2457.

24. T. Mukai, H. Watanabe, and K. Higashi, Materials Science Forum, **350-351** (2000) 159.

25. H. Watanabe, H. Tsutsui, T. Mukai, K. Ishikawa, Y. Okanda, M. Kohzu, and K. Higashi, Materials Science Forum, **350-351** (2000) 171.

26. T. Mukai, M. Yamanoi, H. Watanabe, and K. Higashi, Scripta Materialia, **45** (2001) 89.

27. M. Mabuchi, K. Kubota, and K. Higashi, Mater. Trans., JIM, **36** (1995) 1249.

28. M. Mabuchi, H. Iwasaki, K. Yanase, and K. Higashi, Scripta Materialia, **36** (1997) 681.

29. T. Mohri, M. Mabuchi, H. Iwasaki, T. Aizawa, and K. Higashi, Materials Science and Engineering, **A290** (2000) 139.

30. W. Bleck, JOM, **48 (7)** (1996) 26.

31. G. Marron and P. Teracher, JOM, **48 (7)** (1996) 16.

32. A. A. Lou, JOM, **54 (2)** (2002) 42.

33. W. H. Bonner, U. S. Patent 3065205, 1962.

34. T. E. Attwood, P. C. Dawson, J. L. Freeman, L. R. J. Hoy, J. B. Rose, and P. A. Staniland, Polymer, **22** (1981) 1096.

35. P. C. Dwason and D. J. Blundell, Polymer, **21** (1980) 577.

36. M. T. Bishop, F. E. Karasz, P. S. Russo, and K. H. Langley, Macromolecules, **18** (1985) 86.

37. C. Bailly, D. J. Williams, and F. E. Krantz, W. T. Macknight, Polymer, **28** (1987) 1009.

38. S. L. Gao and J. K. Kim, Composites, **31A** (2000) 517.

39. D. J. Kemmish and J. H. Hay, Polymer, **26** (1985) 905.

40. G. Mensitieri, D. Nobile, A. Apicella, and L. Nicolais, Polymer Engineering and Science, **29** (1959) 1786.

41. G. Mensiteri, A. Apialla, J. M. Kenny, and L. Nicolais, J. Applied Polymer Scince, **37** (1989) 381.

42. P. Cebe, S. Y. Chung, and S.D. Hong, J. Applied Polymer Science, **33** (1987) 487.

43. M. F. Sonnenschein, J. Applied Polymer Science, **72** (1999) 175.

44. M. F. Sonnenschein, J. Applied Polymer Science, **74** (1999) 1146.

45. O. Petillo, G. Peluso, L. Ambrosio, L. Nicolais, W. J. Kao, and J. M. Anderson, J. Biomedical Materials Research, **28** (1994) 635.

46. C. Morrison, R. Macnair, C. Macdonald, A. Wykman, I. Goldie, and M. H. Grant Biomaterials, **16** (13) (1995) 987.

47. J. L. Dewez, A. Doren, Y. J. Schneider. R. Legras, and P. Rouxhelt, in Interface in New Materials, Elsevier Applied Science, London, (1991) 84.

48. W. S. Ramsey, W. Hertl, E. D. Nowlan, and N. J. Binkowshi, In Vitro, **20** (1984) 802.

49. I. S. Ertel, B. D. Ratner, and T. A. Horbelt, J. Biomedical Materials Research, **24** (1990) 1637.

50. C. Henneuse, B. Goret, and M. B. Jecqueline, Polymer, **39** (4) (1998) 835.

51. C. Henneuse, B. Goret, and M. B. Jecqueline, Polymer, **39** (22) (1998) 1998.

52. M. B. Jacqueline, G. Pantano, and O. Noiset, Polymer, **38** (6) (1997) 1387.

53. M. C. Wijers, M. Jin, M. Wessling, and H. Strathmann, Journal of Membrane Science, **147** (1998) 117.

54. Q. H. Wang, J. f. Xu, W. Shen, and W. Liu, Wear, 196 (1996) 82.

55. Q. H. Wang, Q. Xue, H. Liu, W. Shen, and J. Xu, Wear, 198 (1996) 216.

56. Q. H. Wang, J. F. Xu, W. Shen, and Q. Xue, Wear, **209** (1997) 316.

57. C. Fujimoto, M. Sakurai, and Y. Muranaka, Journal of Microsolumn Separations, **11** (10) (1999) 693.

58. S. Ramakrishna, J. Mayer, E. Wintermantel, and K. W. Leong, Composites Science and Technology, **61** (2001) 1189.

59. D. Hull and T. W. Clyne, An Introduction to Composite Materials, 2nd Edition, Cambridge, 1996.

60. S. Hashemi, A. J. Kinloch, and J. G. Williams, J. Composite Materials, **24** (1990) 918.

61. W. J. Mikols, J. C. Seferis, A. Apicella, and L. Nicolais, Polymer Composites, **3** (1982) 118.

62. A. Apicella, L. Nicolais, and C. Cataldis, Advances in Polymer Science, **66** (1985) 189.

63. A. Apicella, L. Nicolais, and G. Astarita, Polymer, **20** (1979) 1143.

64. H. Shen and G. S. Springer, J. Composite Materials, **11** (1977) 2.

65. R. Bunsell, Long-Term Degradation of Polymer-Matrix Composites, Loncise Encyclopedia of Composite Materials. 2nd ed., Pergamon, New York, 1994.

66. F. N. Cogswell, Thermoplastic Aromatic Polymer Composites, Butterworth-Heienmann, Boston, 1992.

67. C. Ageorges, L. Ye, and M. Hou, Composite, **32A** (2001) 839.

68. A Lustiger, F. S. Uralil, and G. M. Newaz, Polymer Composites, **11** (1990) 65.

69. S. Saiello, J, Kenny, and L. Nicoais, J. Materials Science, **25** (1990) 3493.

70. M. Zhang, J. Xu, Z. Zhang, H. Zeng, and X. Xiong, Polymer, **37** (1996) 5151.

71. Y. L. Zou and A. N. Netravali, J. Adhesion Science and Technology, **9** (1995) 1505.

72. H. Kobayashi, E. Hayakawa, T. Kikutani, and A. Takaku, Advanced Composite Materials, **1** (1991) 155.

73. M. J. Folkes, G. Kalay, and A. Ankara, Composites Science and Technology, **46** (1993) 77.

74. Y. Lee and R. S. Porter, Polymer Engineering and Science, **26** (1986) 633.

75. S. L. Gao and J. K. Kim, Composites, **32A** (2001) 763.

76. S. L. Gao and J. K. Kim, Composites, **32A** (2001) 775.

77. V. Mallik, Composites, **32A** (2001) 1167.

78. S. Ramakrishna, J. Mayer, E. Wintermantel, and K. W. Levng, Composites Science and Technology, **61** (2001) 1189.

79. C. Morrison, R. Macanair, C. MacDonald, A. Wyleman, I. Goldie, and M. H. Grant, Biomaterials, **16** (1995) 987.

80. S. A. Brown, R. X. Hastings. J. J. Mason, and A. Moet, Biomaterials, **11** (1990) 541.

81. D. F. Williams, A. McNamara, and R. M. Turner, J. Materials Science Letters, **6** (1987) 188.

82. W. J. Cantwell, G. Broster, and P. Davies, J. Reinforced Plastics and Composites, **15** (1996) 1161.

83. V. K. Srivastava and P. J. Hogg, J. Materials Science, **33** (1998) 1129.

84. V. K. Srivastava and P. J. Hogg, J. Materials Science, **33** (1998) 1119.

85. K. Tanaka and S. Kawakami, Wear, **79** (1982) 221.

86. B. J. Briscoe, A. K. Pogosian, and D. Tabor, Wear, **27** (1974) 19.

87. B. R. Burroughs, J. H. Kim, and T. A. Blanchet, Tribology Transactions, **42** (1999) 592.

88. K. H. Rao, K. S. E. Forssberg, and W. Forsling, Colloids and Surfaces A; Physicochemical and Engineering Aspects, **133** (1998) 107.

89. J. Luo, J. J. Lannutti, and R. R. Seghi, Dental Materials, **14** (1998) 29.

90. D. W. Sundastorm and Y. D. Lee, J. Applied Polymer Science, **16** (1972) 3159.

91. J. T. Mottram, Materials Design, **13** (1992) 221.

92. D. M. Bigg, Composite, **10** (1979) 95.

93. T. Suzuki, K. Adachi, and T. Kotaka, Polymer Journal, **13** (1981) 385.

94. U. Xin, G. Xu, P. G. Hofstra, and R. C. Bajcar, Journal of Polymer Science: Part B: Polymer Physics, **36** (1998) 2259.

95. J. E. Strangroom, Physics in Technology, **14** (1983) 290.

96. A. F. Sprecher, J. D. Carlson, and H. Conard, Materials Science and Engineering, **95** (1987) 187.

97. H. Block and J. P. Kelly, J. Physica, **D 21** (1988) 1661.

98. N. I. Garmayunov and V. A. Murtsovkin, J. Engineering Physics, **43** (1982) 963.

99. S. Fraden, A. J. Hurd, and R. B. Meyer, Physical Review Letters, **63** (1989) 2373.

100. C. Park and R. E. Robertson, Journal of Materials Science, **33** (1998) 3541.

101. S. Schwarzer and A. Roosen, Journal of European Ceramic Society, **19** (1999) 1007.

102. C. W. Nan, J. Applied Physics, **76** (1994) 1155.

103. M. S. Ardi, W. Dick, and D. H. McQueen, Plastics, Rubber and Composites Processing and Applications, **24** (1995) 157.

104. M. Sumita, Y. TsuKumo, K. Miyasaka, and K. Ishikawa, J. Materials Science, **18** (1983) 1758.

105. S. N. Maiti and K. K. Sharma, J. Materials Science, **27** (1992) 4605.

106. Z. Bartczak, A. S. Argogon, R. E. Cohen, and M. Weinberg, Polymer, **40** (1999) 2347.

107. S. Bazhenov, J. X. Li, A. Hiltner, and E. Baer, J. Applied Polymer Science, **52** (1994) 243.

108. I. L. DubniKova, V. G. Oshmyan, and A. Ya. Gorenberg, J. Materials Science, **32** (1997) 1613.

109. J. Jancar, J. Polymer Engineering Science, **30** (1990) 707.

110. J. Jancar and A. T. Dibenedetto, J. Materials Science, **29** (1994) 4651.

111. E. Fekete, S. Z. Molnar, G. M. Kim, G. H. Michler, and B. Pukanszky, J. Macromolecular Science. B, Physics, 13 (1999) 885.

112. G. M. Kim and D. H. Lee, J. Applied Polymer Science, **82** (2001) 785.

113. S. Iijima, Nature, **354** (1991) 56.

114. E. T. Thostenson, Z. Ren, and T. W. Chou, Composites Science and Technology, **61**

(2001) 1899.

115. P. M. Ajayan, O. Stephan, C. Colliex, and D. Trauth, Science, **265** (1994) 1212.

116. A. Malliars and D. Turner, J. Applied Physics, **42** (1917) 614.

117. M. Narkis, A. Ram, and F. Flashner, J. Applied Polymer Science, **22** (1978) 1163.

118. B. Poulaert and J. Jossi, Polymer, **24** (1983) 841.

119. C. Klason and J. Kubat, J. Polymer Materials, **11** (1985) 47.

120. S. Radlhakrishnan, J. Materials Science Letters, **6** (1987) 145.

121. S. Balabanov and Krezhov, J. Physics. D: Appled Physics, **32** (1999) 2573.

122. M. T. Connor, S. Roy, and T. A. Ezquerra, Physical Review B, **57** (1998) 2286.

123. R. P. Pant, V. K. Sankaranarayanan, V. N. Ojha, D. K. Suri, Journal of Magnetism and Magnetic Materials, **201** (1999) 27.

124. S. Wizel, S. Margel, and A. Gedanken, J. Materials Research, **14** (1999) 3913.

125. K. S. Suslick, S. B. Choe, A. A. Cichowlas, and M. W. Grinstaff, Nature, **353** (1991) 414.

126. S. Wolff, Tire Technology, **15** (1987) 276.

127. P. Cassagnau and F. Melis, Polymer, **44** (2003) 6607.

128. M W. Lee, X. Hu, C. Y. Yue, L. Li, and K. C. Tam, Composites Science and Technology, **63** (2003) 339.

129. P. Musto, G.. Ragosta, G.. Scarinzi, and L. Mascia, Polymer, **45** (2004) 1697.

130. A. Kasseh, A. Ait-Kadi, B. Riedl, and J. F. Pierson, Polymer, **44** (2003) 1367.

131. V. A. Soloukin, W. Posthumus, J. C. M. Brokken-Zijp, J. Loos, and G. de With, Polymer, **43** (2002) 6169.

132. C. S. Tan, C. C. Juan, and T. W. Kuo, Polymer, **45** (2004) 1805.

133. C. C. Chang, K. H. Weu, Y. C. Chang, and W. C. Chen, J. Polym. Res., **10** (2003) 1.

134. W. C. Chen and L. H. Lee, Chemical Materials, **13** (2000) 3320.

135. W. C. Chen and S. J. Lee, Polymer J., **32** (2000) 67.

136. Y. Y. Yu, C. Y. Chen, and W. C. Chen, Polymer, **44** (2003) 593.

137. W. Weng, G. Chen, and D. Wu, Polymer, **44** (2003) 8119.

138. T. D. Fornes and D. R. Paul, Polymer, **44** (2003) 3945.

139. S. H. Kim, S. H. Ahn, and T. Hirai, Polymer, **44** (2003) 5625.

140. A. A. Baker, Materials Science and Engineering, **17** (1975) 177.

141. A. A. Baker, M. B. P. Allery, and S. J. Harris, J. Material Science, **4** (1969) 242.

142. P. W. Jackson, D. M. Braddick, and P. J. Walker, Fiber Science and Technology, **5** (1972) 219.

143. R. T. Pepper and E. G. Kendall, U. S. Patent No. 3,770,488, 1973.

144. R. T. Pepper, J. W. Upp, R. C. Rossi, and E. G. Kendall, Metallurgical Transactions, **2** (1971) 117.

145. G. Korb, J. Korab, and G. Groboth, Composites, **29A** (1998) 1563.

146. C. T. Lin and P. W. Kao, Acta Materialia, **44 (3)** (1996) 1181.

147. M. F. Amateau, J, Composite Materials, **10** (1976) 279.

148. D. M. Goddard, Metal Progress, **125** (1984) 49.

149. H. A. Katzman, J. Materials Science, **22** (1987) 144.

150. F. Wu, J. Zhu, K. Ibe, and T. Oikawa, Composites Science and Technology, **58** (1998) 77.

151. O. O. Popoola, R. C. McCune, and L. Reatherford, U. S. Patent, 5983495, 1999.

152. E. Kung, C. Mercer, S. Allameh, O. Popoola, and W. O. Soboytjo, Metallurgical and Materials Transcations, **32A** (2001) 1997.

153. S. S. Zumdahl, Chemical Principles, 4th ed. Houghton Mifflin Company, Boston, USA, (2002) 923.

154. H. L. Lin and J. C. Huang, Materials Transactions, **43 (10)** (2002) 2424.

155. G. T. Chuang, Processing-Morphology-Property Relationship of Poly (ether ether ketone) and Its Carbon Fiber Composite, Ph. D. Thesis, National Sun Yat-Sen University, ROC

(1995).

156. S. C. Chen and J. C. Huang, Materials Science and Technology, **13** (1997) 143.

157. K. Y. Rhee and J. H. Yang, Composites Science and Technology, **63** (2003) 33.

158. R. M. Silverstein and F. X. Webster, Spectrometric Identification of Organic Compounds (6^{th} ed.) John Wiley & Sons, Inc. NY, USA, (1998) 92.

159. G. Tsagaropoulos, A. Eisenberg, Macromolecules, **28** (1995) 396.

160. G. Tsagaropoulos, A. Eisenberg, Macromolecules, **28** (1995) 6067.

161. V. Arrighia, I. J. McEwena, H. Qiana, and M. B. Serrano Prietob, Polymer, **44** (2003) 6259.

162. J. Sandlera, P. Wernerb, M. S. P. Shaffera, V. Demchukc, V. Altstadt, and A. H. Windlea, Composites, **A 33** (2002) 1033.

163. C. L. Wei, M. Chen, and F. E. Yu, Polymer, **44** (2003) 8185.

164. J. Tang, Y. Wang, H. Liu, and L. A. Belfiore, Polymer, **45** (2004) 2081.

165. A. Inoue, Y. Kawamura, and J. Koike, J. Materials Research, **16** (2001) 1894.

166. L. B. Vogelesang, and J. W. Gunnink, Materials Design, **7(6)** (1986) 287.

167. C. T. Lin, P. W. Kao, and F. S. Yang, Composites, **22** (1991) 135.

168. C. T. Lin and P. W. Kao, Materials Science and Engineering, **A190** (1995) 65.

169. Aluminum Standards and Data, The Aluminum Association, Inc., Washington, D.C. USA, 1993.

170. R. J. Bucci. L. N. Mueller, L. B. Vogelesang, and J. W. Gunnink, Proc. 33^{rd} Intl. SAMPE Symp., **33** (1988) 1237.

171. W. D. Callister, Jr, Materais Sceience and Engineering, An Introduction (6^{th} ed). John Wiley & Sons, Inc. NY, USA, 2003.

172. A. Yim, R. S. Chahal, and L. E. St. Pierre, J. Colloid Interface Science, **28** (1973) 583.

173. V. M. Litvinov and H. W. Spiess, Makromol Chemistry, **192** (1991) 3005.

174. V. Arrighi, J. S. Higgins, A. N. Burgess, and G. Floudas, Polymer, **39** (1998) 6369.

175. S. Gagliardi, V. Arrighi, R. Feruson, and M. T. F. Telling, Physica B, **301** (2001) 110.

176. V. Arrighi, I. J. McEwena, H. Qiana, and M. B. Serrano Prieto, Polymer, **43** (2002) 6169.

177. S. Vieweg, R. Unger, E. Hempel, and E. Donth, J. Non-Crystal Solids, **235** (1998) 470.

178. J. M. Margolis, Engineering Thermoplastics, Marcel Dekker, Inc. NY, USA, 1985.

Table 1.1 Typical properties of metal matrices for metal-metal laminates [3].

Metal	Density, g/cm^3	T_m, ^oC	Heat capacity kJ/(kg·K)	Thermal cond., W/(m·K)	Thermal exp. coeff., $10^{-6}/^oC$	Tensile strength, MPa	Modulus, GPa	Remarks
Aluminum	2.8	580	0.96	171	23.4	310	70	6061 (T6)
Beryllium	1.9	1280	1.88	150	11.5	620	290	annealed
Copper	8.9	1080	0.38	391	17.6	340	120	oxygen-free hardened
Lead	11.3	320	0.13	99	28.8	20	10	1% Sb
Magnesium	1.7	570	1.00	76	25.5	290	40	AZ31B-H24
Nickel	8.9	1440	0.46	62	13.3	760	210	nichel 200 hardened
Niobium	8.6	2470	0.25	55	6.8	280	100	
Steel	7.8	1460	0.46	29	13.3	2070	210	ultra-high strength (MOD.H-11)
Superalloy	8.3	1390	0.42	19	16.7	1100	210	Inconel X-750
Tantalum	16.6	2990	0.17	55	6.5	410	190	
Tin	7.2	230	0.21	43	23.4	10	40	
Titanium	4.4	1650	0.59	7	9.5	1170	110	Ti-6Al-4V
Tungsten	19.4	3410	0.13	168	4.5	1520	410	
Zinc	6.6	390	0.42	112	27.4	280	70	alloy Agada

Table 1.2 Comparison of mechanical and physical properties of various materials [32]

Material	Cast Mg		Wrought Mg		Cast Iron	Steel	Cast Al		Wrought Al		Plastics (PC/ABS)
Alloy/Grade	AZ91	AM50	AZ80 -T5	AZ31 -H24	Class 40	Galvanized	380	A356 -T6	6061 -T6	5182 -T6	Dow Pulse 2000
Process/ Product	die cast	die cast	extrusion	sheet	sand cast	sheet	die cast	P/M cast	extrusion	sheet	injection molding
Density (d, g/cm^3)	1.81	1.77	1.80	1.77	7.15	7.80	2.68	2.76	2.70	2.70	1.13
Elastic Modulus (E, GPa)	45	45	45	45	100	210	71	72	69	70	2.3
Yeild Strength (YS, MPa)	160	125	275	220	N/A	200	159	186	275	235	53
Ultimate Tensile Strength (UTS, MPa)	240	210	380	290	293	320	324	262	310	310	55
Elongation (e_f, %)	3	10	7	15	0	40	3	5	12	8	5 at yield and 125 at break
Fatigue Strength (S_f, MPa)	85	85	-	-	128	-	138	90	95	-	-
Thermal Cond. (l, W/m·K)	51	65	78	77	41	46	96	159	167	123	-
Thermal Exp. Coeff. (d, mm/m·K)	26	26	26	26	10.5	11.70	22	21.5	23.6	24.1	74
Melting Temp. (T_m, ^oC)	598	620	210	230	1175	1515	595	615	652	638	143

Table 1.3 Values for the lattice spacing constants of the annealed isotropic samples and other parameters of chain comformations [35]

Lattice Constants	PEEK	Poly(phenylene oxide)	Poly(phenylene sulphide)
$a(A^o)$	7.75	8.07	8.67
$b(A^o)$	5.86	5.54	5.61
$c(A^o)$	10.0	9.72	10.26
Crystal density (g/cm^3)	1.40	1.41	1.43
amorphous density ($g/c\ m^3$)	1.26	1.27	1.32
Main chain	125	124	110
Bond angle			
T_g (^oC)	144	85	92
Crystal melting point T_m (^oC)	335	285	295

Table 1.4 Properties of PEEK and 'Victrex' polyethersulphone [34]

Property	Test method	PEEK	Poly(ethersulphone)
T_m, ^oC		>330	-
T_g, ^oC		145	225
Heat distortion temp., ^oC at 1.81 MPa	ASTM D648	160	203
Continuous service temp., ^oC		200	180
Tensile yield strength, MPa	ASTM D638	91	84
Elongation at break, %	ASTM D638	150 max	40-80
Environemntal stress cracking in:	ICI test[a]		
Acetone		Good	Poor
Trichloroethylene		Good	Fair/good
Ethyl acetate		Good	Poor
Isopropyl alcohol		Good	Good
n-hexane		Good	Good

Note: (a) The environemntal stress cracking of the tabulated polymers in various solvents is issued by ICI Group.

Table 1.5 Solubility of PEEK at 25 ^{o}C [36]

Sovlent	Solubility
94.9% H_2SO_4	complete
89.9% H_2SO_4	nearly complete
84.8% H_2SO_4	partial
79.6% H_2SO_4	negligible
CH_3SO_3H	complete
CF_3CO_2H	negligible
Poly(phosphoric acid) (100^{o}C)	slight/partial

Table 1.6 Typical values for specific strength and specific stiffness of different materials along the longitudinal (or fiber reinforced) direction [77]

Material	Strength/density ($MPa/g/cm^3$)	Stiffness/density ($MPa/g/cm^3$)
Steel	250	27000
Aluminum alloys	200	26000
Titanium alloys	200	25000
AS-4/PEEK (TPC)[a]	1400	84000
IM6/epoxy (TSC)	2200	128000

Note: (a) TPC represents thermal-plastic composite, and TSC represents thermal-set composite.

Table 1.7 Selected properties for different types of matrix [59]

Matrix	Density ρ ($g\ cm^{-3}$)	Young's modulus *E* (GPa)	Possion's ratio ν	Tensile strength *σ* (GPa)	Failure strain ε (%)	Thermal expansion coefficient α ($10^{-6}\ K^{-1}$)	Thermal conductivity K ($W\ m^{-1}\ K^{-1}$)
Thermosets							
Epoxy resins	1.1-1.4	3-6	0.38-0.40	0.035-0.1	1-6	60	0.1
Polyesters	1.2-1.5	2.0-4.5	0.37-0.39	0.04-0.09	2	100-200	0.2
Thermoplastics							
Nylon 6.6	1.14	1.4-2.8	0.3	0.06-0.07	40-80	90	0.2
Polypropylene	0.90	1.0-1.4	0.3	0.02-0.04	300	110	0.2
PEEK	1.26-1.32	3.6	0.3	0.17	50	47	0.2
Metals							
Al	2.70	70	0.33	0.2-0.6	6-20	24	130-230
Mg	1.80	45	0.35	0.1-0.3	3-10	27	100
Ti	4.5	110	0.36	0.3-1.0	4-12	9	6-22
Ceramics							
Borosilicate glass	2.3	64	0.21	0.10	0.2	3	12
SiC	3.4	400	0.20	0.4	0.1	4	50
Al_2O_3	3.8	380	0.25	0.5	0.1	8	30

Table 1.8 Fibre properties [59]

Fibre	Density ρ ($g\ cm^{-3}$)	Young's modulus E (GPa)	Possion's ratio ν	Tensile strength σ (GPa)	Failure strain ε (%)	Thermal expansivity α ($10^{-6}\ K^{-1}$)	Thermal conductivity K ($W\ m^{-1}\ K^{-1}$)
SiC monofilament	3.0	400	0.20	2.4	0.6	4.0	10
Boron monofilament	2.6	400	0.20	4.0	1.0	5.0	38
HM[a] carbon	1.95	Axial 380	0.20	2.4	0.6	Axial –0.7	Axial 105
HS[b] carbon	1.75	Axial 230	0.20	3.4	1.1	Axial –0.4	Axial 40
E-glass	2.56	76	0.22	2.0	2.6	4.9	13
Kevlar™ 49	1.45	Axial 130	0.35	3.0	2.3	Axial –6	Axial 0.04
Saffil™	3.4	300	0.26	2.0	0.7	7.0	5
SiC whisker	3.2	450	0.17	5.5	1.2	4.0	100
Cellulose (flax)	1.0	80	0.3	2.0	3.0	-	-

Note: (a) high modulus, (b) high strength

Table 2.1 Comparison of the weight and volume percentage (wt% and vol%) of the nano SiO_2 and Al_2O_3 particles added in the PEEK composites. The densities for PEEK, SiO_2, and Al_2O_3 are 1.30, 2.65, and 3.98 g/cm^3, respectively.

SiO_2	wt %	2.5	5.0	7.5	10.0
	vol %	1.2	2.5	3.7	4.9
Al_2O_3	wt %	2.5	5.0	7.5	10.0
	vol %	0.8	1.6	2.5	3.3

Table 3.1 Processing conditions of Mg/APC-2 laminated composites

Sample No.	Carbon fiber configuration	No. of plies	Etching agent	Temp. (^{o}C)	Pressure (MPa)
1	Unidirectional	4	CrO_3/HNO_3	400	1.1
2	Unidirectional	4	CrO_3/HNO_3	400	0.7
3	Unidirectional	4	CrO_3/HNO_3	400	0.7
4	Unidirectional	4	CrO_3/HNO_3	400	1.6
5	Unidirectional	3	CrO_3/HNO_3	400	1.0
6	Unidirectional	2	CrO_3/HNO_3	400	0.7
7	Unidirectional	3	CrO_3/HNO_3	400	1.4

Table 3.2 The room temperature mechanical properties along the longitudinal (L) and transverse (T) directions. The volume fractions of AZ31, carbon fiber, and PEEK in the resulting Mg/CF/PEEK composite are 61%, 24%, and 15% in volume, respectively. The UTS tolerance is less than 3%.

Property	AZ31 Mg	CF (L)	PEEK	CF/PEEK (L)	CF/PEEK (T)	Mg/CF/PEEK (L)	Mg/CF/PEEK (T)
Density *d* (g/cm^3)	1.77	1.77	1.30	1.60	1.60	1.70	1.70
Stiffness *E* (GPa)	45	230	3.6	134	8.9	74.6	30.8
YS (MPa)	220	--	91	--	--	225	125
UTS (MPa)	290[a]	3400[b]	170[c]	2130	80	932	188
Specific stiffness *E/d* ($GPa/g/cm^3$)	25.4	129.9	2.8	83.8	5.6	43.9	18.1
Specific strength *UTS/d* ($MPa/g/cm^3$)	164	1921	131	1331	50	548	111
Elongation (%)	15	1.1	50	1.5	1.3	1.9	2.6

a: Referring to reference 3.

b: Referring to reference 59.

c: Referring to reference 59.

Table 3.3 UTS and elongation data obtained at room temperature (25°C), 100°C, and 150°C along the longitudinal and transverse directions. The UTS tolerance is less than 3%.

Property	25°C		100°C		150°C	
	(L)	(T)	(L)	(T)	(L)	(T)
UTS (MPa)	932	188	910	163	877	144
Elongation (%)	1.9	2.6	1.2	2.7	1.1	3.3
UTS decrement percentage (%)[a]	-	-	-2.4	-9.1	-5.9	-23.4

a: UTS decrement is based on the room temperature tensile tests.

Table 3.4 The wavenumbers of the characteristic group absorptions on the AS-4 prepreg, etched CF-phase, unetched CF-phase, and etched Mg-phase.

Sample	Absorption wavenumber, cm^{-1}														
AS-4 prepreg	1651	1596	1489	1413	1308	1278	1222	1186	1155	1101	1012	926	840	767	681
Etched CF-phase	1650	1595	1490	1413	1307	1279	1223	1188	1157	1101	1012	928	839	767	679
Unetched CF-phase	1649	1595	1490	1414	1306	1279	1223	1188	1157	1101	1012	928	839	767	678
Etched Mg-phase	1649	1595	1490	1414	1308	1279	1223	1188	1157	1101	1012	928	838	768	677

Table 3.5 Characteristic group absorption wave-numbers of the PEEK polymer.

Wave-number, cm^{-1}	Corresponding group absorption
1653	C=O stretching
1489, 1597 doublets	Benzene ring skeletal vibration
1223	C-O-C stretching
1160, 1186	Aromatic ketones stretching and bending
1000-1300	In-plane bending of the ring C-H bonds
675-900	Out-of-plane bending of the ring C-H bonds

Table 3.6 The microhardness and tensile data of the nanoparticle-filled PEEK composites. The increment percentage of the experimental data with respect to the unfilled PEEK is also included in parentheses (). The UTS tolerance is less than 3%.

Filler	Variable	0 wt%	2.5 wt%	5 wt%	7.5 wt%	10 wt%
SiO_2 15 nm	H_v	21.7	24.0 (11%)	27.5 (27%)	29.5 (36%)	32.5 (50%)
	E, GPa	3.9	4.1 (5%)	4.1 (5%)	4.3 (10%)	4.5 (15%)
	UTS, MPa	89	96 (8%)	100 (12%)	102 (15%)	101 (14%)
	Elongation %	12	10.43 (-13%)	8.55 (-29%)	7.37 (-39%)	6.06 (-50%)
SiO_2 30 nm	H_v	21.7	26.1 (20%)	28.1 (29%)	29.1 (34%)	30.0 (38%)
	E, GPa	3.9	4.2 (8%)	4.5 (15%)	4.9 (26%)	5.3 (36%)
	UTS, MPa	89	94 (6%)	105 (18%)	91 (2%)	89 (0%)
	Elongation %	12	6.58 (-45%)	5.95 (-50%)	4.77 (-60%)	3.89 (-68%)
Al_2O_3 30 nm	H_v	21.7	23.2 (7%)	25.0 (15%)	27.2 (25%)	28.2 (30%)
	E, GPa	3.9	4.1 (5%)	4.4 (13%)	4.6 (18%)	5.1 (31%)
	UTS, MPa	89	97 (9%)	105 (18%)	108 (21%)	94 (6%)
	Elongation %	12	4.45 (-63%)	4.04 (-66%)	3.70 (-69%)	3.48 (-71%)

Table 3.7 DSC data on the 15 nm silica filled PEEK composites, obtained from the cooling DSC runs. $T_{ci,}$ $T_{cp,}$ and T_{cf} are referred to the initiation, peak, and finishing temperatures for PEEK crystallization, respectively. t_c is referred to the overall crystallization time.

Sample	Cooling rate (°C/min)	T_m (°C)	T_{ci} (°C)	T_{cp} (°C)	T_{cf} (°C)	t_c (min)	$-H_c$ (J/g)	X_c (%)
Pure PEEK	2.5	--	311	300	283	11.20	50.77	39.1
	5	340	306	296	269	7.36	49.30	37.9
	10	340	302	290	276	2.60	45.89	35.3
	15	340	298	286	272	1.77	44.43	34.2
	20	340	296	282	268	1.37	43.34	33.3
	25	340	293	279	265	1.12	42.51	32.7
	30	340	291	276	262	0.96	41.80	32.2
SiO_2 2.5%	2.5	--	296	284	276	8.24	49.31	38.9
	5	332	293	279	266	5.34	47.15	37.2
	10	332	288	274	261	2.71	43.98	34.7
	15	333	285	271	257	1.83	43.22	34.1
	20	333	282	268	254	1.39	42.33	33.4
	25	334	281	267	253	1.11	41.70	32.9
	30	334	279	265	252	0.90	40.94	32.3
SiO_2 5.0%	2.5	--	302	296	284	7.08	48.91	39.6
	5	338	298	292	277	4.10	46.81	37.9
	10	338	293	286	275	1.81	43.72	35.4
	15	338	290	283	271	1.27	41.37	33.5
	20	338	288	280	268	1.01	40.63	32.9
	25	338	286	277	265	0.84	39.89	32.3
	30	338	284	275	263	0.73	39.15	31.7
SiO_2 7.5%	2.5	--	302	296	289	5.28	46.18	38.4
	5	338	300	292	284	3.22	44.97	37.4
	10	337	295	286	277	1.84	41.49	34.5
	15	337	292	283	272	1.36	39.80	33.1
	20	337	291	280	269	1.10	38.72	32.2
	25	337	289	277	266	0.92	37.88	31.5
	30	337	287	275	264	0.79	37.52	31.2
SiO_2 10%	2.5	--	303	294	286	6.52	41.89	35.8
	5	340	299	289	280	3.84	38.03	32.5
	10	340	294	282	273	2.14	35.10	30.0
	15	340	291	278	269	1.53	34.40	29.4
	20	340	289	276	266	1.17	33.93	29.0
	25	340	287	274	264	0.93	33.70	28.8
	30	340	285	272	262	0.76	33.46	28.6

Table 3.8 DSC data on the 30 nm silica filled PEEK composites, obtained from the cooling DSC runs. T_{ci}, T_{cp}, T_{cf} , are referred to the initiation, peak, and finishing temperatures for PEEK crystallization, respectively. t_c is referred to the overall crystallization time.

Sample	Cooling rate (°C/min)	T_m (°C)	T_{ci} (°C)	T_{cp} (°C)	T_{cf} (°C)	t_c (min)	$-H_c$ (J/g)	X_c (%)
Pure PEEK	2.5	--	311	300	283	11.20	50.77	39.1
	5.0	340	306	296	269	7.36	49.30	37.9
	10	340	302	290	276	2.60	45.89	35.3
	15	340	298	286	272	1.77	44.43	34.2
	20	340	296	282	268	1.37	43.34	33.3
	25	340	293	279	265	1.12	42.51	32.7
	30	340	291	276	262	0.96	41.80	32.2
SiO_2 2.5%	2.5	--	294	285	279	5.84	42.29	35.6
	5.0	335	289	279	272	3.34	38.17	32.1
	10	336	283	271	263	1.92	36.00	30.7
	15	336	279	267	258	1.41	34.26	28.9
	20	336	277	264	254	1.12	33.13	27.7
	25	336	275	262	252	0.94	32.43	26.7
	30	336	275	261	251	0.84	32.02	25.9
SiO_2 5.0%	2.5	--	296	288	276	7.76	48.52	39.3
	5.0	339	290	281	275	3.08	43.54	35.3
	10	339	284	274	266	1.74	41.41	33.5
	15	339	280	269	261	1.28	39.17	31.7
	20	339	277	266	256	1.04	37.87	30.1
	25	339	275	263	253	0.87	36.78	29.8
	30	339	274	261	251	0.77	36.03	29.2
SiO_2 7.5%	2.5	--	296	289	282	5.44	41.34	34.4
	5.0	341	291	282	275	3.10	36.75	30.6
	10	340	284	275	267	1.76	34.78	28.9
	15	340	281	270	261	1.27	32.93	27.4
	20	340	278	267	257	1.03	31.66	26.3
	25	340	275	264	254	0.86	30.86	25.7
	30	340	274	262	251	0.76	30.17	25.1
SiO_2 10%	2.5	--	298	291	281	7.08	41.64	33.3
	5.0	339	293	285	274	3.94	37.62	30.1
	10	338	288	278	265	2.27	36.00	28.4
	15	338	284	273	259	1.65	33.83	27.0
	20	338	281	270	255	1.29	32.36	26.1
	25	338	279	267	252	1.07	31.19	25.6
	30	338	277	265	250	0.90	30.25	25.3

Table 3.9 DSC data on the 30 nm alumina filled PEEK composites, obtained from the cooling DSC runs. T_{ci}, T_{cp}, and T_{cf} are referred to the initiation, peak, and finishing temperatures for PEEK crystallization, respectively. t_c is referred to the overall crystallization time.

Sample	Cooling rate (°C/min)	T_m (°C)	T_{ci} (°C)	T_{cp} (°C)	T_{cf} (°C)	t_c (min)	$-H_c$ (J/g)	X_c (%)
Pure PEEK	2.5	--	311	300	283	11.20	50.77	39.1
	5	340	306	296	269	7.36	49.30	37.9
	10	340	302	290	276	2.60	45.89	35.3
	15	340	298	286	272	1.77	44.43	34.2
	20	340	296	282	268	1.37	43.34	33.3
	25	340	293	279	265	1.12	42.51	32.7
	30	340	291	276	262	0.96	41.80	32.2
Al_2O_3 2.5%	2.5	--	280	271	263	7.12	50.49	39.0
	5	338	276	265	256	3.88	46.82	36.9
	10	338	270	259	248	2.20	42.71	33.7
	15	337	268	256	244	1.61	40.86	32.2
	20	337	268	254	240	1.31	39.83	31.4
	25	337	267	253	239	1.11	39.47	31.1
	30	337	266	254	239	0.96	40.00	31.6
Al_2O_3 5.0%	2.5	--	304	289	285	7.84	46.00	39.8
	5	338	296	287	271	5.02	44.02	37.2
	10	338	291	282	268	2.31	40.96	35.0
	15	338	289	280	266	1.51	39.63	33.6
	20	338	286	277	264	1.12	38.87	32.7
	25	337	285	275	262	0.94	37.83	32.0
	30	338	284	274	260	0.81	37.46	31.4
Al_2O_3 7.5%	2.5	--	302	293	282	8.08	45.00	37.4
	5	337	299	290	275	4.82	42.61	35.4
	10	337	294	285	274	2.04	41.34	34.4
	15	337	291	282	270	1.43	40.30	33.5
	20	337	289	279	265	1.21	39.39	32.8
	25	337	288	277	263	0.98	38.76	32.2
	30	337	286	276	262	0.83	38.35	31.9
Al_2O_3 10%	2.5	--	301	293	282	7.90	46.38	37.2
	5	336	298	289	274	4.82	43.49	34.6
	10	336	293	283	268	2.54	40.93	33.2
	15	336	290	279	264	1.75	39.28	32.1
	20	336	288	276	260	1.39	38.23	31.5
	25	336	285	273	256	1.18	37.48	30.6
	30	336	283	270	253	1.00	36.78	30.3

Table 4.1 Summary of the room temperature mechanical properties along the longitudinal (L) and transverse (T) directions. The volume fractions of AZ31, carbon fiber, and PEEK in the resulting Mg/CF/PEEK composite are 61%, 24%, and 15% in volume, respectively.

Property	AZ31 Mg Exp	CF (L) Exp	PEEK Exp	CF/PEEK (L) Theo	CF/PEEK (L) Exp	CF/PEEK (T) Theo	CF/PEEK (T) Exp	Mg/CF/PEEK (L) Theo	Mg/CF/PEEK (L) Exp	Mg/CF/PEEK (T) Theo	Mg/CF/PEEK (T) Exp
Density *d* (g/cm^3)	1.77	1.77	1.30	1.60		1.60		1.70		1.70	
Stiffness *E* (GPa)	45	230	3.6	142	134	9	8.9	82.8	74.6	31.0	30.8
YS (MPa)	220	3400	91	--		--		--	225	--	125
UTS (MPa)	290	3400	170	2140	2130	20	80	1018	932	185	188
Specific stiffness *E/d* (GPa/g/cm^3)	25.4	129.9	2.8	83.8		5.6		43.9		18.1	
Specific strength *UTS/d* (MPa/g/cm^3)	164	1921	131	1331		50		548		111	
Elongation (%)	15	1.1	50	1.5		1.3		1.9		2.6	

Exp: Experimental data, Theo: Theoretical data based on ROM.

Table 4.2 Comparison of the current Mg laminated composites with other commercial structural metallic alloys, such as AZ91 Mg, 6061 Al, Ti-6Al-4V and 1040 steel.

Property	Mg/CF/PEEK	Mg alloy (AZ91)	Al alloy (6061)	Ti alloy (Ti-6Al-4V)	Steel (1040)
d (g/cm^3)	1.70	1.77	2.70	4.20	7.80
E (GPa)	75	45	72	135	210
UTS (MPa)	932	290	350	1000	600
E/d (GPa/g/cm^3)	44	25	27	32	27
UTS/d (MPa/g/cm^3)	548	163	130	238	77

Table 4.3 Comparison of the room temperature tensile properties of the current Mg laminated composites along the longitudinal (L) and transverse (T) directions with previously reported data on the ARALL (2024Al/AF/epoxy) [170] and CARALL (2024Al/CF/epoxy) [167,168].

Property	Mg/CF/PEEK* (L)	Al/AF/epoxy ARALL (L)	Al/CF/epoxy CARALL (L)	Mg/CF/PEEK* (T)	Al/AF/epoxy ARALL (T)	Al/CF/epoxy CARALL (T)
d (g/cm^3)	1.70	2.29	2.35	1.70	2.29	2.35
E (GPa)	75	64	84	31	49	56
YS (MPa)	225	395	485	125	228	255
UTS (MPa)	932	717	750	188	317	285
Elongation (%)	1.9	2.5	1.4	2.6	12.7	9.4
E/d ($GPa/g/cm^3$)	44	28	36	18	21	24
UTS/d ($MPa/g/cm^3$)	548	313	319	111	138	121

* Present work.

Table 4.4 The yield stress (YS) and ultimate tensile strength (UTS) of the AZ31 alloy, PEEK polymer, and carbon fiber at room temperature (25^{o}C), 100^{o}C, and 150^{o}C [154, 178].

Temp. (^{o}C)	AZ31		PEEK		Carbon fiber	
	YS (MPa)	*UTS* (MPa)	*YS* (MPa)	*UTS* (MPa)	*YS* (MPa)	*UTS* (MPa)
25	220	290	91	170	3400	3400
100	175	230	78	146	3400	3400
150	110	150	46	85	3400	3400

Table 4.5 Comparison of the theoretical (based on ROM) and experimental UTS values on the Mg/CF/PEEK laminated composites along the longitudinal (L) and transverse (T) directions at room temperature, 100°C, and 150°C.

Property	25°C				100°C				150°C			
	(L)		(T)		(L)		(T)		(L)		(T)	
	Theo	Exp	Theo	Exp	Theo	Exp	Theo	Exp	Theo	Exp	Theo	Exp
UTS (MPa)	1018	932	185	188	978	910	147	163	920	877	95	144
Elongation (%)	--	1.9	--	3	--	1.2	--	2.7	--	1.1	--	3.3
UTS decrement percentage (%)[a]	--	--	--	--	--	-2.4	--	-13	--	-5.9	--	-23

a: UTS decrease is based on the room temperature values.

Table 4.6 Summary of the room temperature flexural properties along the longitudinal (L) and transverse (T) directions. The volume fractions of AZ31, carbon fiber, and PEEK in the resulting Mg/CF/PEEK composite are 61%, 24%, and 15% in volume, respectively [155].

Property	AZ31 Mg	CF (L)	PEEK	CF/PEEK (L)		CF/PEEK (T)		Mg/CF/PEEK (L)		Mg/CF/PEEK (T)	
	Exp	Exp	Exp	Theo	Exp	Theo	Exp	Theo	Exp	Theo	Exp
Flexural modulus (GPa)	--	--	--	--	128	--	10.5	--	61.8	--	36.5
Flexural stress (MPa)	--	--	--	--	1750	--	165	--	960	--	318

Exp: Experimental data, Theo: Theoretical data based on ROM.

Table 4.7 Comparison of the theoretically predicted (Theo) and experimentally measured (Exp) mechanical data. The increment percentage of the experimental data with respect to the unfilled PEEK is also included in parentheses ().

Filler	Variable	0 wt%		2.5 wt%		5 wt%		7.5 wt%		10 wt%	
		Theo	Exp	Theo	Exp	Theo	Exp	Theo	Exp	Theo	Exp
SiO_2 15 nm	H_v	--	21.7	22.6	24.0 (11%)	23.7	27.5 (27%)	24.6	29.5 (36%)	25.5	32.5 (50%)
	E (Gpa)	--	3.9	3.9	4.1 (5%)	4.0	4.1 (5%)	4.0	4.3 (10%)	4.1	4.5 (15%)
	UTS (MPa)	--	89	90	96 (8%)	91	100 (12%)	91	102 (15%)	92	101 (14%)
SiO_2 30 nm	H_v	--	21.7	22.6	26.1 (20%)	23.7	28.1 (29%)	24.6	29.1 (34%)	25.5	30.0 (38%)
	E (Gpa)	--	3.9	3.9	4.2 (8%)	4.0	4.5 (15%)	4.0	4.9 (26%)	4.1	5.3 (36%)
	UTS (MPa)	--	89	90	94 (6%)	91	105 (18%)	91	91 (2%)	92	89 (0%)
Al_2O_3 30 nm	H_v	--	21.7	22.7	23.2 (7%)	23.0	25.0 (15%)	23.7	27.2 (25%)	25.9	28.2 (30%)
	E (Gpa)	--	3.9	4.2	4.1 (5%)	45	4.4 (13%)	4.8	4.6 (18%)	5.0	5.1 (31%)
	UTS (MPa)	--	89	90	97 (9%)	91	105 (18%)	92	108 (21%)	93	94 (6%)

Table 4.8 The mean distance L between statistically distributed nanoparticles. $L = d[(F/V_f) - 1]$, d, F, and V_f are filler diameter, packing factor (0.64 for spherical fillers), and volume fraction, respectively [176].

Filler	Weight fraction (%)	Volume fraction (%)	Filler diameter (nm)	Filler spacing (nm)
SiO_2 (15 nm)	2.5	1.2	15	800
	5.0	2.5	15	369
	7.5	3.7	15	244
	10.0	4.9	15	81
SiO_2 (30 nm)	2.5	1.2	30	1570
	5.0	2.5	30	738
	7.5	3.7	30	489
	10.0	4.9	30	362
Al_2O_3 (30 nm)	2.5	0.8	30	2370
	5.0	1.6	30	1170
	7.5	2.5	30	768
	10.0	3.3	30	552

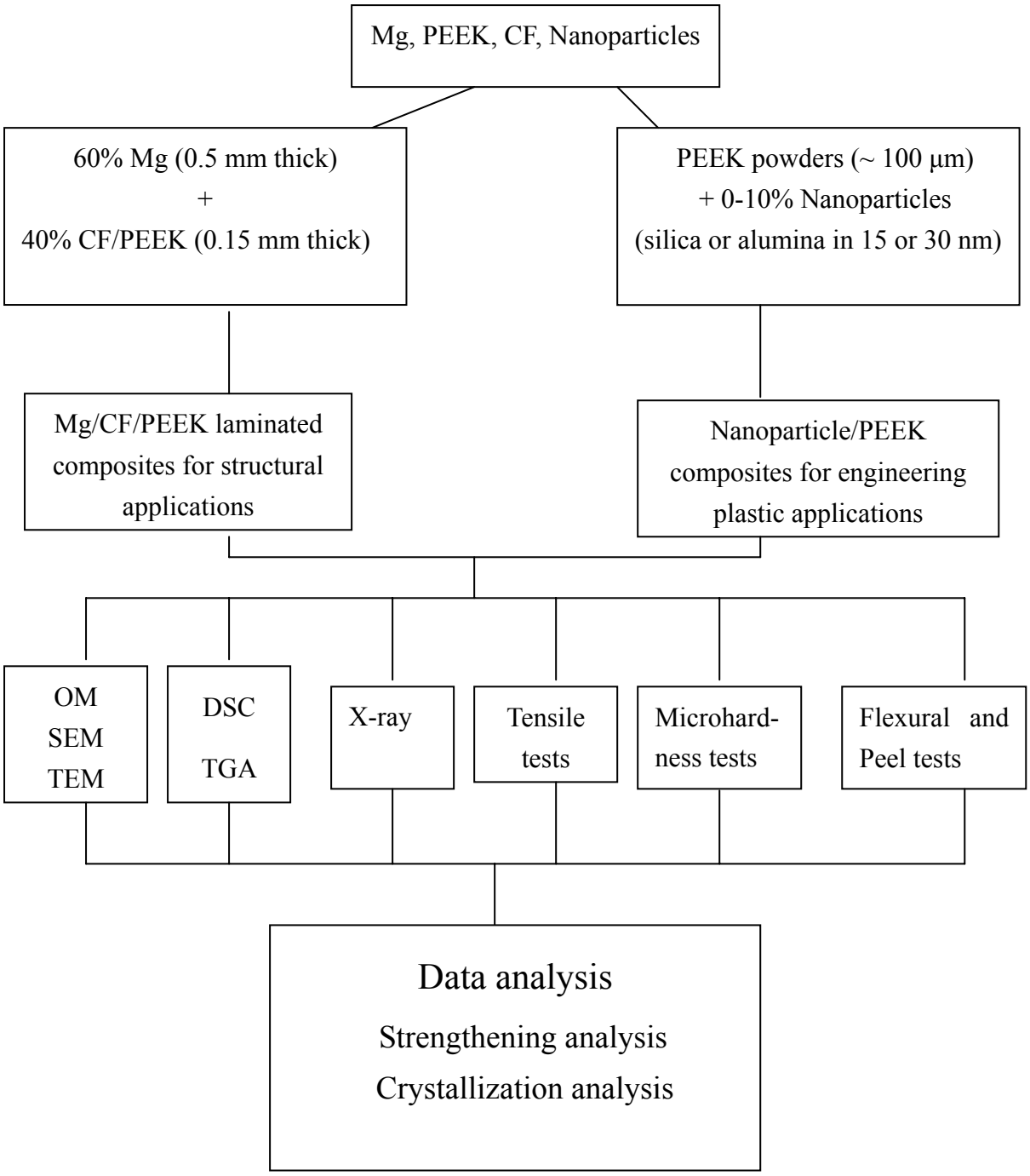

Fig. 1.1 Flow chart of the conducting research

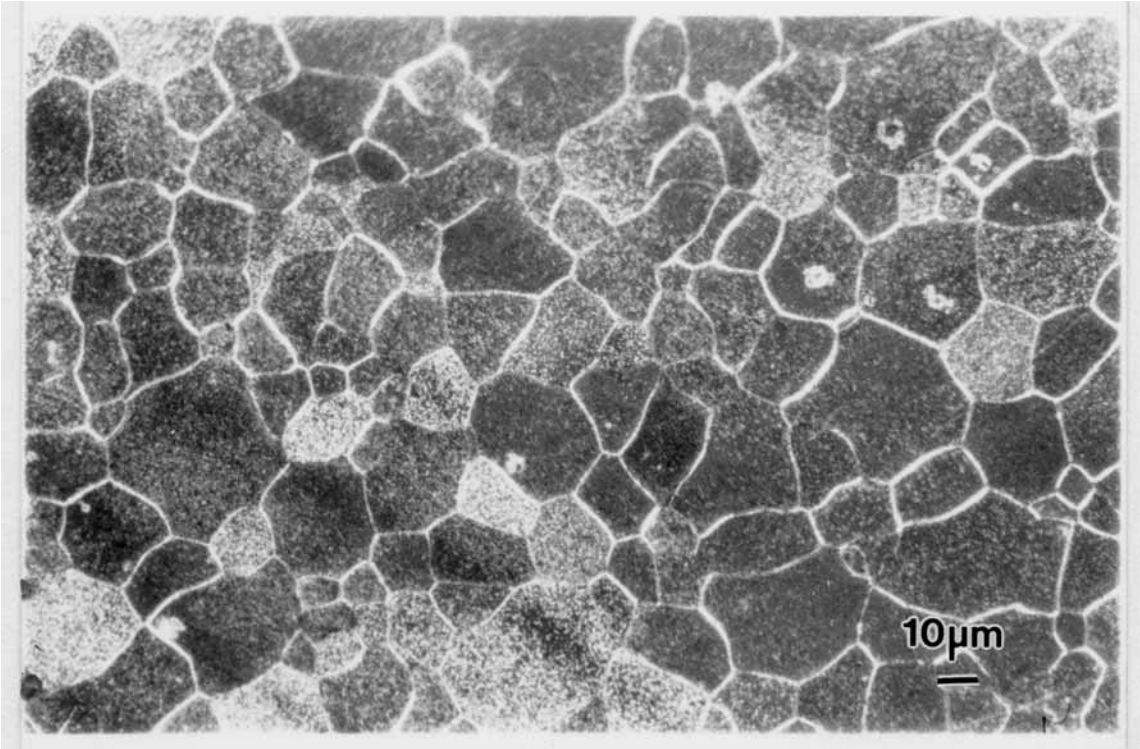

Fig. 2.1　Microstructure of the as-received AZ31 Mg alloy. The grain size is about 34 μm in average.

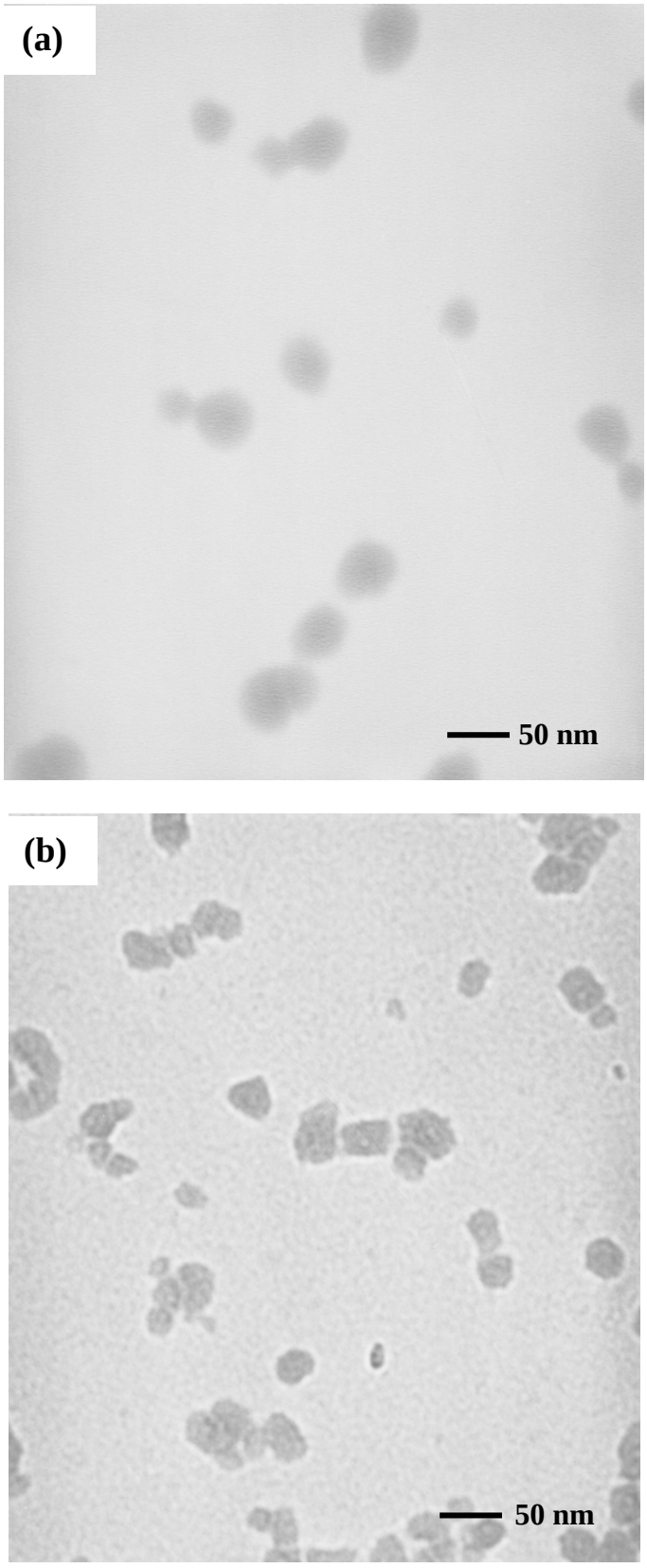

Fig. 2.2 TEM micrographs showing the shapes of the nano particles in the resulting PEEK nanocomposites: (a) SiO_2 (30 nm) and (b) Al_2O_3 (30 nm).

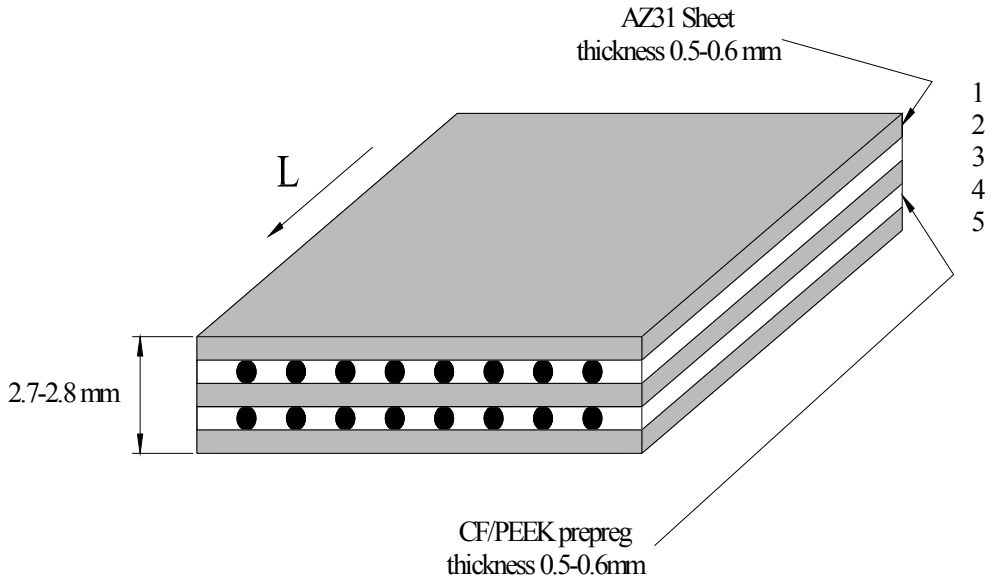

Fig. 2.3 Schematic drawing of the Mg based laminated composite, layers 1, 3 and 5 are Mg and layers 2 and 4 are APC-2 (with 4 foils). The longitudinal direction is indicated.

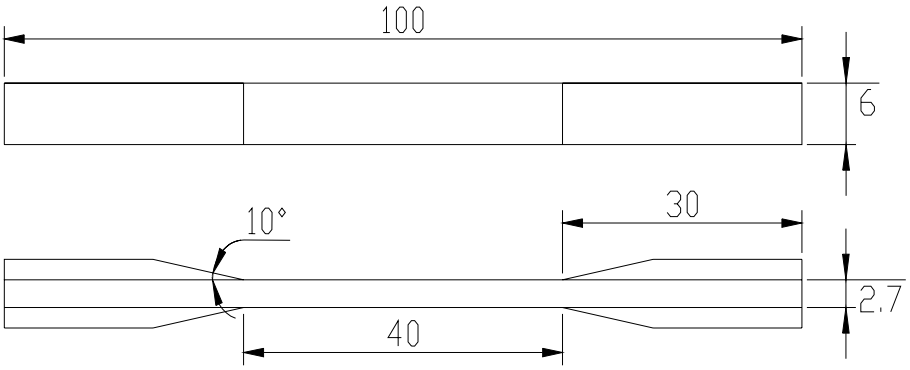

Fig. 2.4 The geometry and dimensions of tensile test spcimen of Mg/CF/PEEK laminated composite, laps shown in figure are the copper laps adhered. Unit: mm.

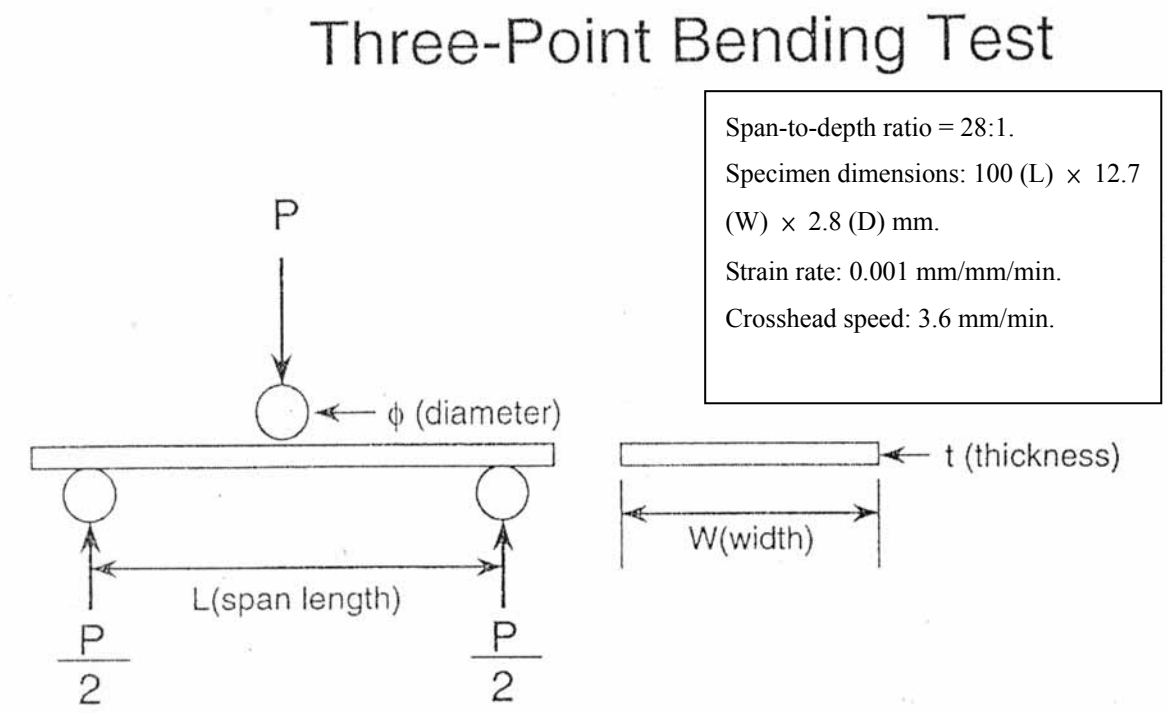

Fig. 2.5 The geometry and dimensions of flexural test.

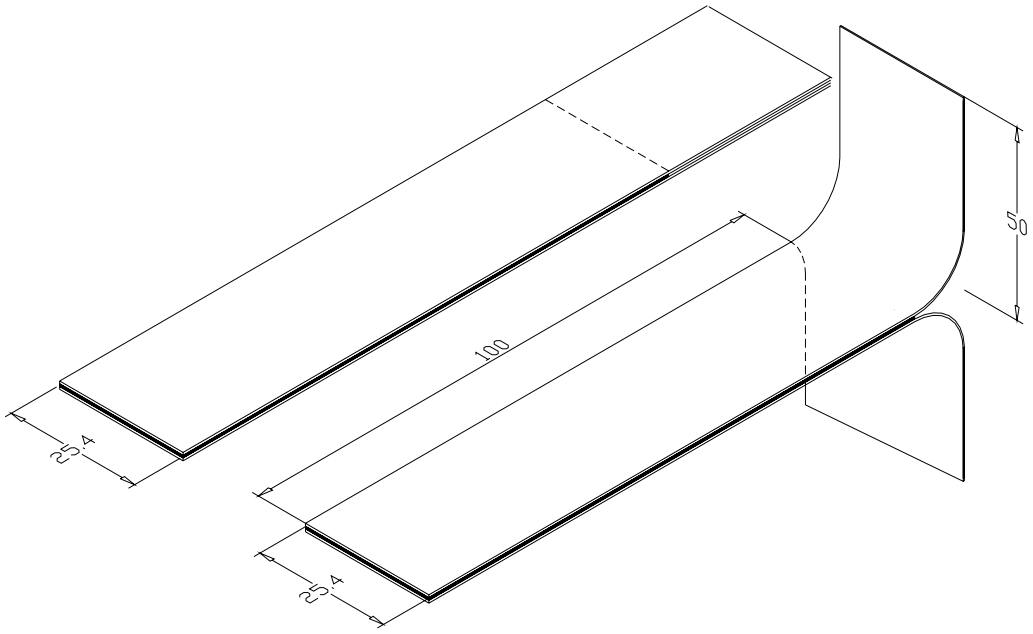

Fig. 2.6 The geometry of specimen for T-Peel test. Unit: mm.

Fig. 2.7 Vacuum hot-press for the fabrications of SiO_2 and Al_2O_3 particulates filled PEEK nanocomposites.

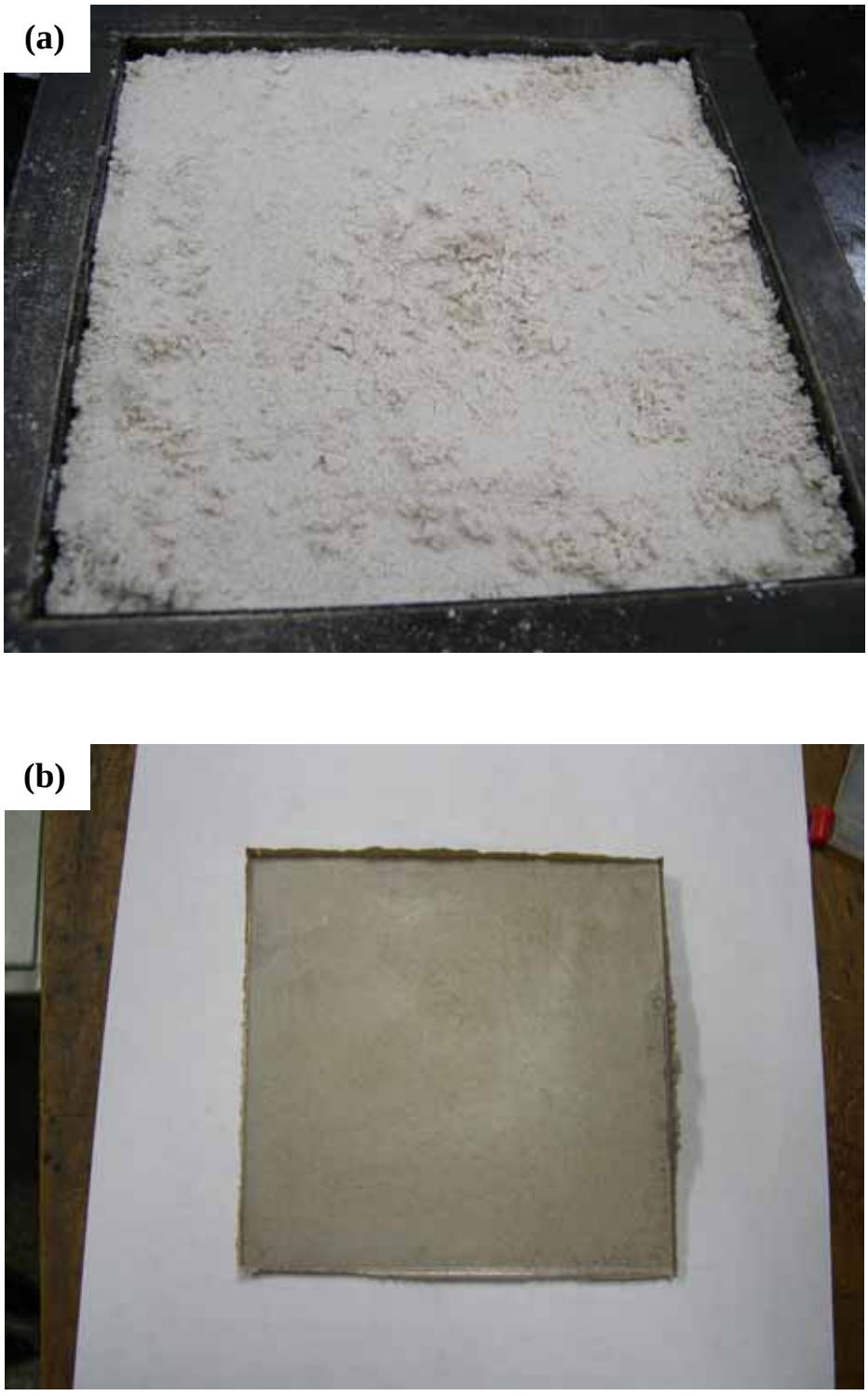

Fig. 2.8 Fabrication of SiO_2 or Al_2O_3 particulates filled PEEK nanocomposite, (a) molding, (b) fabricated PEEK nanocomposite.

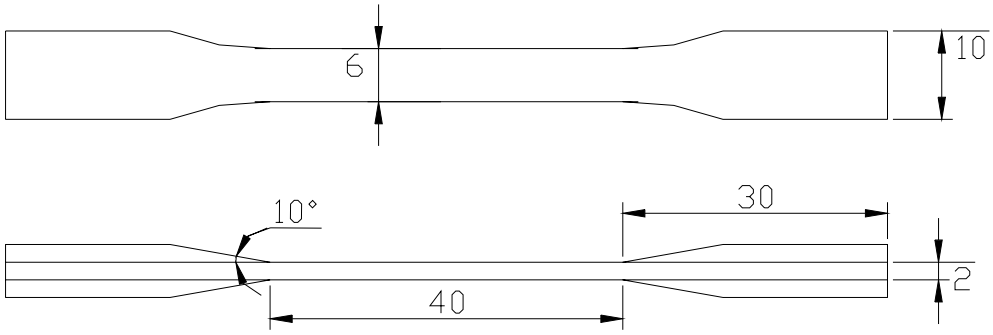

Fig. 2.9 The geometry and dimensions of tensile test specimen of particulates filled PEEK nanocomposite, laps shown in figure are the copper laps adhered. Unit: mm.

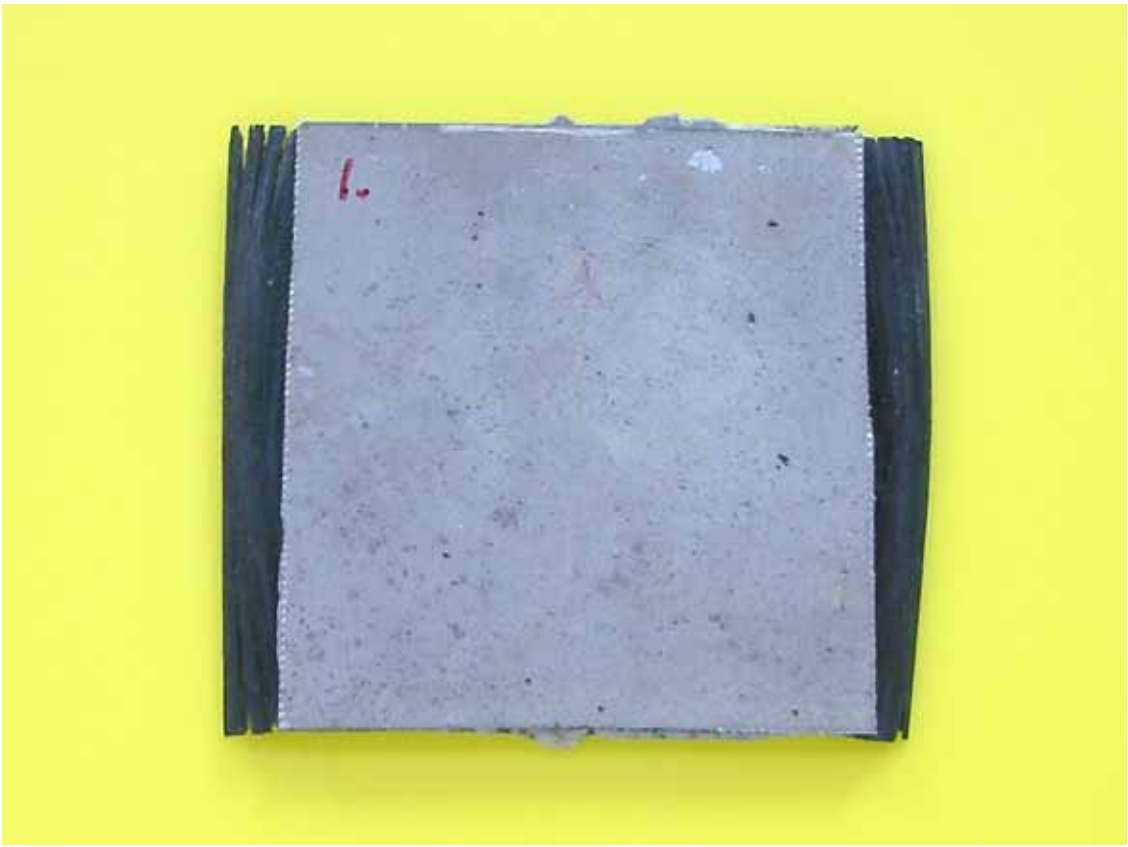

Fig. 3.1 Mg/APC-2 laminate with 4 plies of APC-2 prepreg sandwiched by two AZ31 Mg sheets formed at 400^{o}C under 1.1 MPa (sample 1 in Table 3.1).

Fig. 3.2 Mg/APC-2 laminate with 4 plies of APC-2 prepreg sandwiched by two AZ31 Mg sheets formed at 400^{o}C under 0.7 MPa (sample 2 in Table 3.1).

Fig. 3.3 Mg/APC-2 laminate with 4 plies of APC-2 prepreg sandwiched by two AZ31 Mg sheets formed at 400^{o}C under 0.7 MPa (sample 3 in Table 3.1).

Fig. 3.4 Mg/APC-2 laminate with 4 plies of APC-2 prepreg sandwiched by two AZ31 Mg sheets formed at 400 ^{o}C under 1.6 MPa (sample 4 in Table 3.1).

Fig. 3.5 Mg/APC-2 laminate with 3 plies of APC-2 prepreg sandwiched by two AZ31 Mg sheets formed at 400^{o}C under 1.0 MPa (sample 5 in Table 3.1).

Fig. 3.6 Mg/APC-2 laminate with 2 plies of APC-2 prepreg each layer and laminated in the stacking sequence of Mg/ APC-2/Mg/APC-2/Mg formed at 400^{o}C under 0.7 MPa (sample 6 in Table 3.1).

Fig. 3.7 Mg/APC-2 laminate with 2 plies of APC-2 prepreg each layer and laminated in the stacking sequence of Mg/ APC-2/Mg/APC-2/Mg formed at 400^{o}C under 1.4 MPa (sample 7 in Table 3.1).

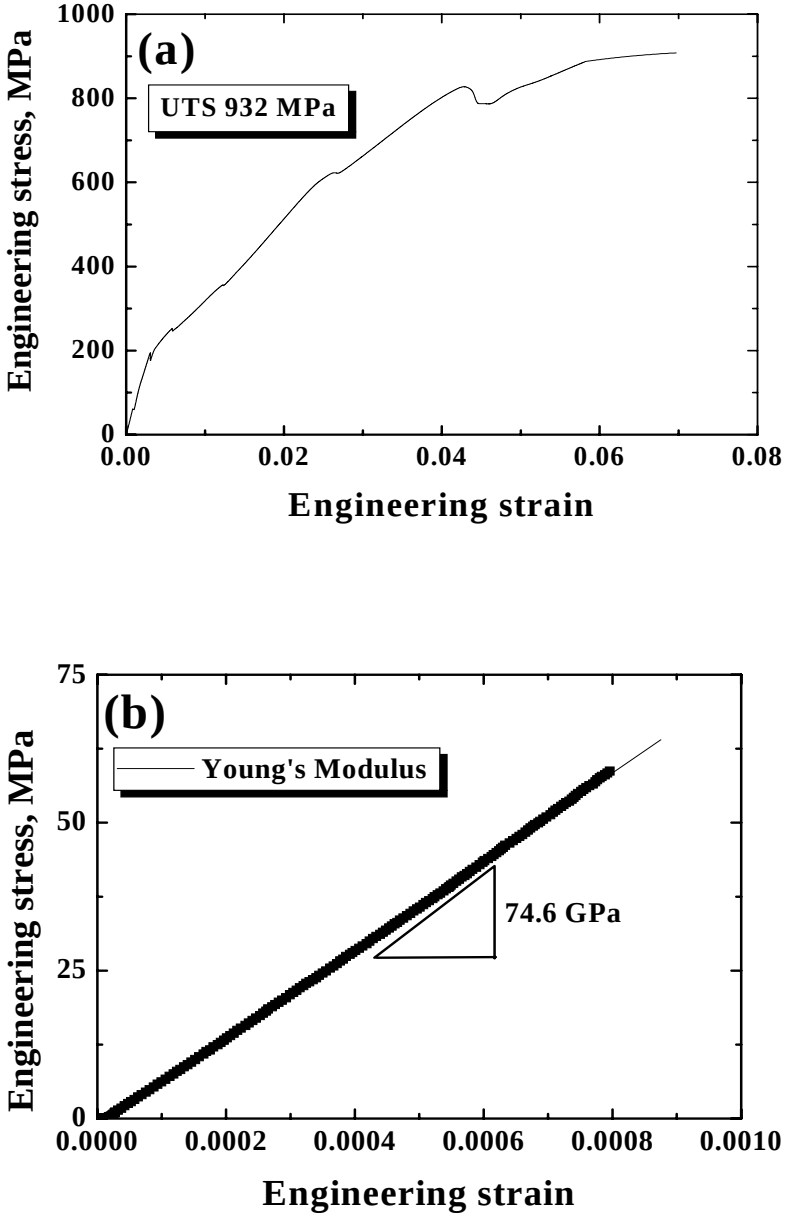

Fig. 3.8 (a) Room temperature tensile stress strain curve of the Mg/CF/PEEK Mg based laminated composite along the longitudinal direction, and (b) extraction of the Young's modulus of the Mg/CF/PEEK Mg based laminated composite.

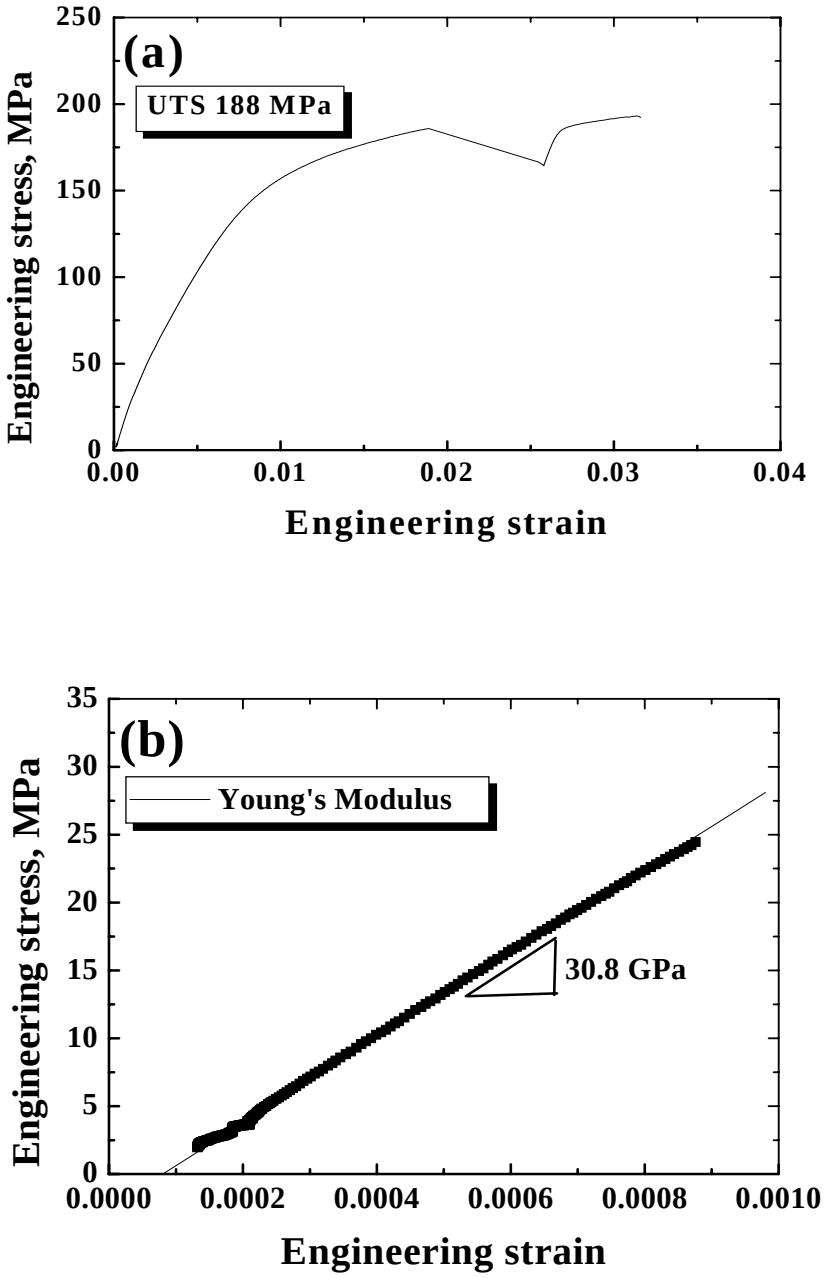

Fig. 3.9 (a) Room temperature tensile stress strain curve of the Mg/CF/PEEK Mg based laminated composite along the transverse direction, and (b) extraction of the Young's modulus of the Mg/CF/PEEK Mg based laminated composite.

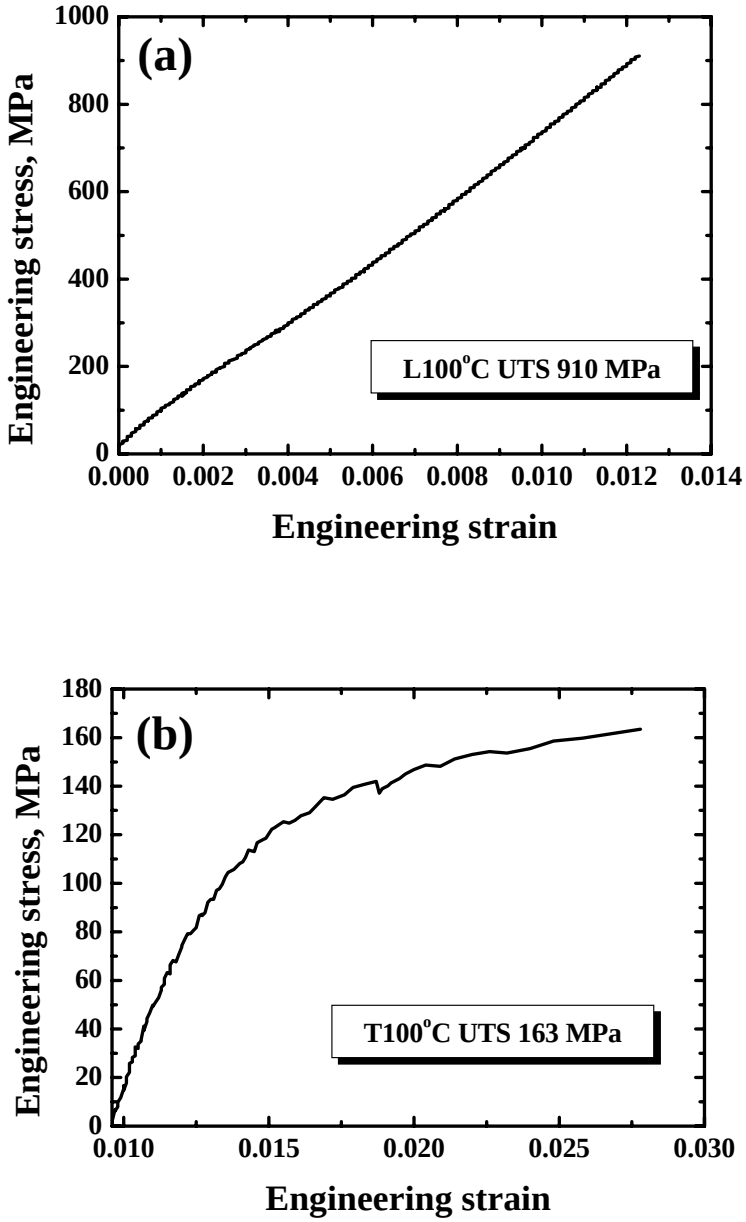

Fig. 3.10 Tensile stress strain curve of the Mg/CF/PEEK Mg based laminated composite at 100°C along the (a) longitudinal and (b) transverse directions.

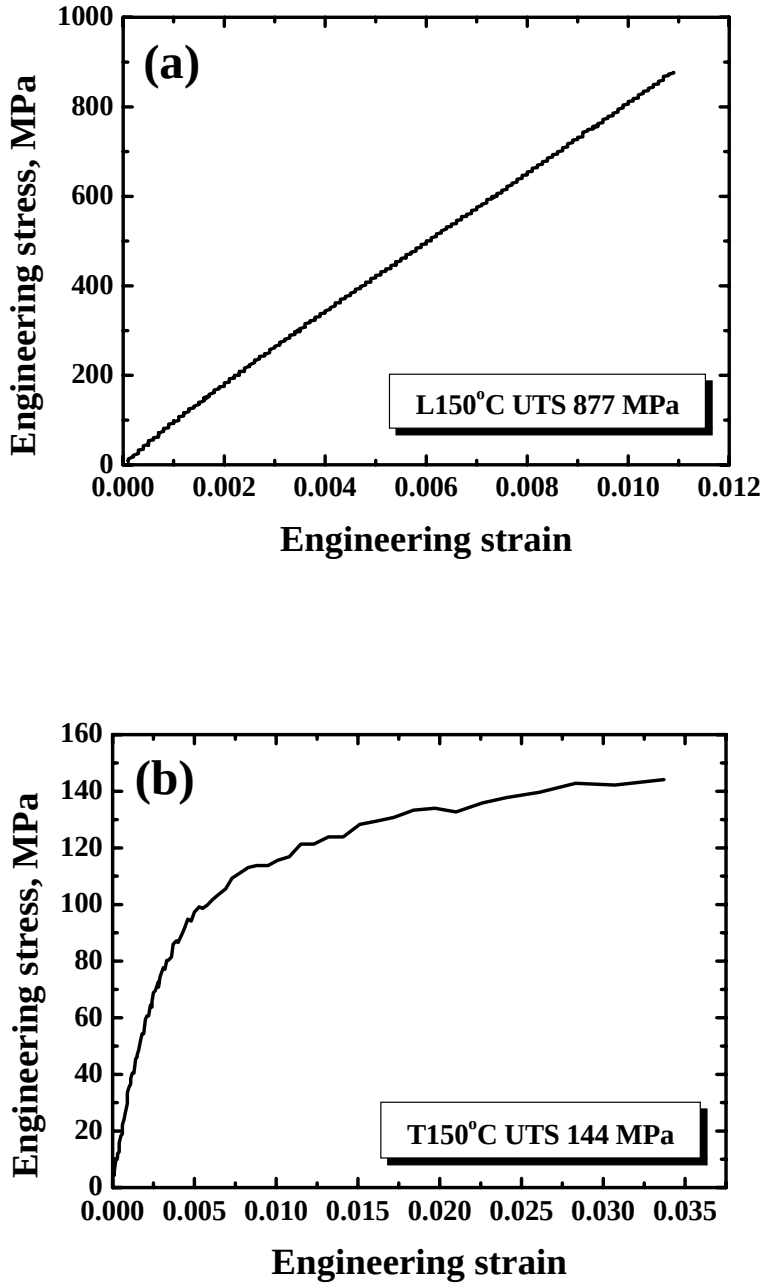

Fig. 3.11 Tensile stress strain curve of the Mg/CF/PEEK Mg based laminated composite at 150^{o}C along the (a) longitudinal and (b) transverse directions.

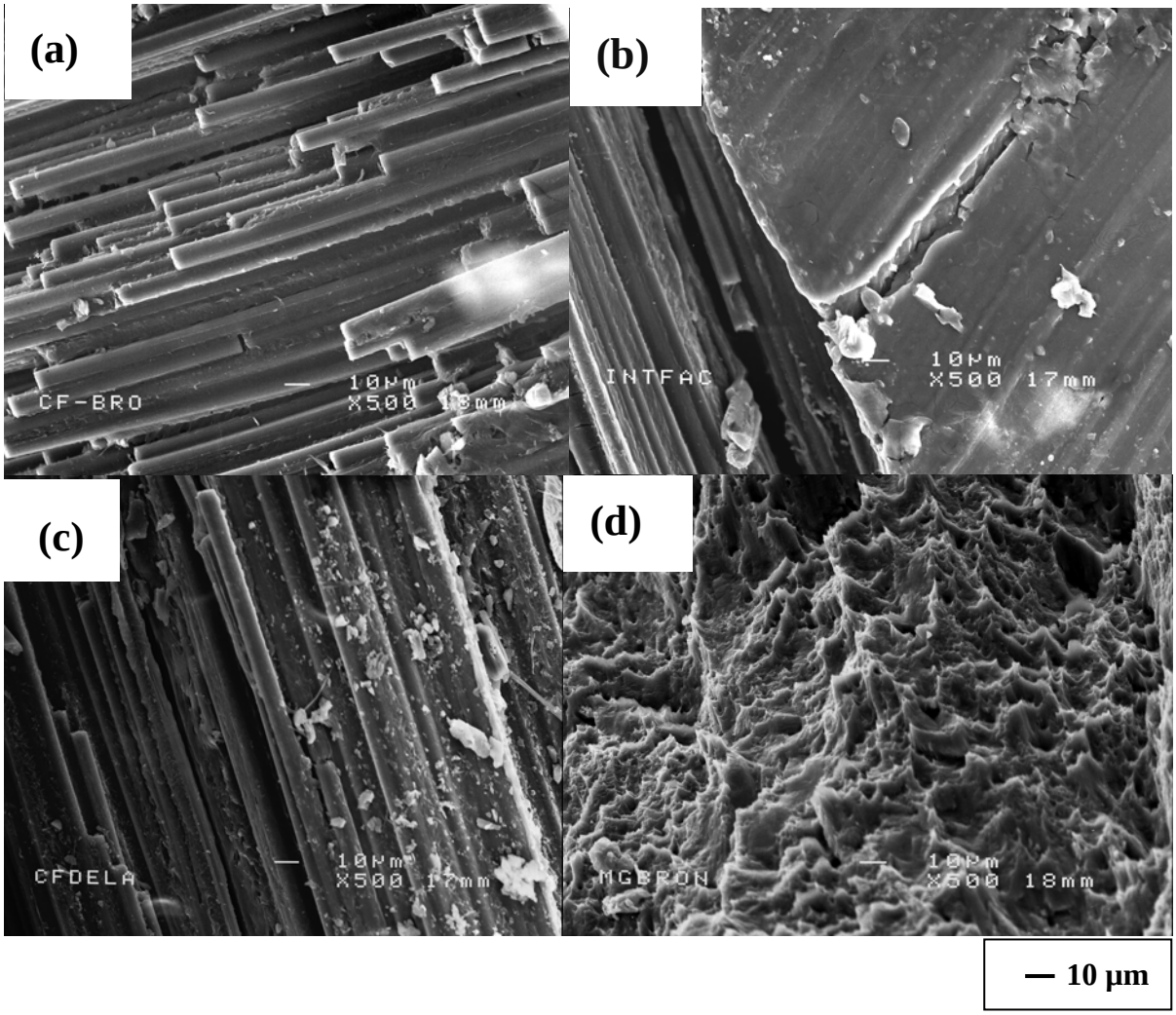

Fig. 3.12 SEM micrographs of the room-temperature fractured specimens of Mg/CF/PEEK laminated composite, taken from the longitudinal specimens.

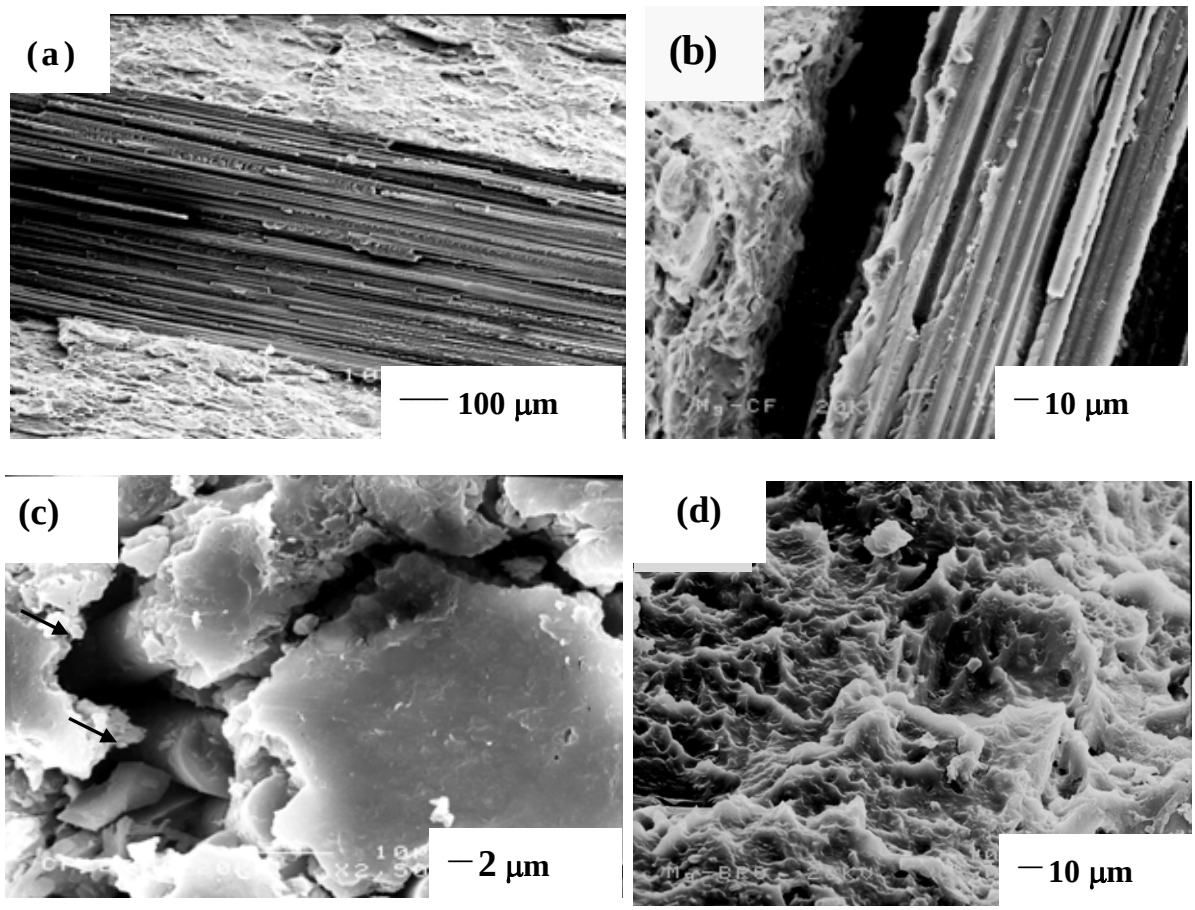

Fig. 3.13 SEM micrographs of the room-temperature fractured specimens of Mg/CF/PEEK laminated composite, taken from the transverse specimens.

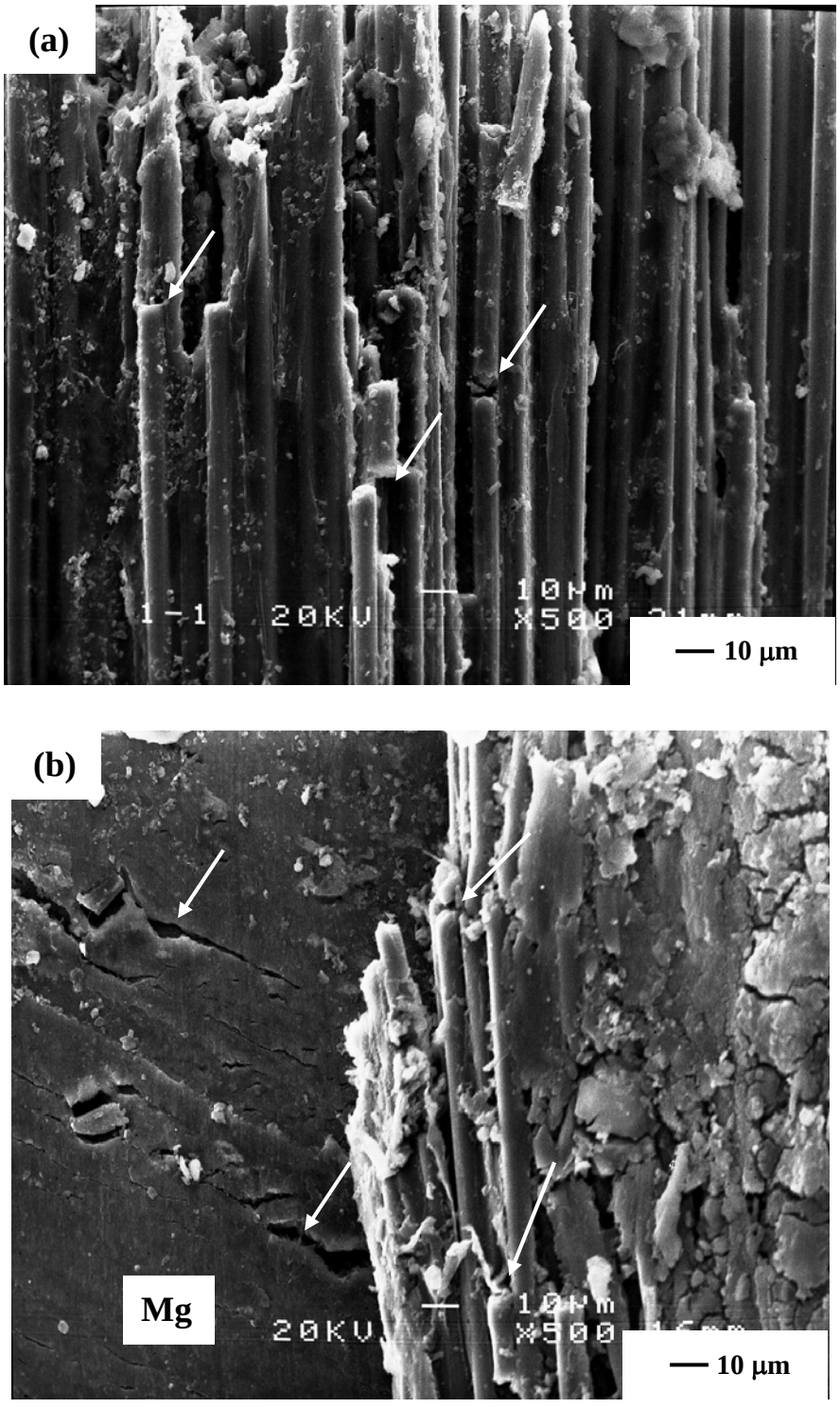

Fig. 3.14 SEM micrographs of the fractured specimens of Mg/CF/PEEK laminated composite loaded at 100^{o}C, taken from the longitudinal specimens, showing (a) the carbon fiber broken in the APC-2 prepreg, and (b) the correlation of the fracture positions in the Mg phase and the carbon fibers.

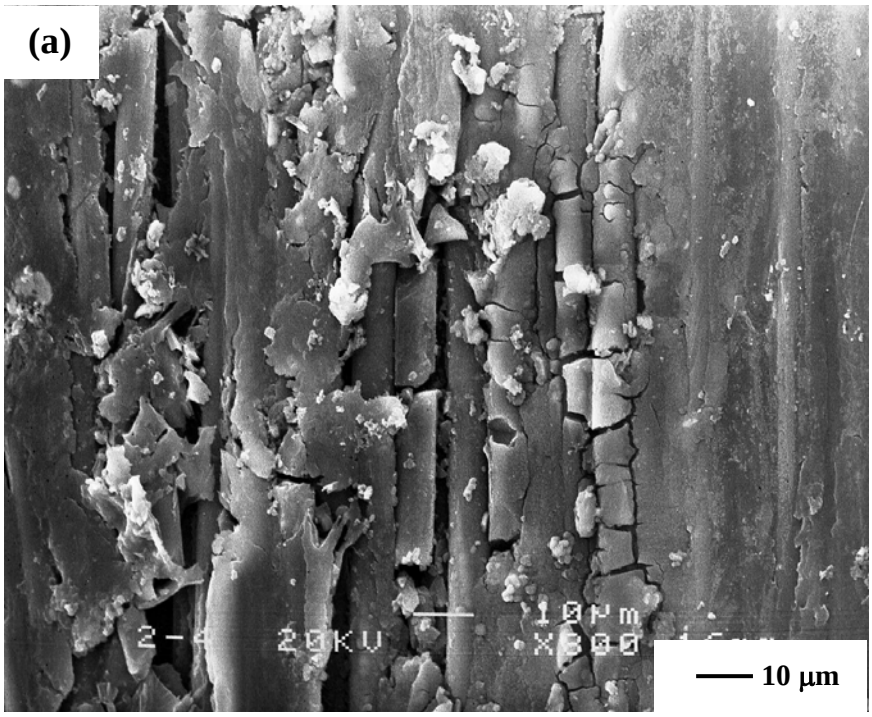

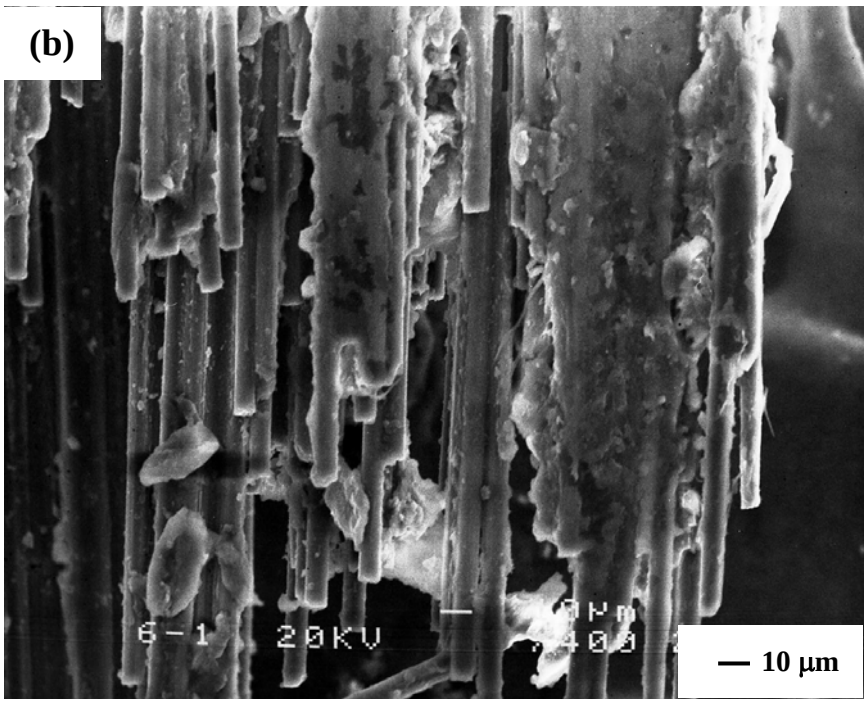

Fig. 3.15 SEM micrographs of the fractured specimens of Mg/CF/PEEK laminated composite loaded at 150^{o}C , taken from the longitudinal specimens, showing (a) the carbon fiber broken in the APC-2 prepreg, and (b) the broken positions of the carbon occurring at different places, indicating the ductile fracture behavior in the Mg matrix.

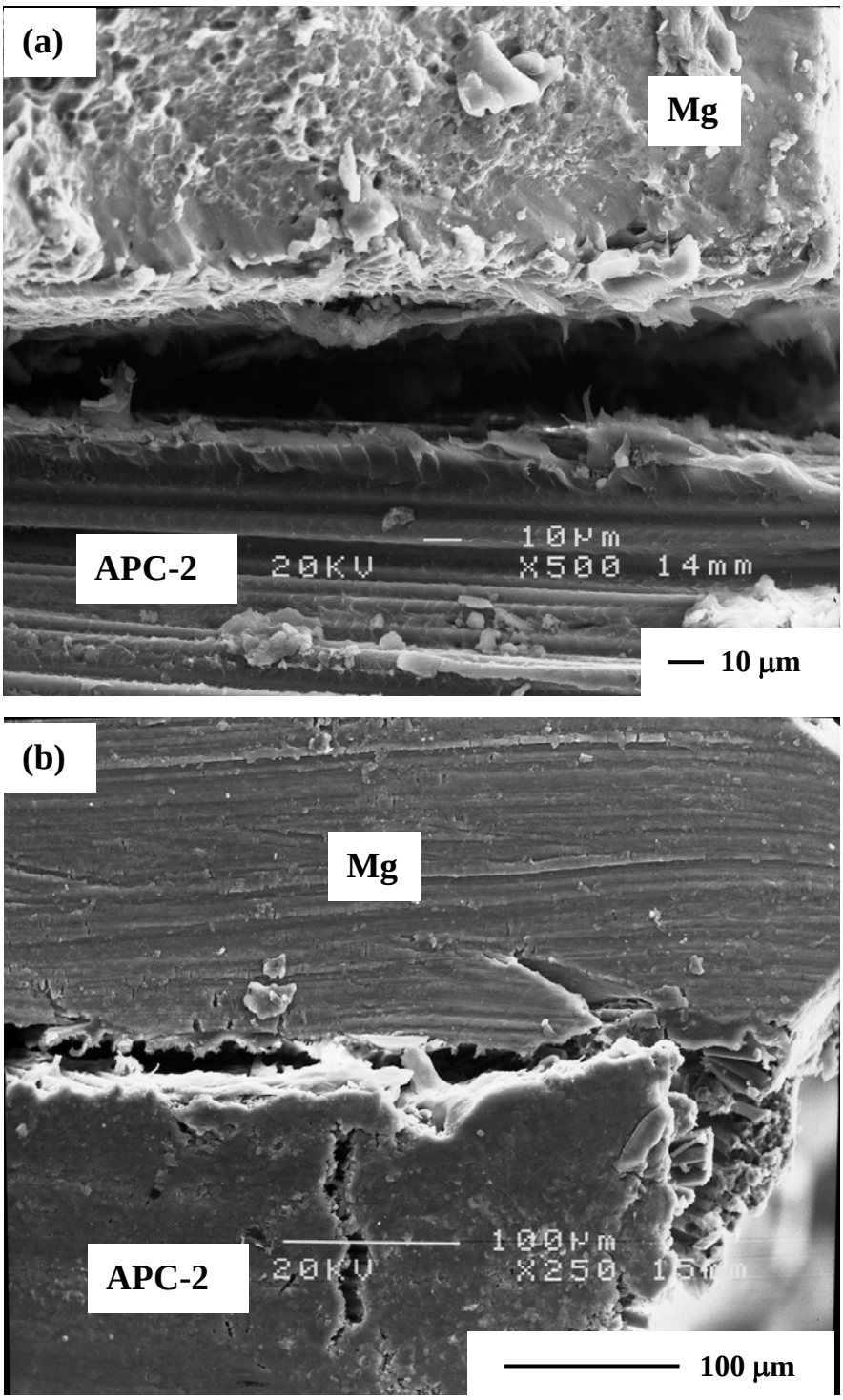

Fig. 3.16 SEM micrographs of the fractured specimens of Mg/CF/PEEK laminated composite loaded at 100^{o}C, taken from the transverse specimens, showing (a) the interface de-attachment fracture and dimples in the Mg phase and, (b) the interface delamination and the microcrack in the APC-2 phase.

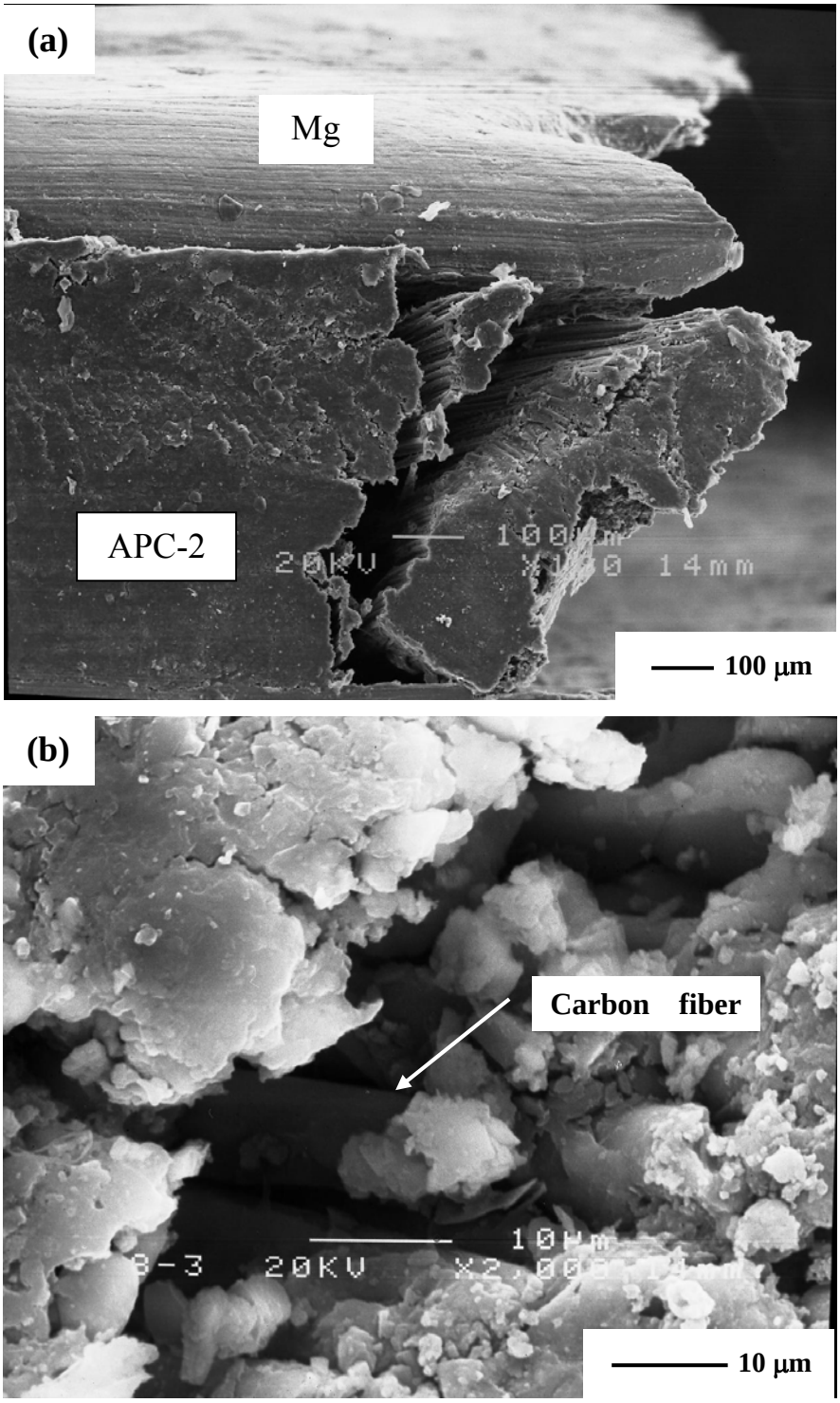

Fig. 3.17 SEM micrographs of the fractured specimens of Mg/CF/PEEK laminated composite loaded at 150°C, taken from the transverse specimens, showing (a) the interface fracture behavior and, (b) the de-attachment behavior between the PEEK resin and the carbon fiber.

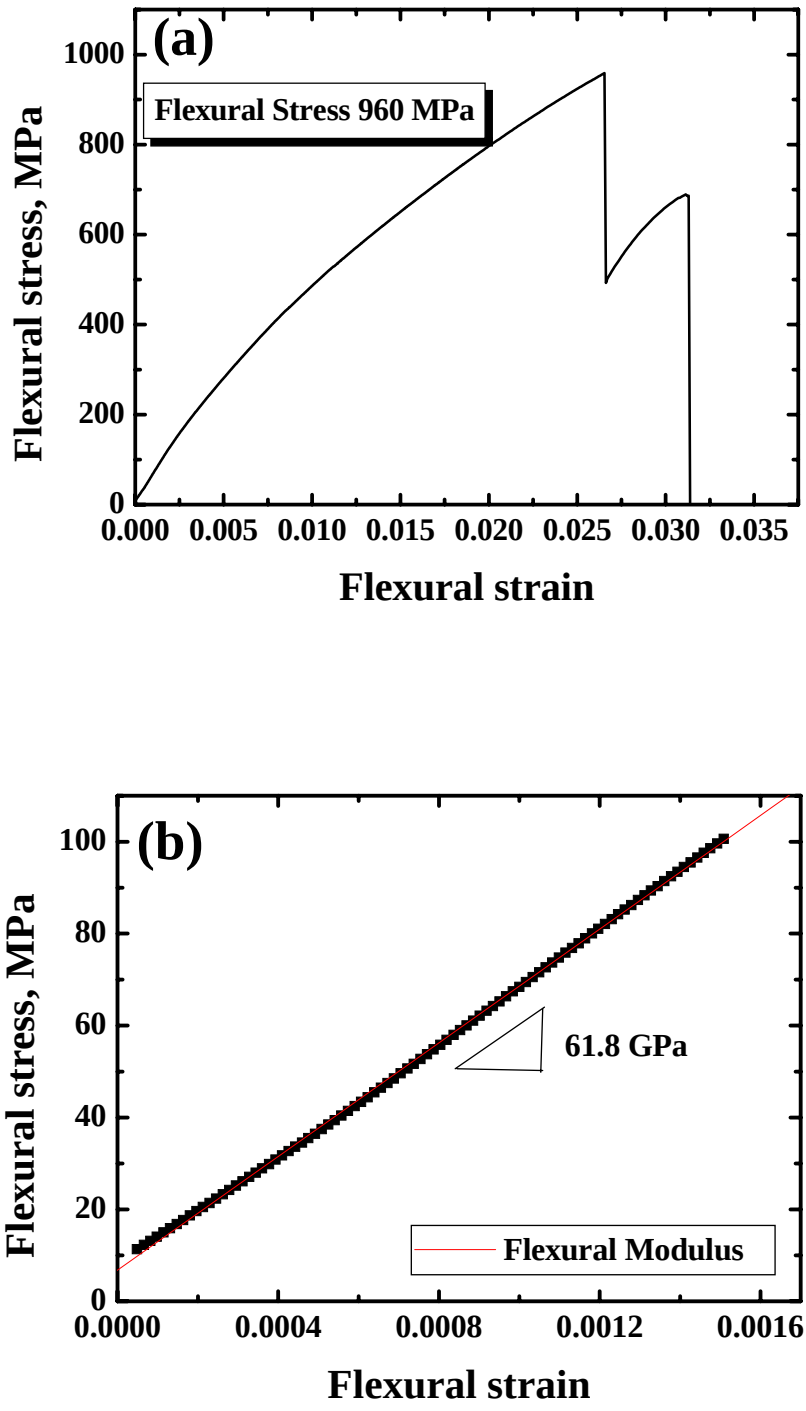

Fig. 3.18 (a) Room temperature flexural stress strain curve of the Mg/CF/PEEK Mg based laminated composite along the longitudinal direction, and (b) extraction of the flexural modulus of the Mg/CF/PEEK Mg based laminated composite.

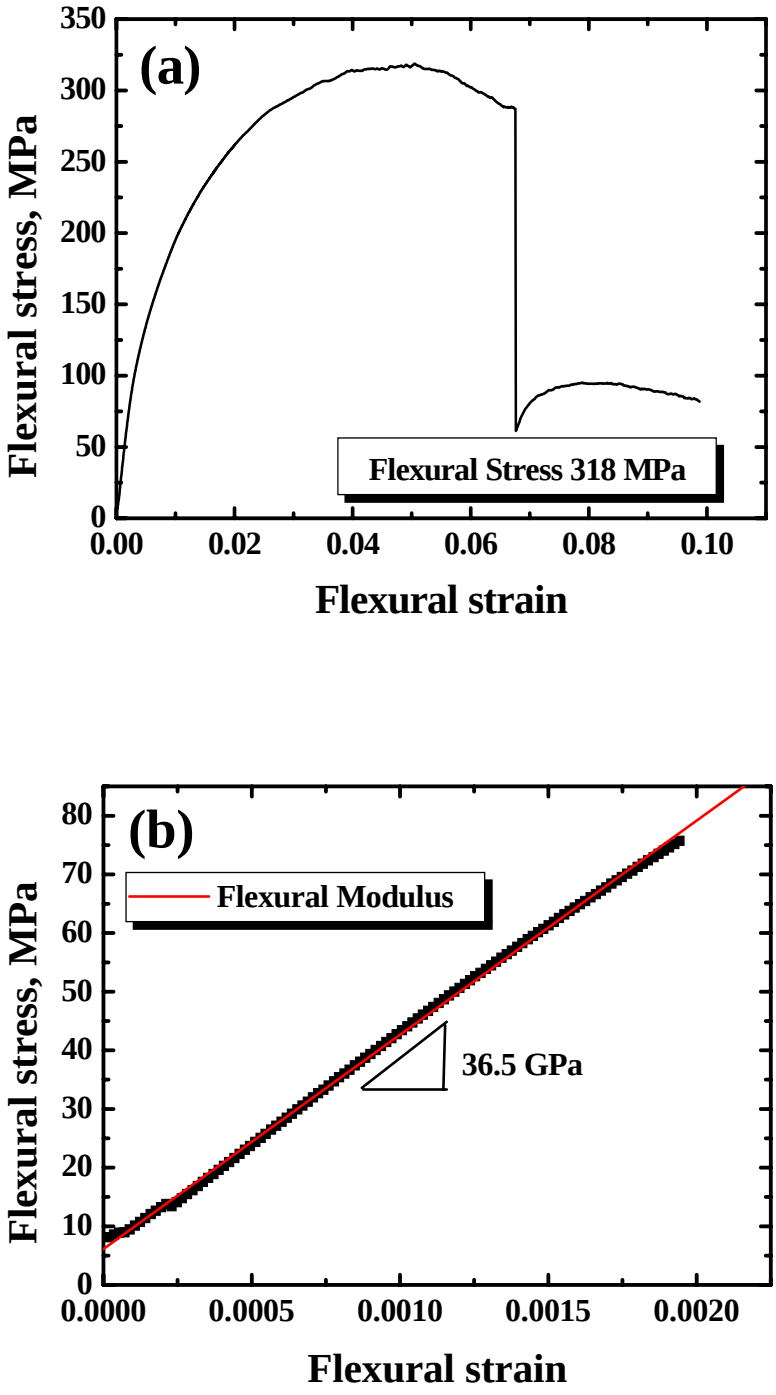

Fig. 3.19 (a) Room temperature flexural stress strain curve of the Mg/CF/PEEK Mg based laminated composite along the transverse direction, and (b) extraction of the flexural modulus of the Mg/CF/PEEK Mg based laminated composite.

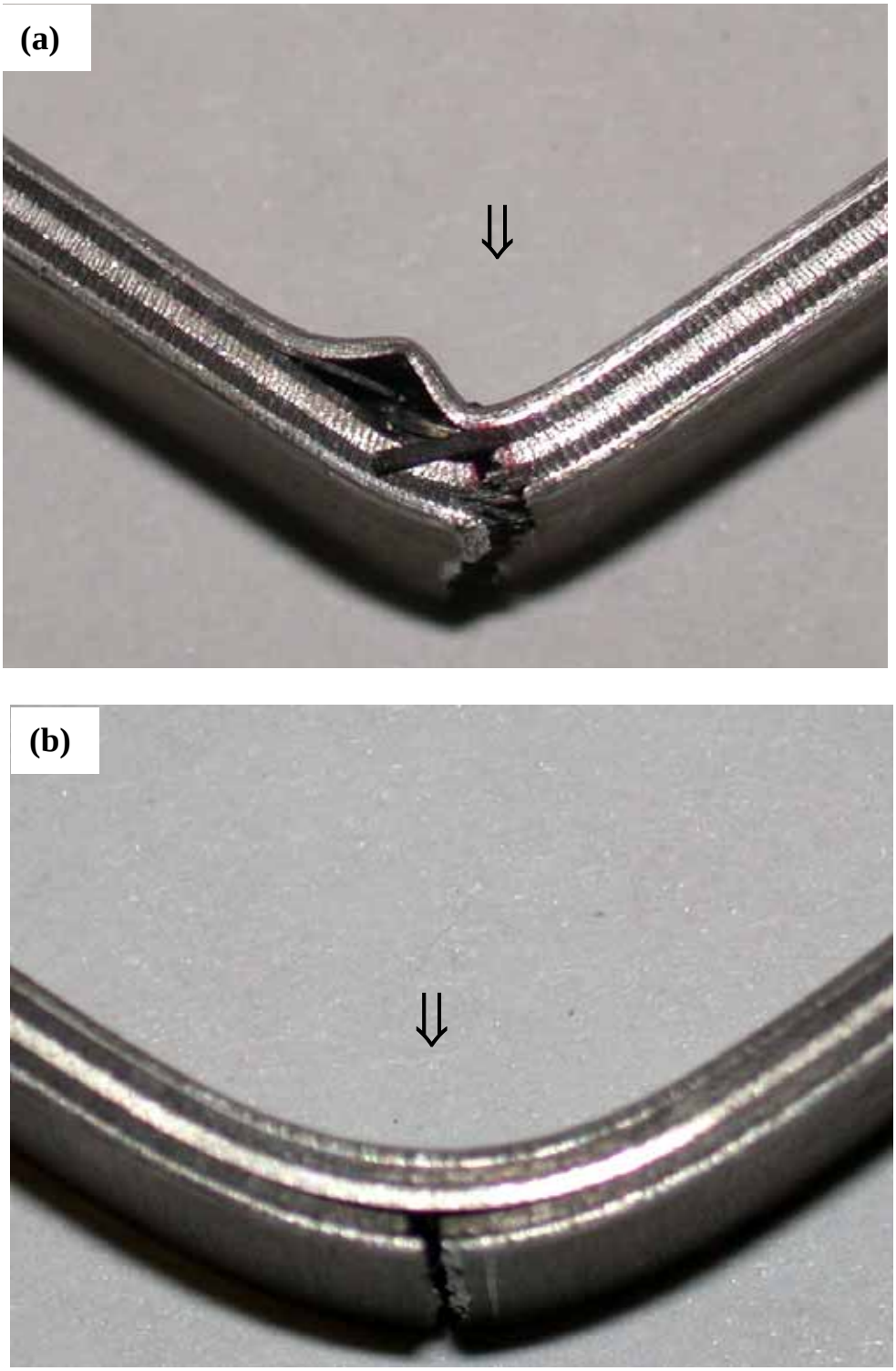

Fig. 3.20 Photographs of the fractured Mg/CF/PEEK laminated composites for the (a) longitudinal and (b) transverse configurations of carbon fibers. The loading direction is indicated.

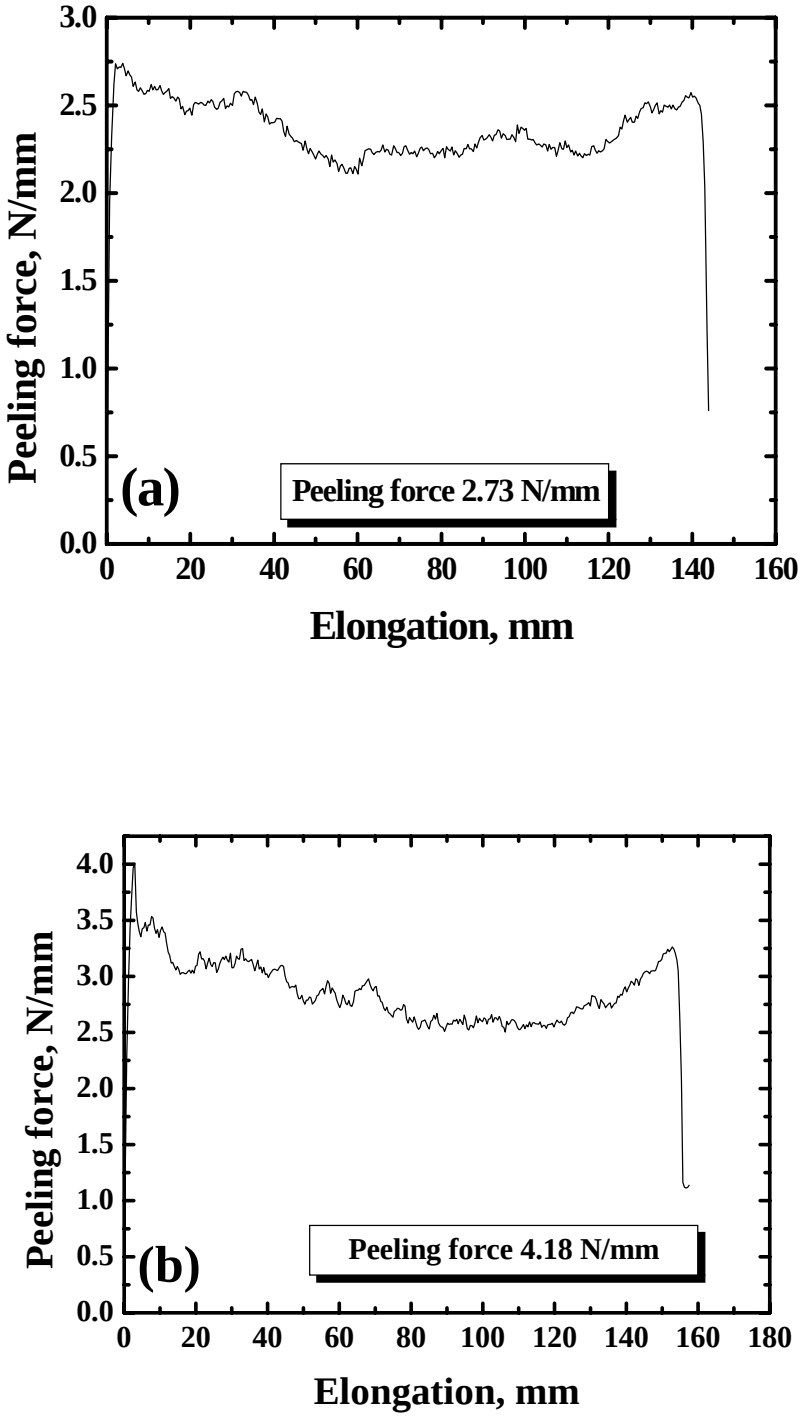

Fig. 3.21 Typical peeling test results for the Mg/CF/PEEK laminated composites along the (a) longitudinal and (b) transverse directions.

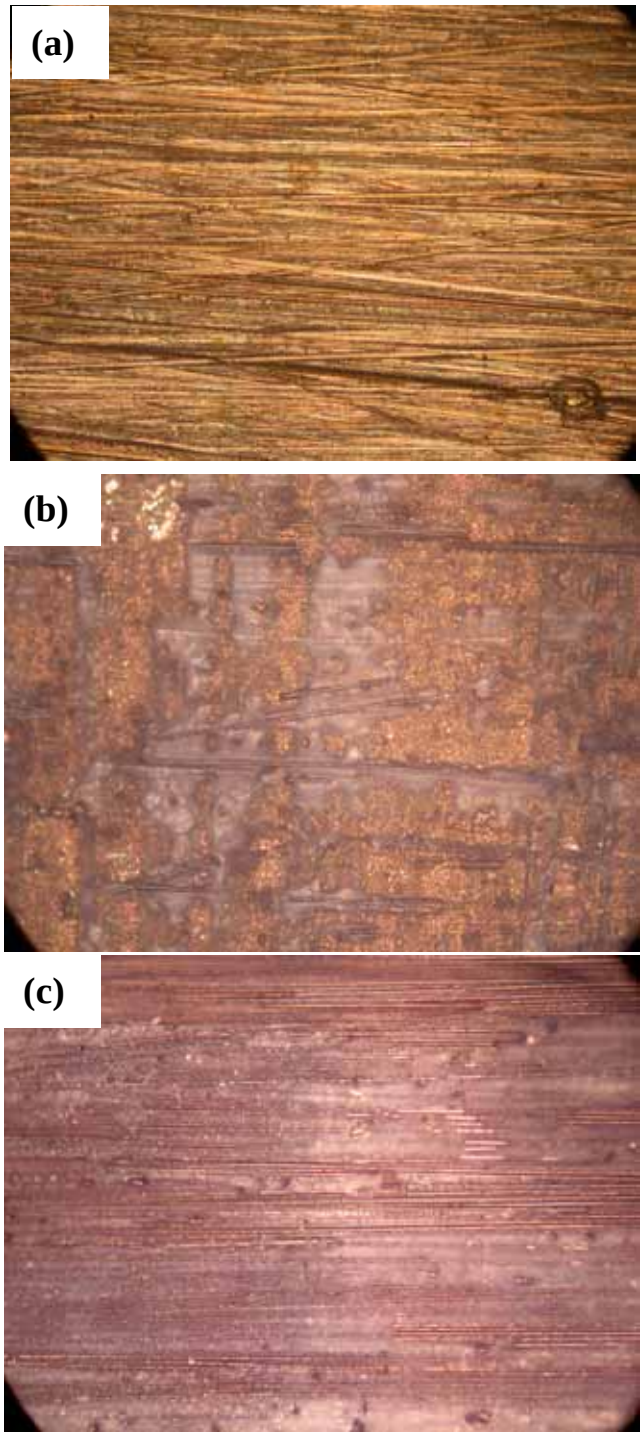

Fig. 3.22 OM micrographs taken from the peel-tested specimens with the longitudinal configurations of carbon fibers: (a) Mg layer without CrO_3 etching, (b) Mg layer with CrO_3 etching, and (c) APC-2 layer. The lighter-contrasted PEEK resin adhered on the Mg phase is evident in (b) and on carbon fibers in (c), and the broken carbon fibers stuck on the Mg phase in (b).

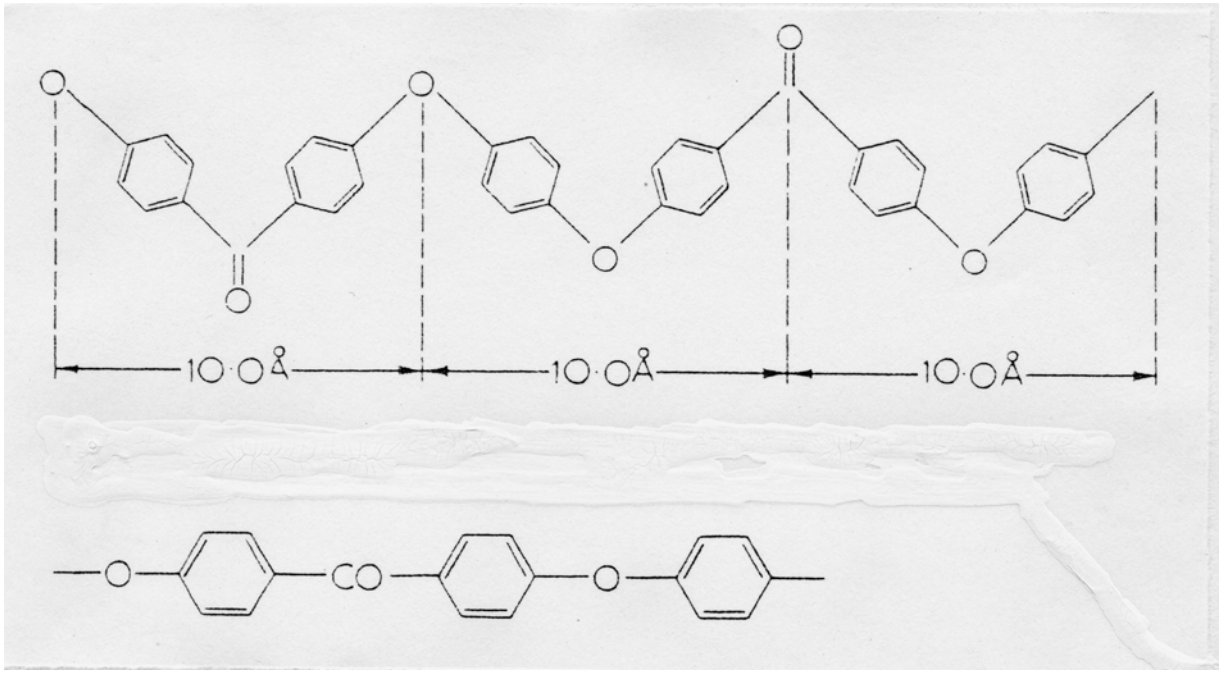

Fig. 3.23 Chemical structure of the PEEK polymer.

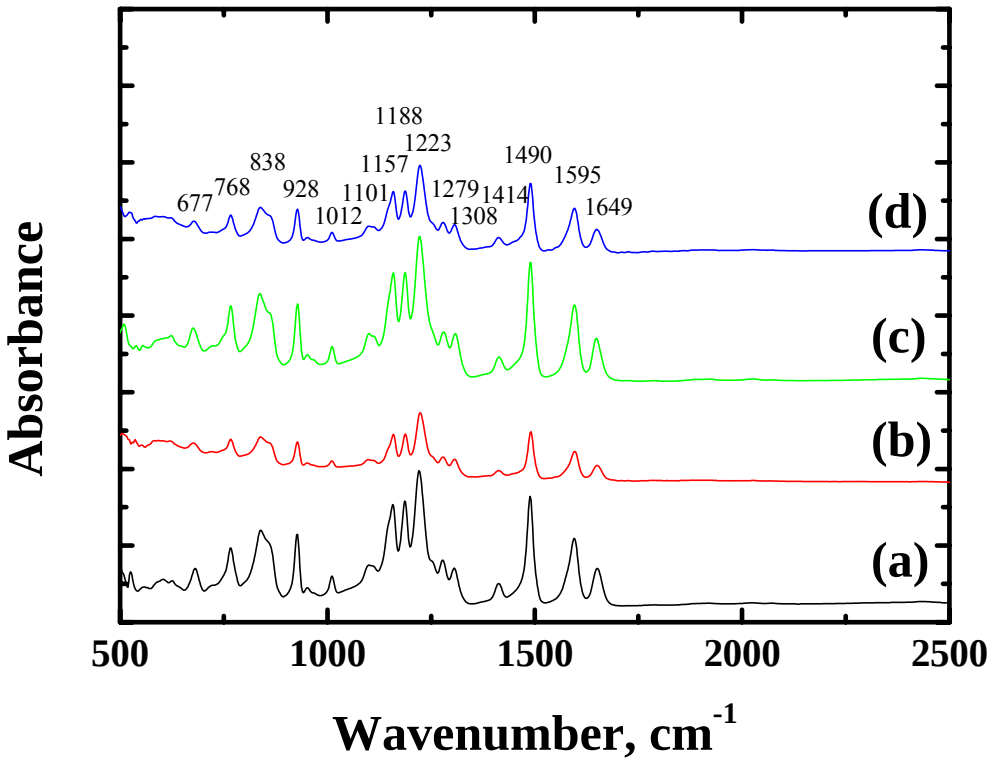

Fig. 3.24 FT-IR spectra on the (a) AS-4 prepreg, (b) etched CF-phase peeled from the Mg/APC-2 laminated composite, (c) unetched CF-phase peeled from the Mg/APC-2 laminated composite, and (d) etched Mg-phase peeled from the Mg/APC-2 laminated composite.

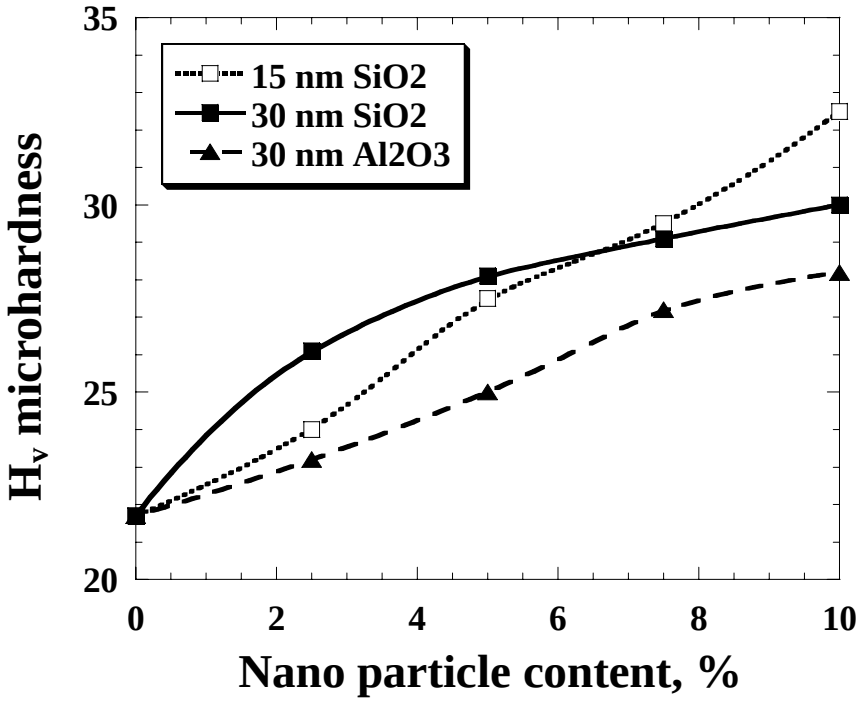

Fig. 3.25 Variations of the microhardness of the nanocomposites as a function of the nanoparticle content in wt%.

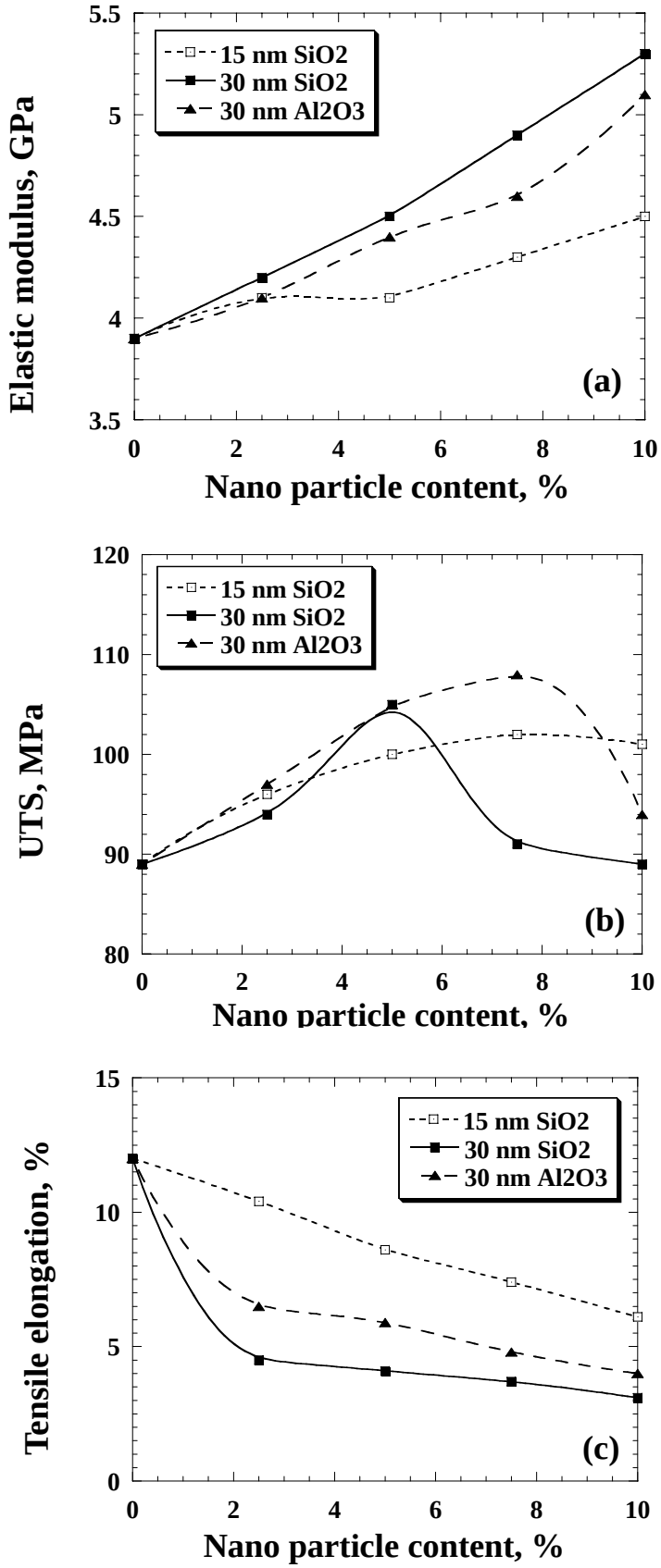

Fig. 3.26 Variations of the (a) Young's modulus *E*, (b) ultimate tensile stress UTS, and (c) tensile failure elongation *e* of the nanocomposites as a function of the particle content in wt%.

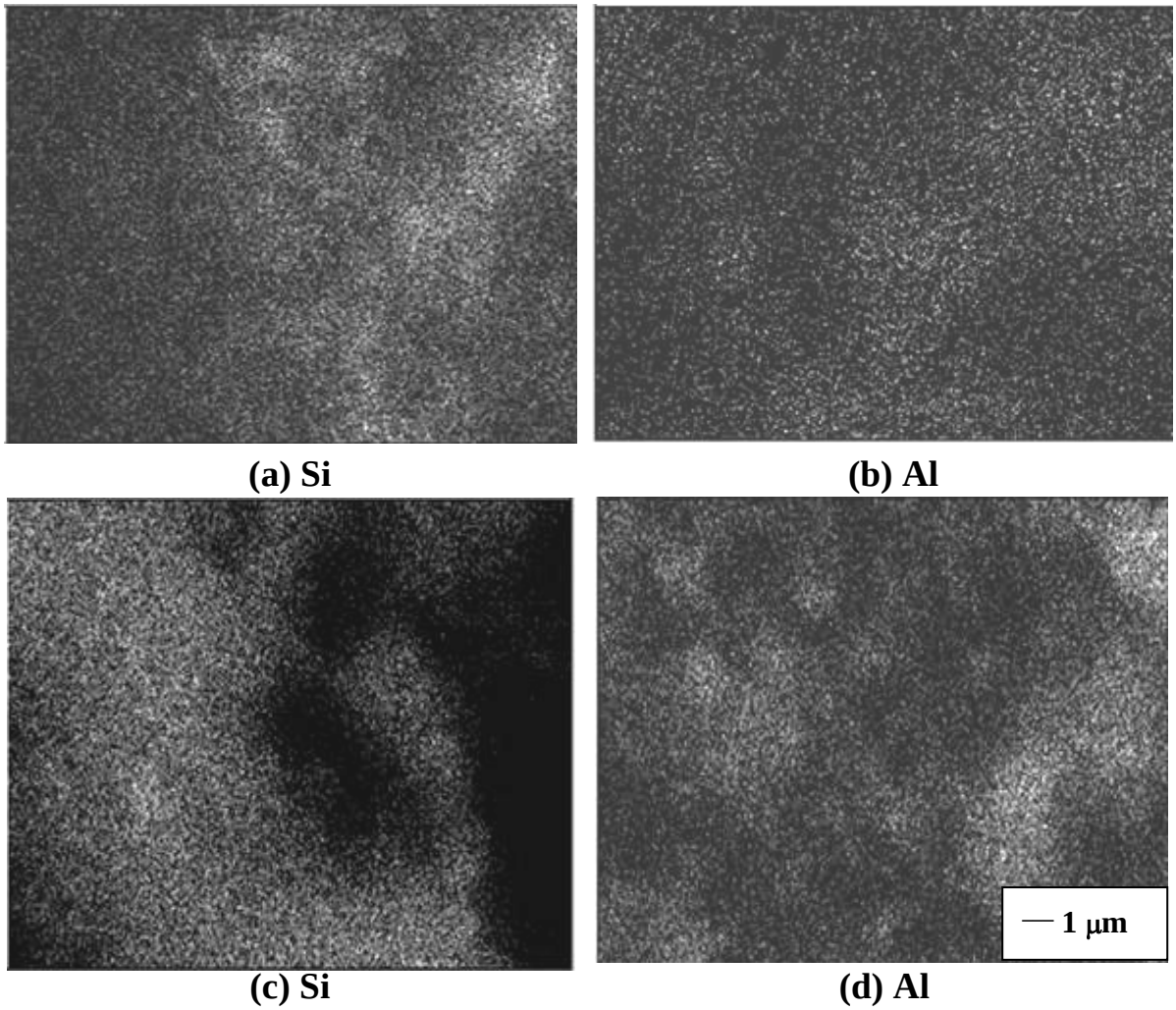

Fig. 3.27 SEM/EDS elemental mapping (Si or Al) for the composites with: (a) 5 wt% SiO_2, (b) 5 wt% Al_2O_3, (c) 7.5 wt% SiO_2, and (d) 7.5 wt% Al_2O_3.

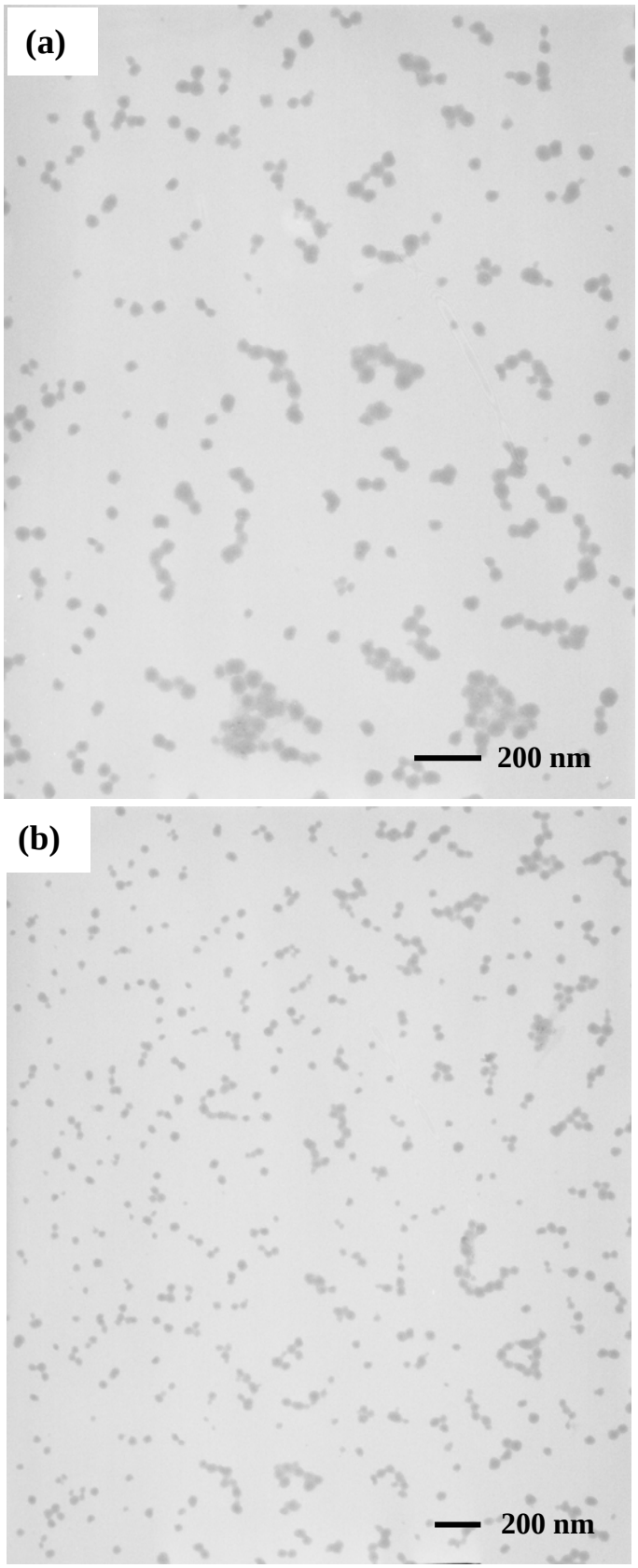

Fig. 3.28 TEM micrographs showing the distribution of the nano particles: (a) 2.5 wt% SiO_2 (15 nm) and (b) 5 wt% SiO_2 (15 nm).

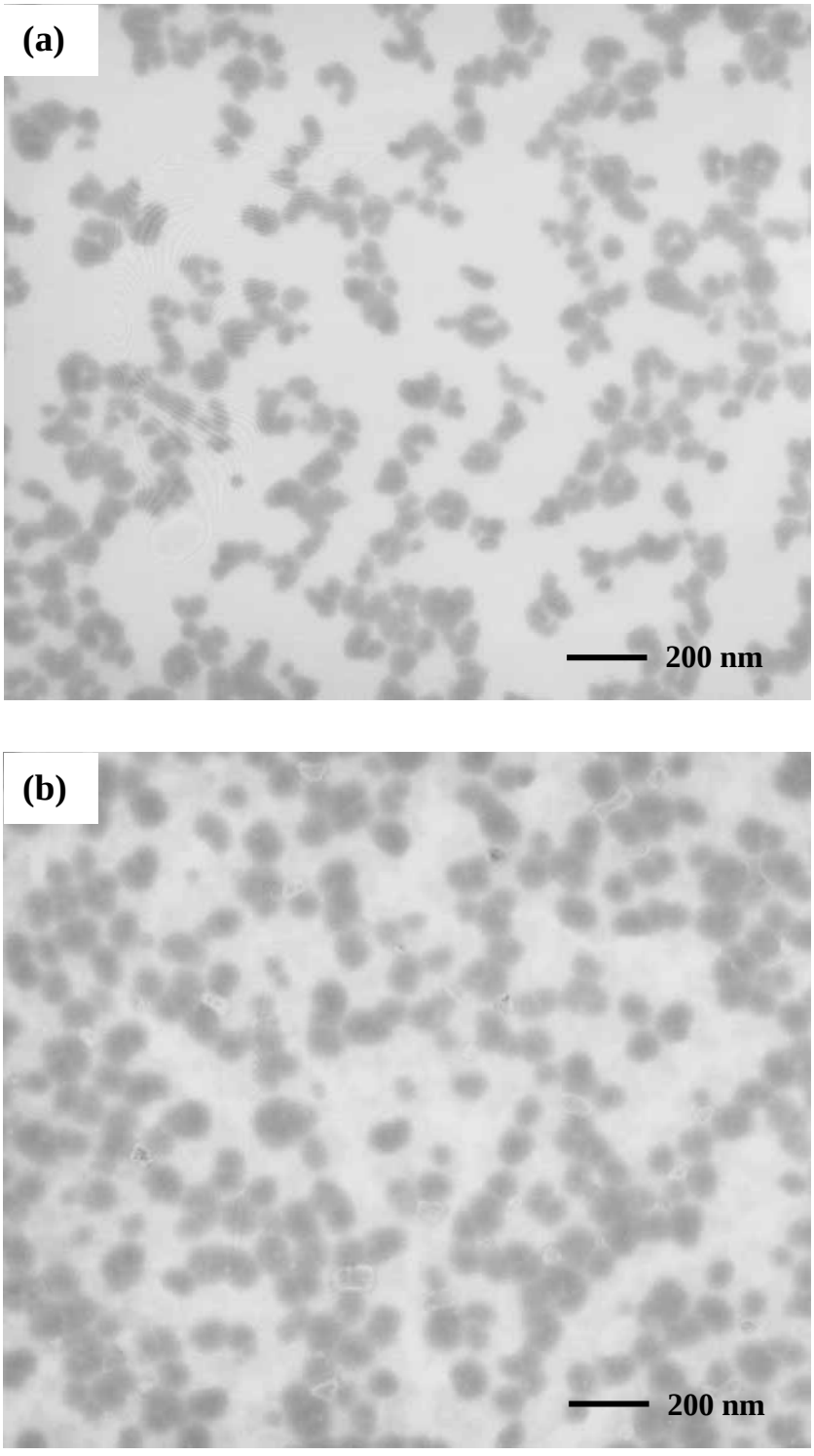

Fig. 3.29 TEM micrographs showing the distribution of the nano particles: (a) 2.5 wt% SiO_2 (30 nm) and (b) 5 wt% SiO_2 (30 nm).

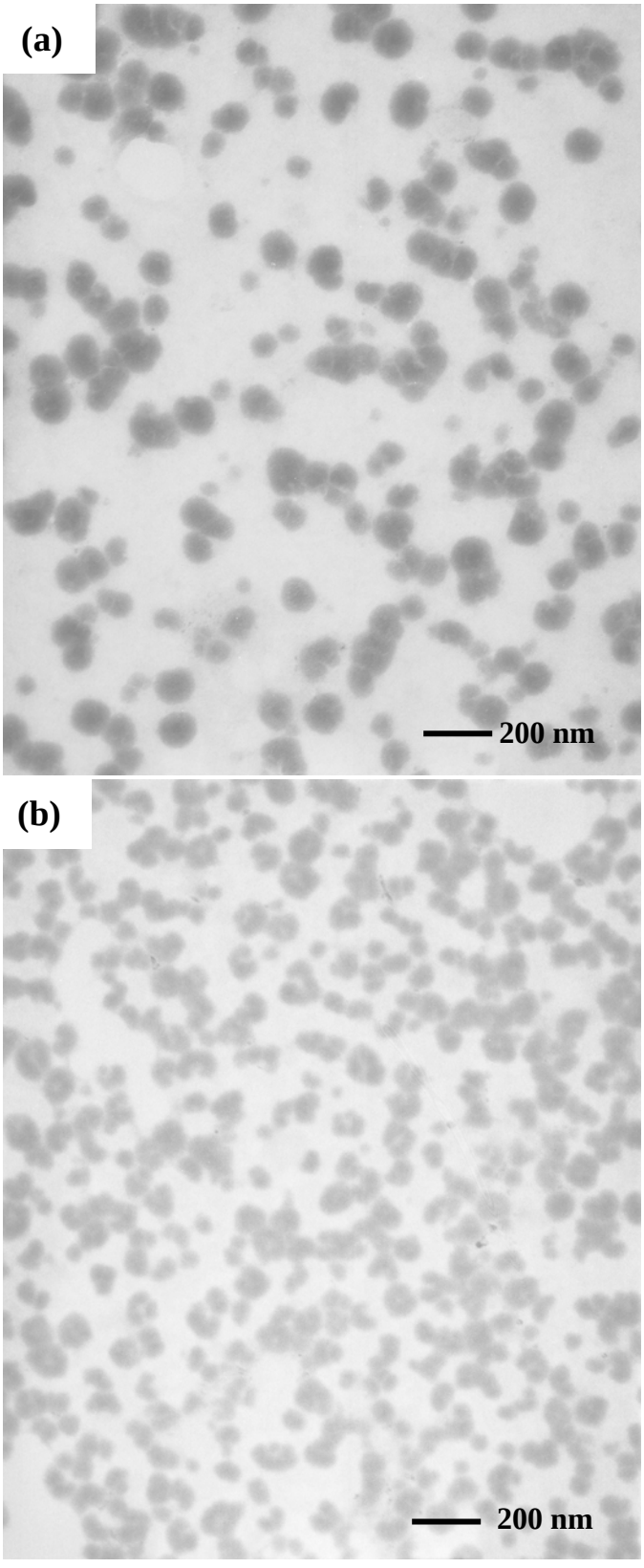

Fig. 3.30 TEM micrographs showing the distribution of the nano particles: (a) 2.5 wt% Al_2O_3 (30 nm) and (b) 5 wt% Al_2O_3 (30 nm).

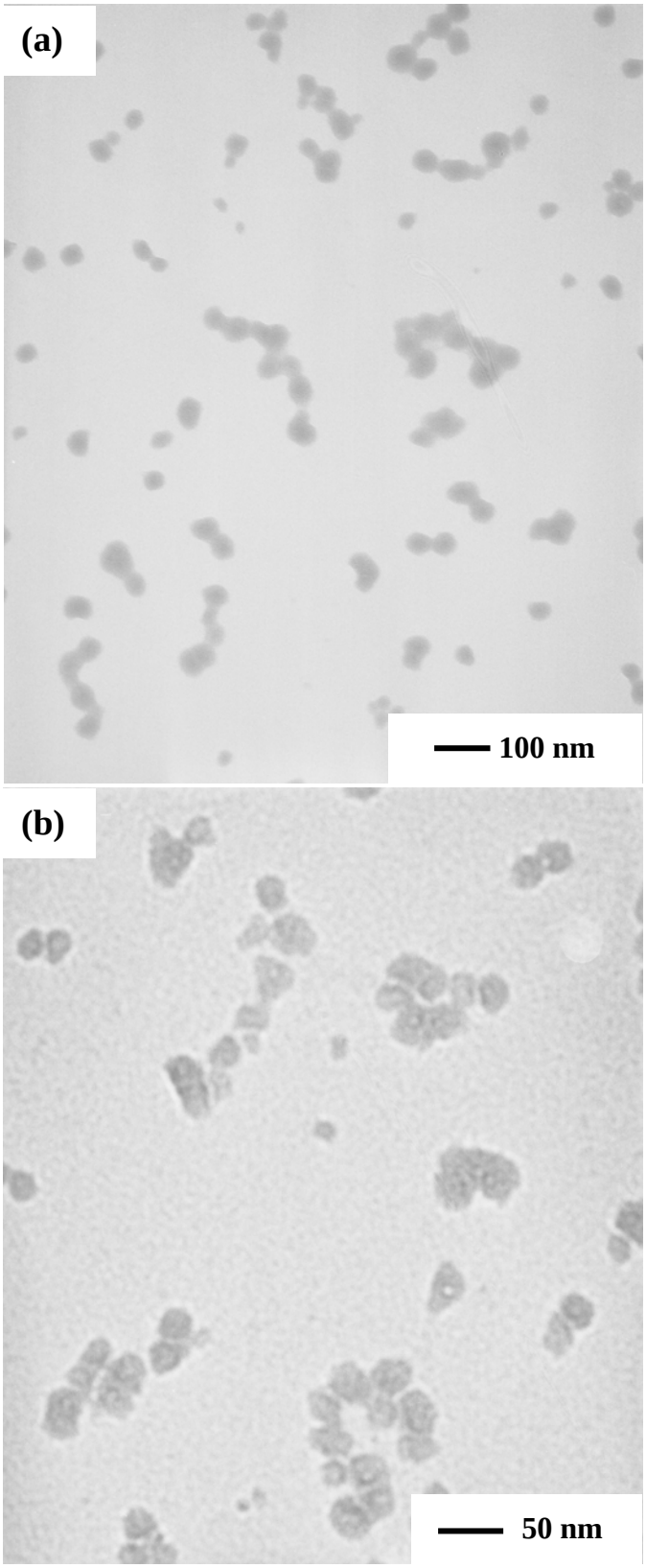

Fig. 3.31 TEM micrographs showing the distribution of the nano particles: (a) 2.5 wt% SiO_2 (15 nm) and (b) 2.5 wt% Al_2O_3 (30 nm).

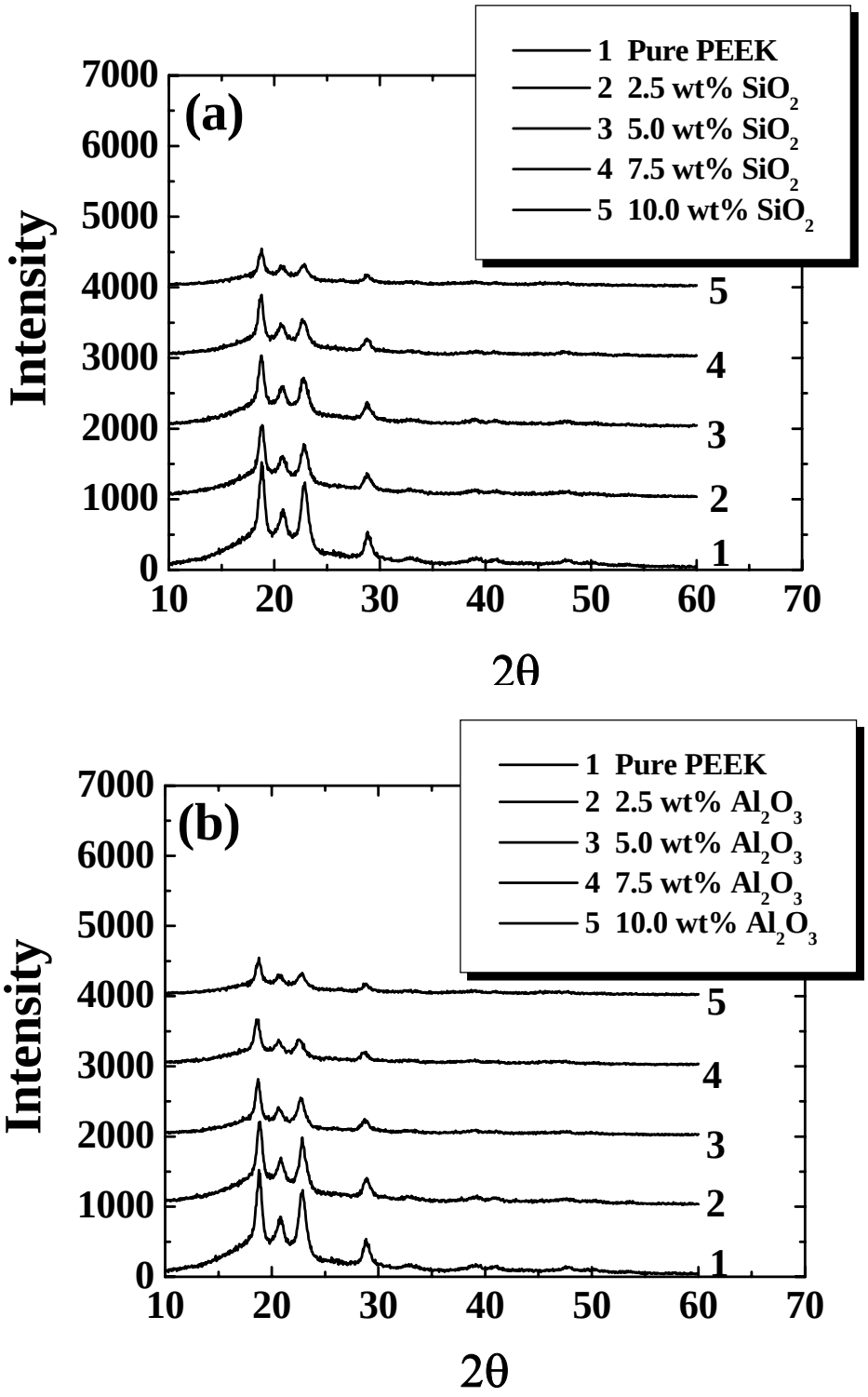

Fig. 3.32 X-ray diffraction patterns of the PEEK nanocomposites filled with 30 nm (a) SiO_2 and (b) Al_2O_3 particles.

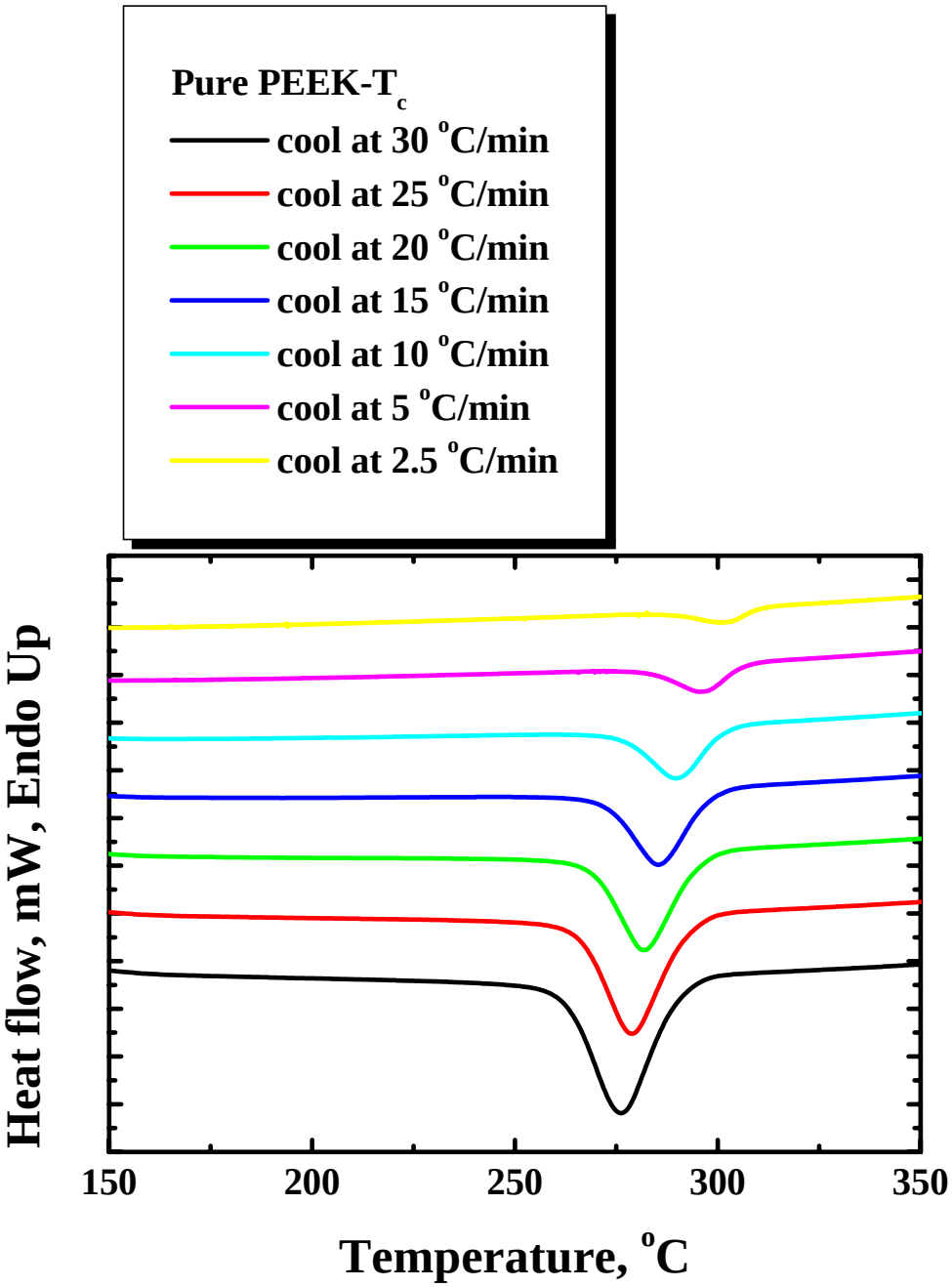

Fig. 3.33 DSC thermalgrams of the pristine PEEK during nonisothermal crystallization at different cooling rates.

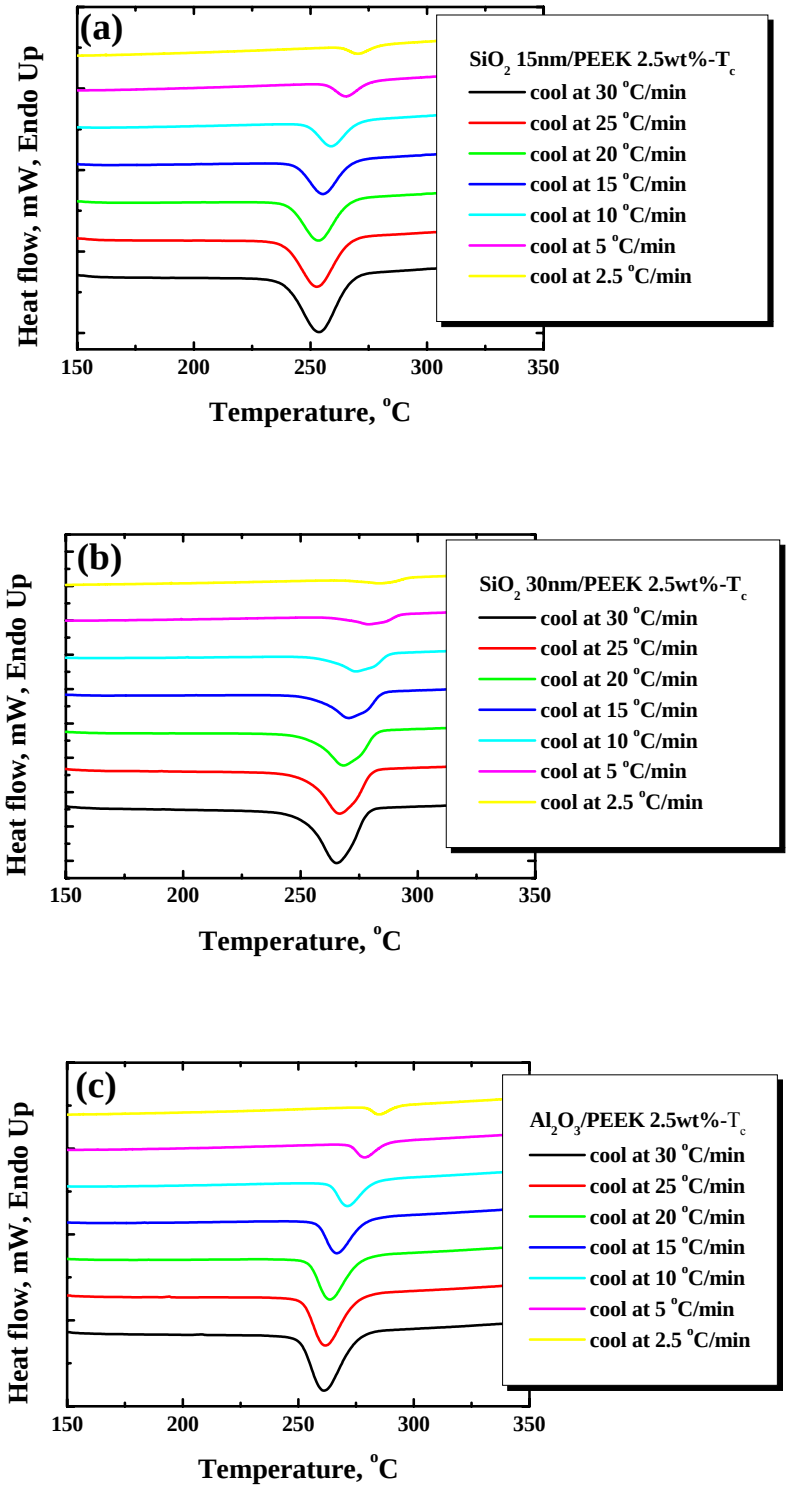

Fig. 3.34 DSC thermalgrams of the nanocomposites during nonisothermal crystallization at different cooling rates: (a) 2.5 wt% 15 nm silica/PEEK (b) 2.5 wt% 30 nm silica/PEEK, and (c) 2.5 wt% 30 nm alumina/PEEK.

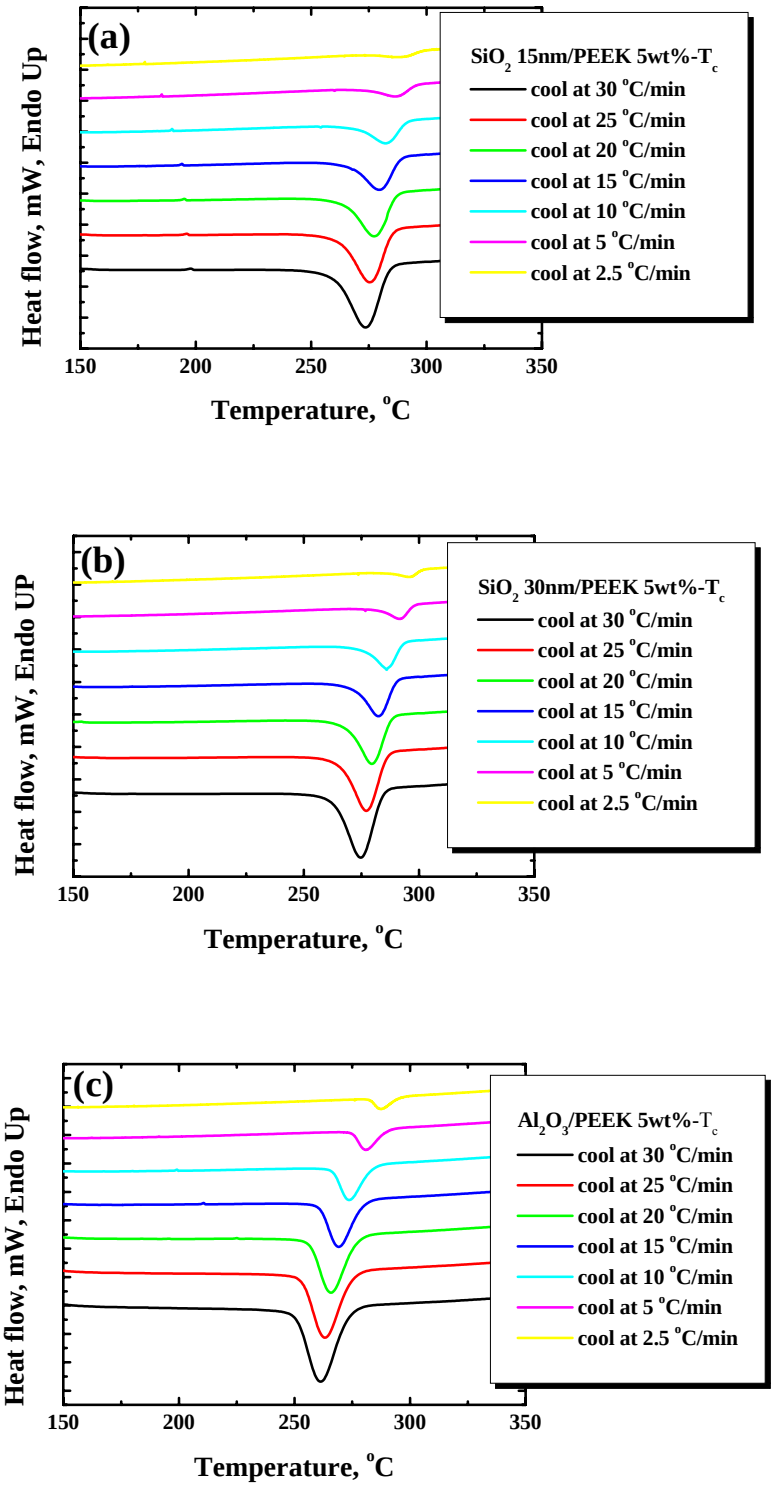

Fig. 3.35 DSC thermalgrams of the nanocomposites during nonisothermal crystallization at different cooling rates: (a) 5.0 wt% 15 nm silica/PEEK (b) 5.0 wt% 30 nm silica/PEEK, and (c) 5.0 wt% 30 nm alumina/PEEK.

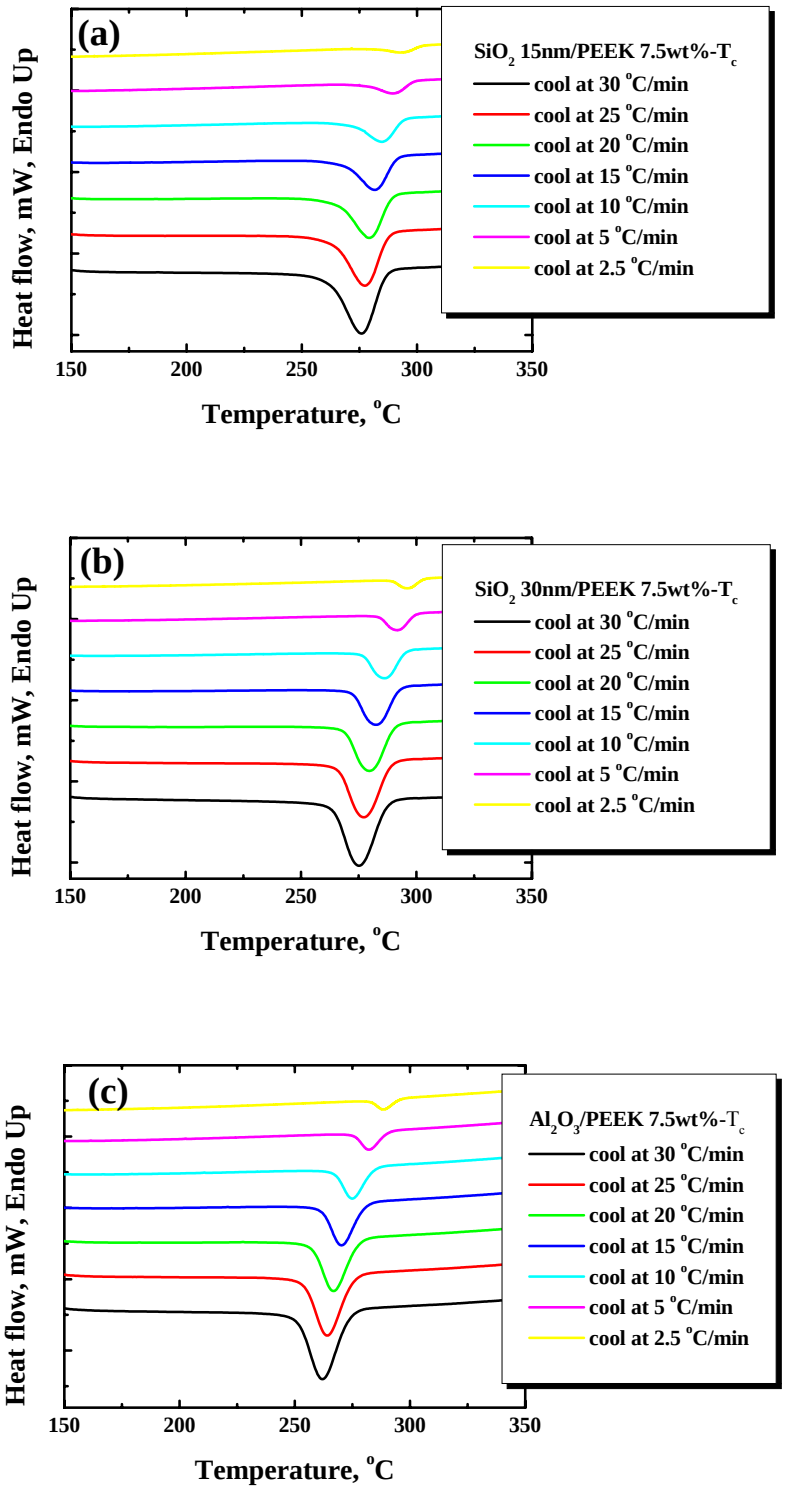

Fig. 3.36 DSC thermalgrams of the nanocomposites during nonisothermal crystallization at different cooling rates: (a) 7.5 wt% 15 nm silica/PEEK (b) 7.5 wt% 30 nm silica/PEEK, and (c) 7.5 wt% 30 nm alumina/PEEK.

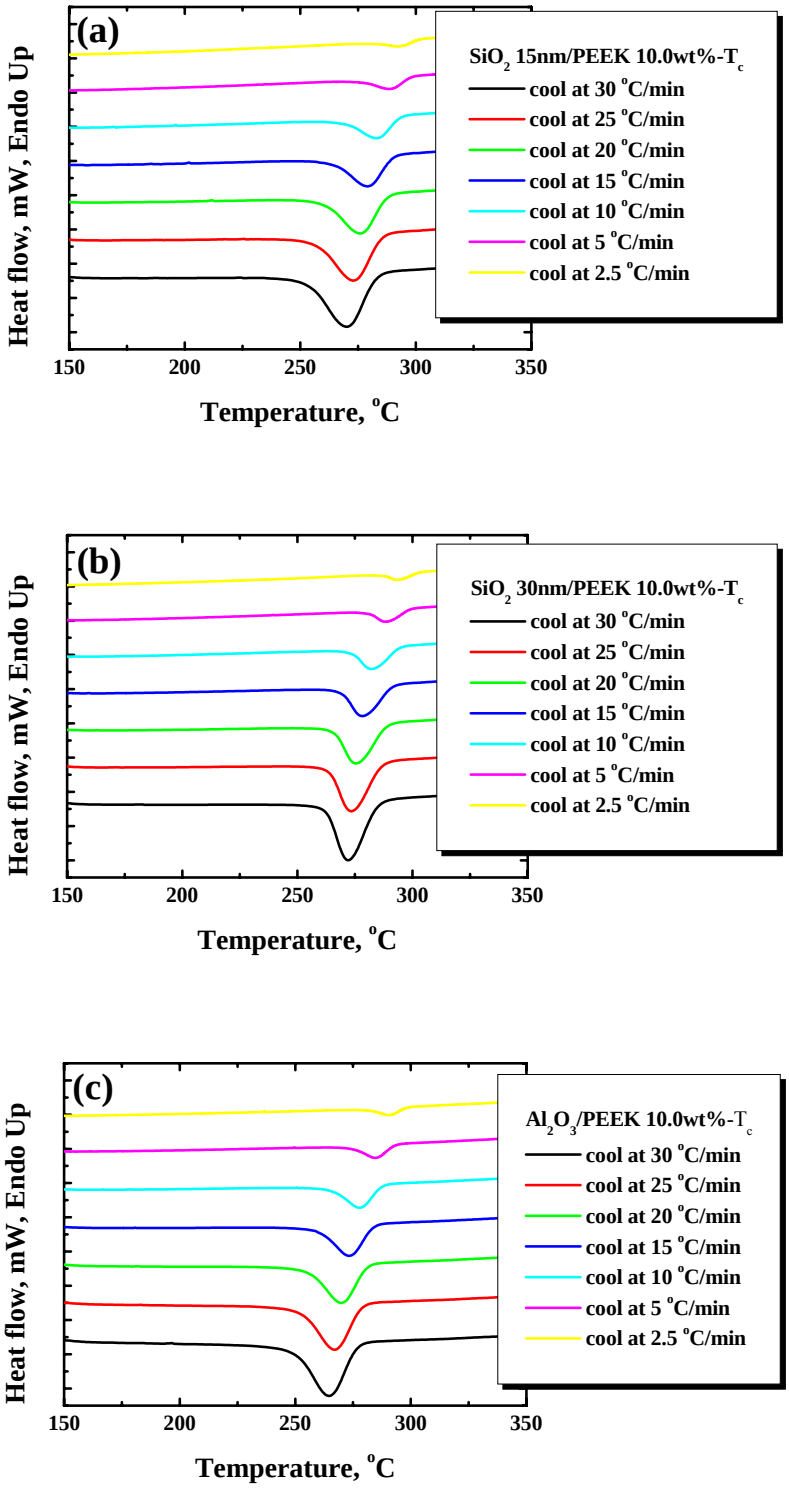

Fig. 3.37 DSC thermalgrams of the nanocomposites during nonisothermal crystallization at different cooling rates: (a) 10.0 wt% 15 nm silica/PEEK (b) 10.0 wt% 30 nm silica/PEEK, and (c) 10.0 wt% 30 nm alumina/PEEK.

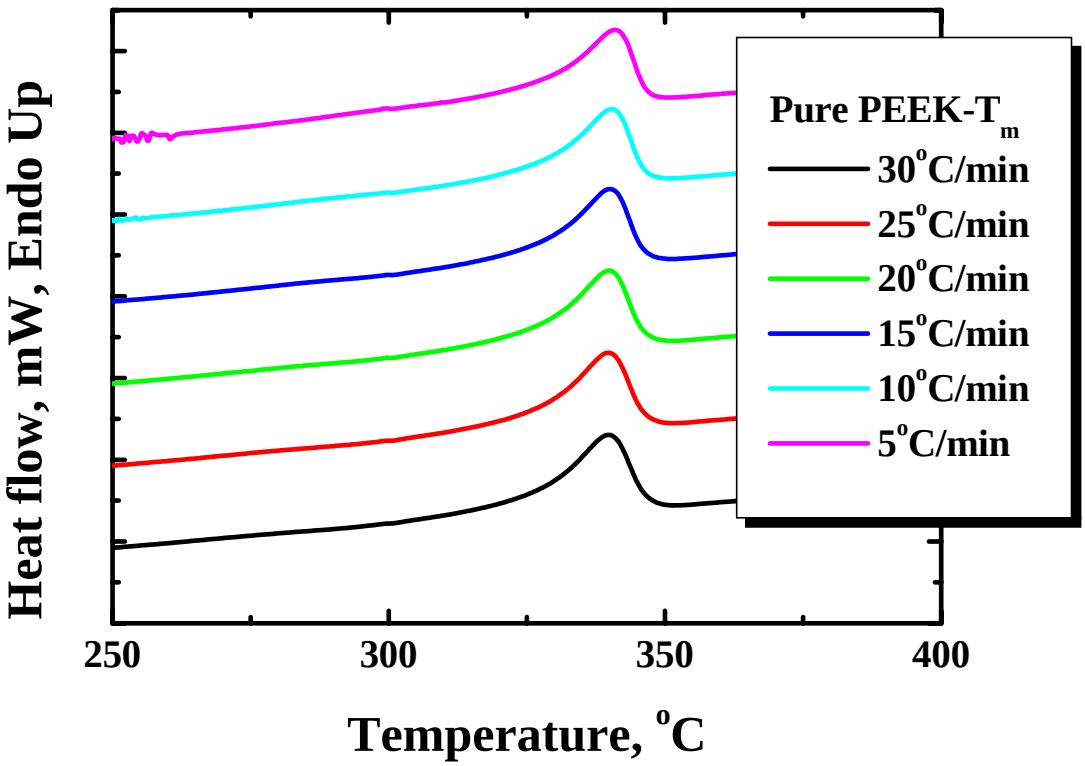

Fig. 3.38 DSC thermalgrams of pristine PEEK upon heating showing the melting peak. All the heating rates are 10 °C/min. Before heating up to 410 °C, the specimen was cooled from 410 to 50 °C at different cooling rates shown in the figures.

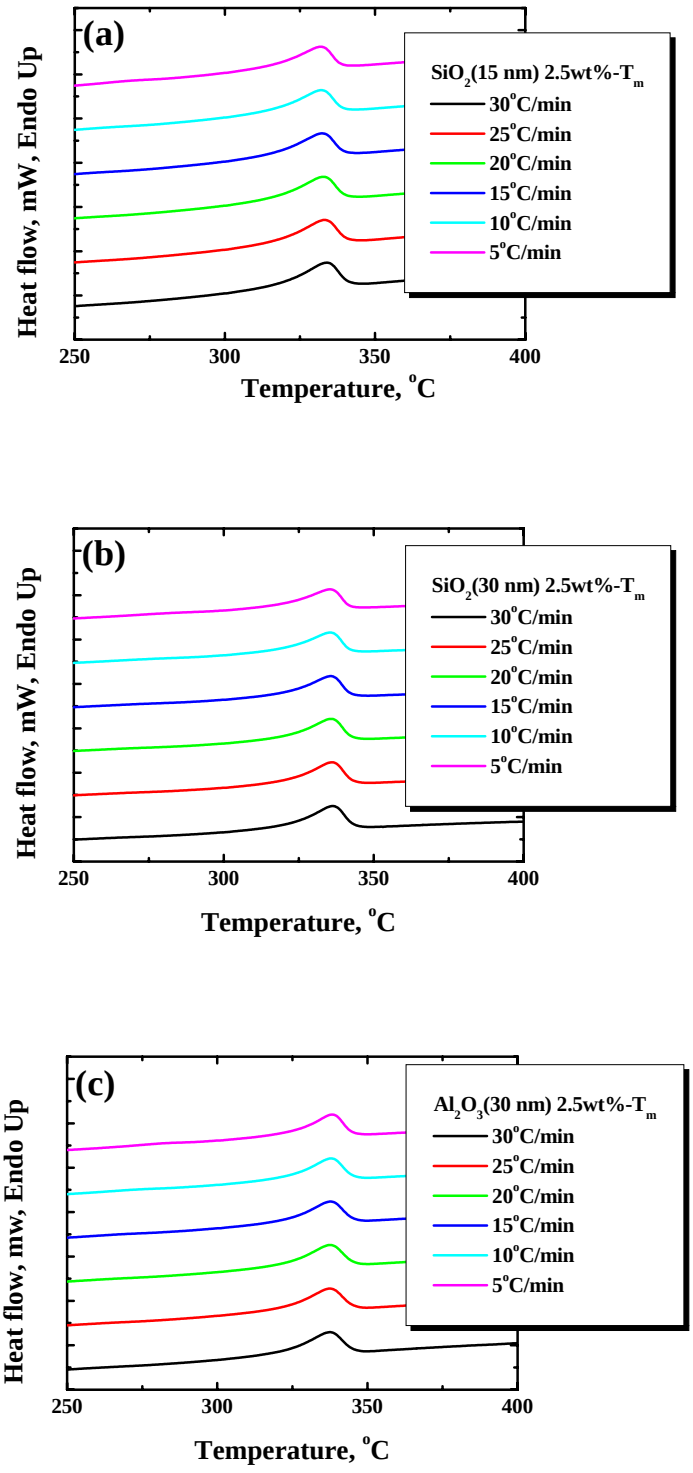

Fig. 3.39 DSC thermalgrams of the nanocomposites upon heating showing the melting peak: (a) 2.5 wt% 15 nm silica/PEEK, (b) 2.5 wt% 30 nm silica/PEEK, and (c) 2.5 wt% 30 nm alumina/PEEK. All the heating rates are 10 °C/min. Before heating up to 410 °C, all the specimens were cooled from 410 to 50 °C at different cooling rates shown in the figures.

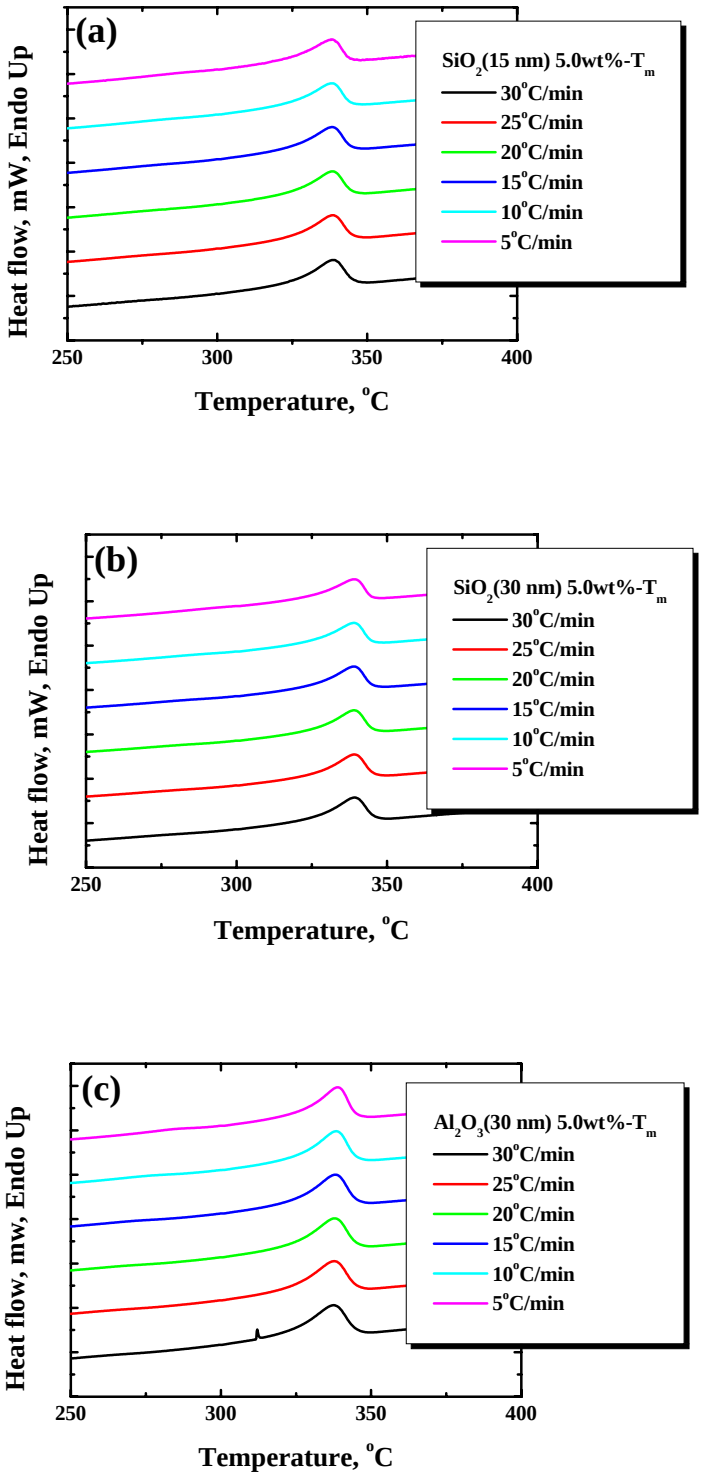

Fig. 3.40 DSC thermalgrams of the nanocomposites upon heating showing the melting peak: (a) 5.0 wt% 15 nm silica/PEEK, (b) 5.0 wt% 30 nm silica/PEEK, and (c) 5.0 wt% 30 nm alumina/PEEK. All the heating rates are 10 °C/min. Before heating up to 410 °C, all the specimens were cooled from 410 to 50 °C at different cooling rates shown in the figures.

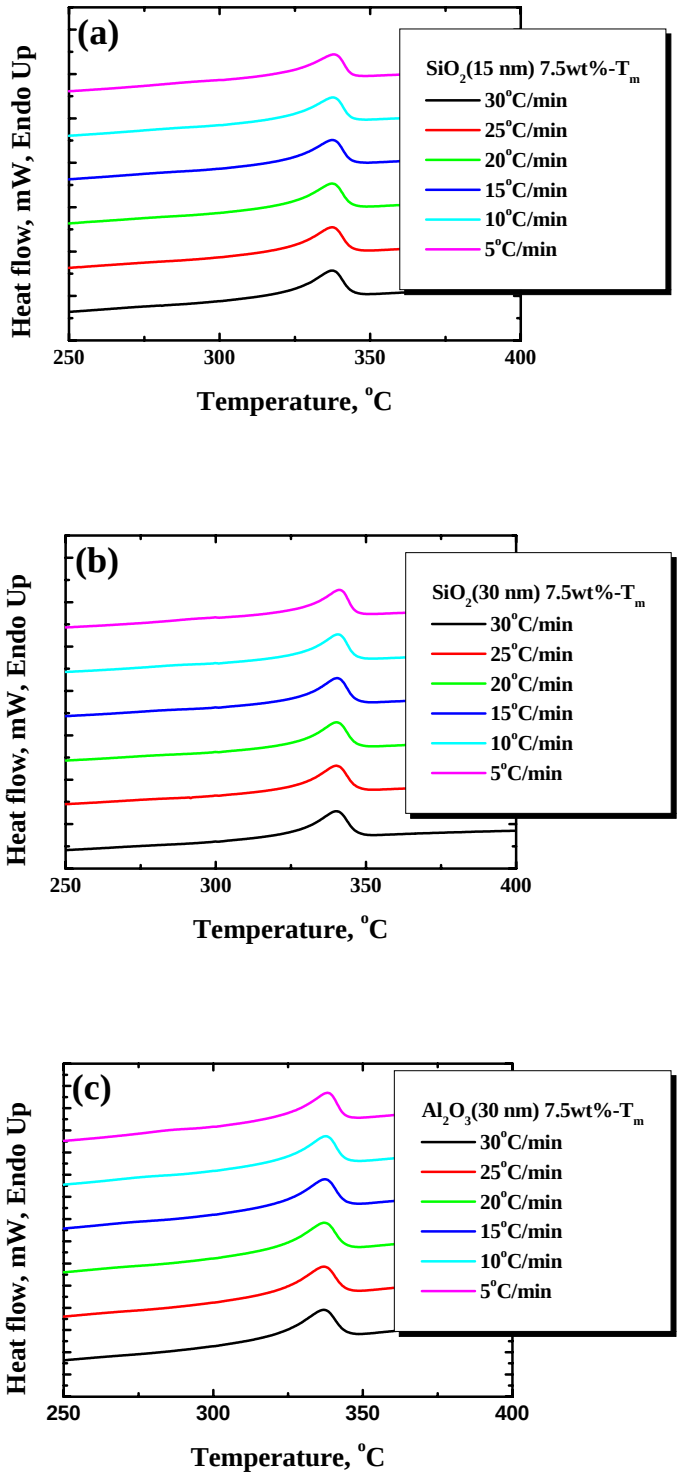

Fig. 3.41 DSC thermalgrams of the nanocomposites upon heating showing the melting peak: (a) 7.5 wt% 15 nm silica/PEEK, (b) 7.5 wt% 30 nm silica/PEEK, and (c) 7.5 wt% 30 nm alumina/PEEK. All the heating rates are 10 °C/min. Before heating up to 410 °C, all the specimens were cooled from 410 to 50 °C at different cooling rates shown in the figures.

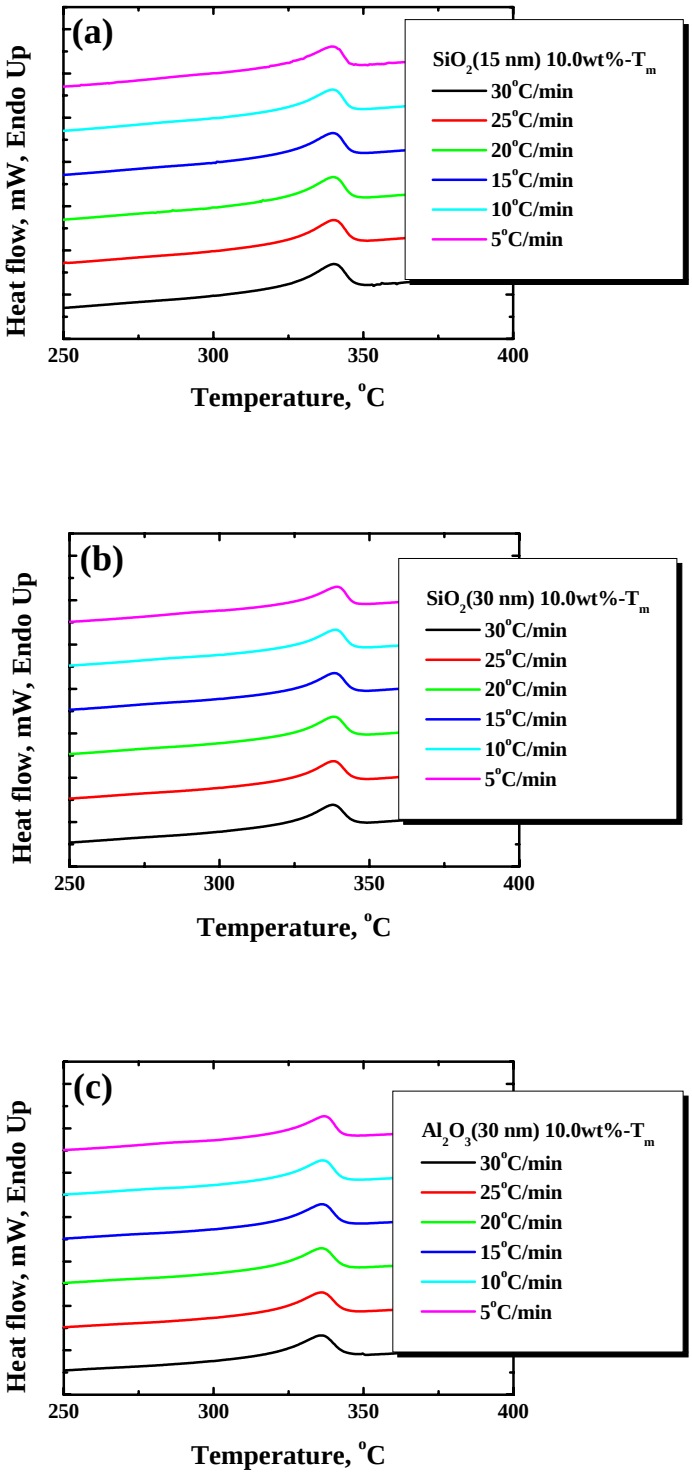

Fig. 3.42 DSC thermalgrams of the nanocomposites upon heating showing the melting peak: (a) 10.0 wt% 15 nm silica/PEEK, (b) 10.0 wt% 30 nm silica/PEEK, and (c) 10.0 wt% 30 nm alumina/PEEK. All the heating rates are 10 °C/min. Before heating up to 410 °C, all the specimens were cooled from 410 to 50 °C at different cooling rates shown in the figures.

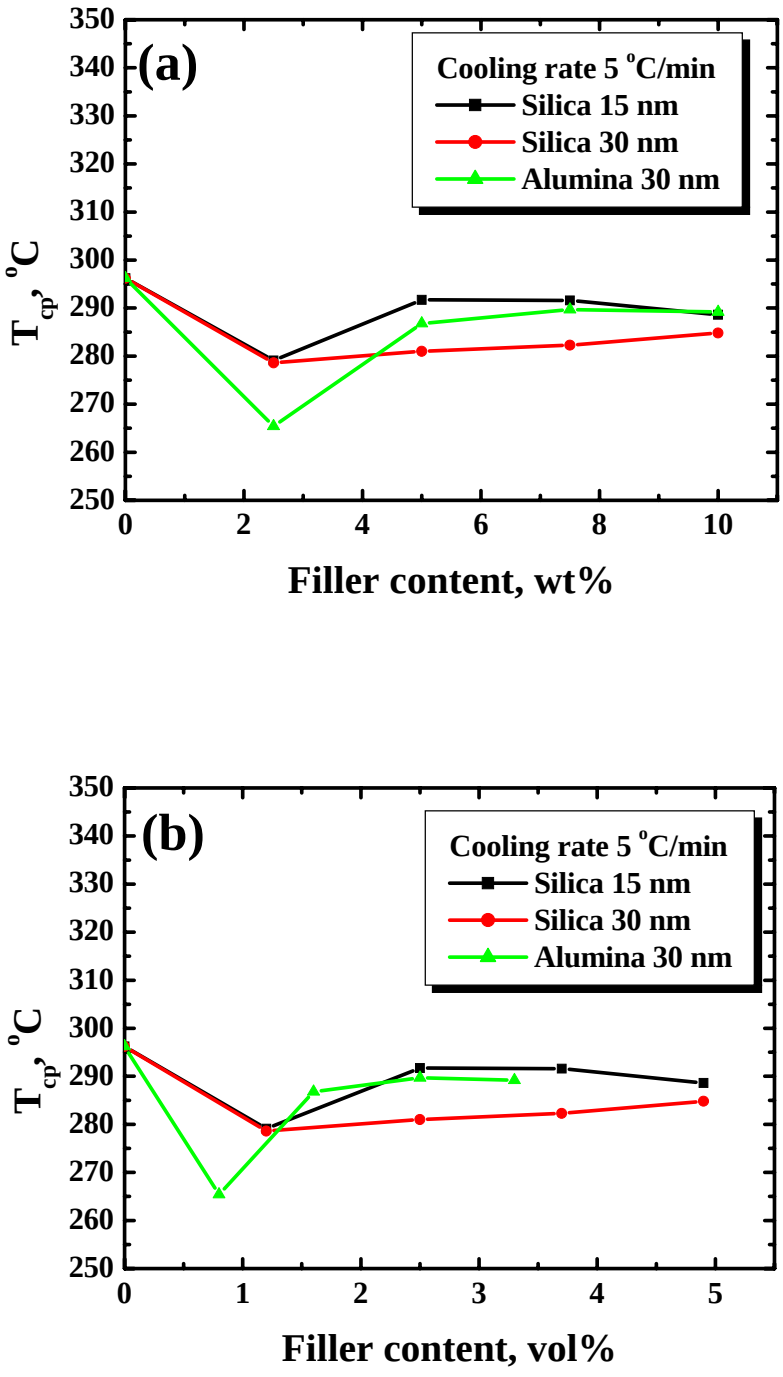

Fig. 3.43 The typical effect of filler content on peak crystallization temperature, T_{cp}, of PEEK nanocomposites at a cooling rate of 5 °C/min: (a) filler content in terms of weight percent, wt%, and (b) filler content in terms of volume percent, vol%.

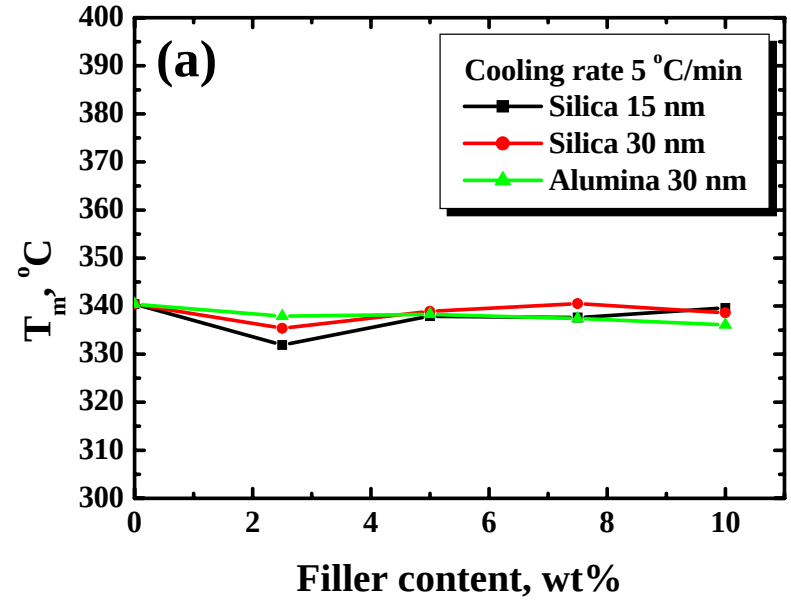

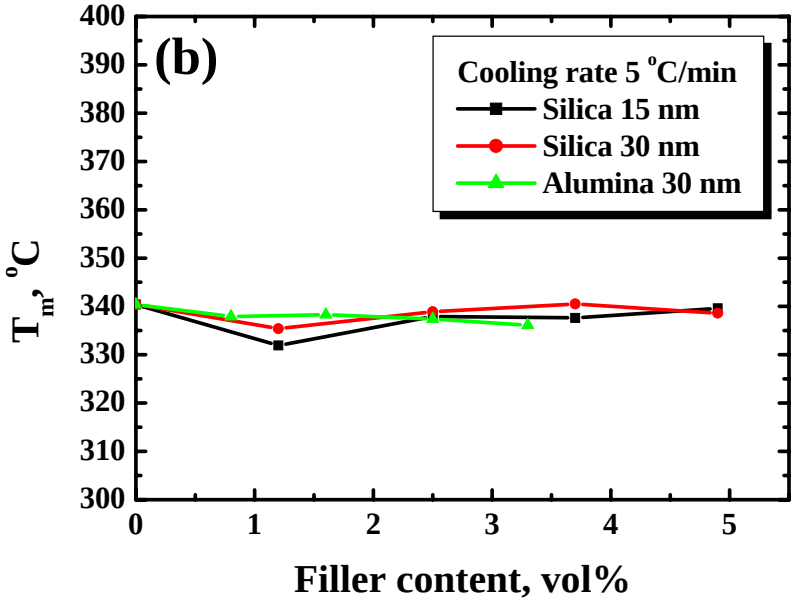

Fig. 3.44 The typical effect of filler content on melting temperature, T_m, of PEEK nanocomposites at a cooling rate of 5 ^oC/min: (a) filler content in terms of weight percent, wt%, and (b) filler content in terms of volume percent, vol%.

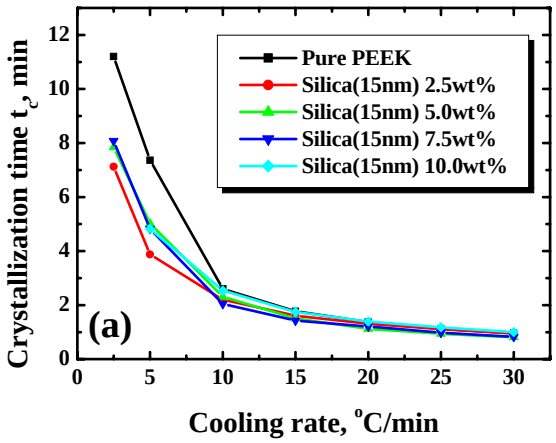

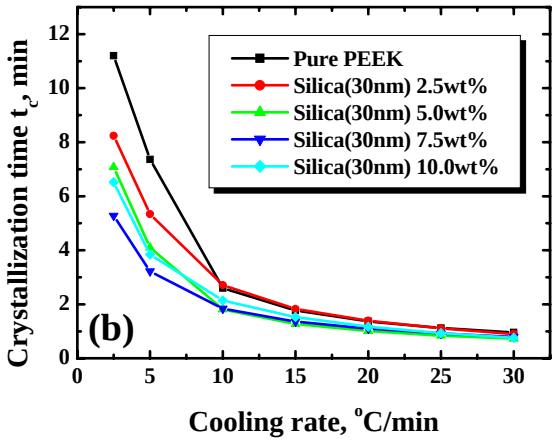

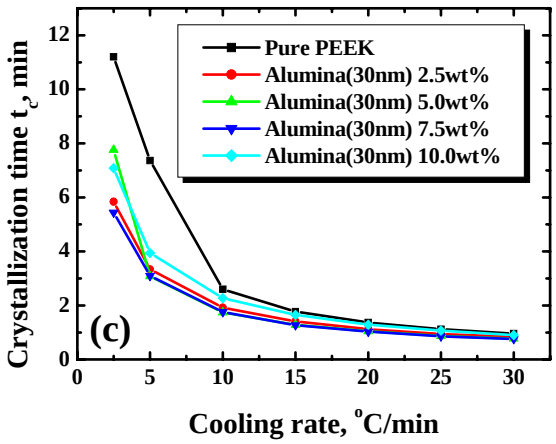

Fig. 3.45 Overall crystallization time versus filler content at various cooling rates: (a) 15 nm silica/PEEK, (b) 30 nm silica/PEEK, and (c) 30 nm alumina/PEEK.

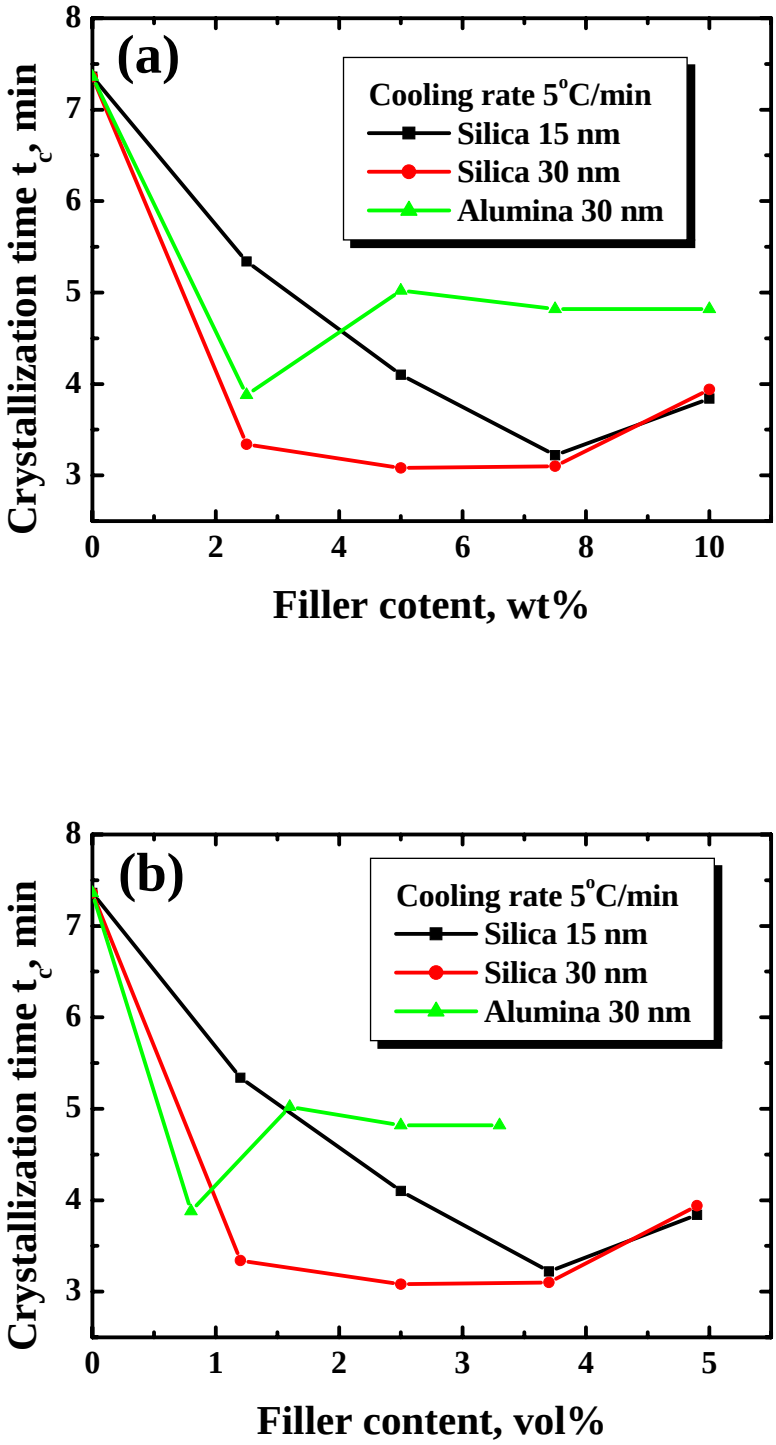

Fig. 3.46 The effect of filler content and dimension on the overall crystallization of the PEEK chain segments at a cooling rate of 5 °C/min: (a) filler content in terms of weight percent, wt%, and (b) filler content in terms of volume percent, vol%.

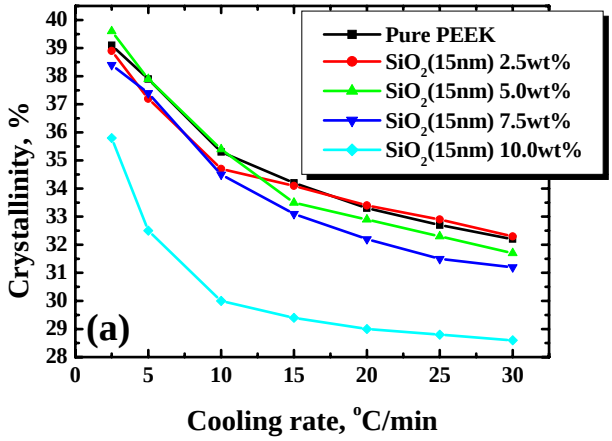

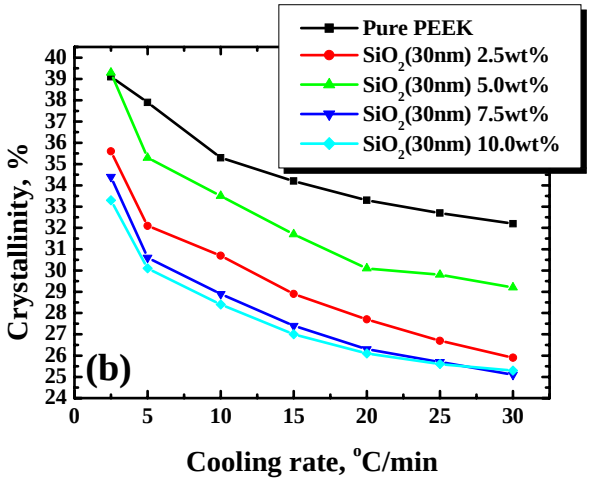

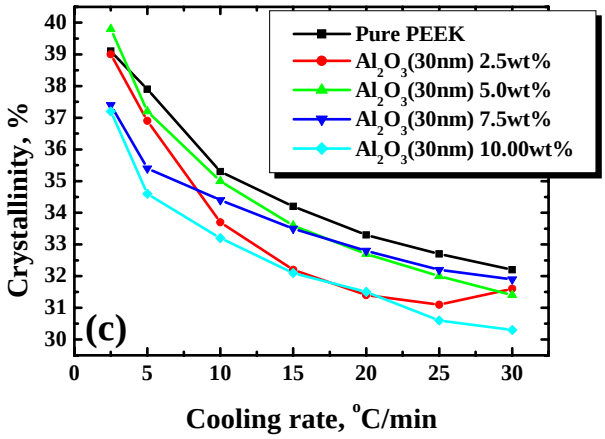

Fig. 3.47 Absolute crystallinity versus cooling rate: (a) 15 nm silica/PEEK, (b) 30 nm silica/PEEK, and (c) 30 nm alumina/PEEK.

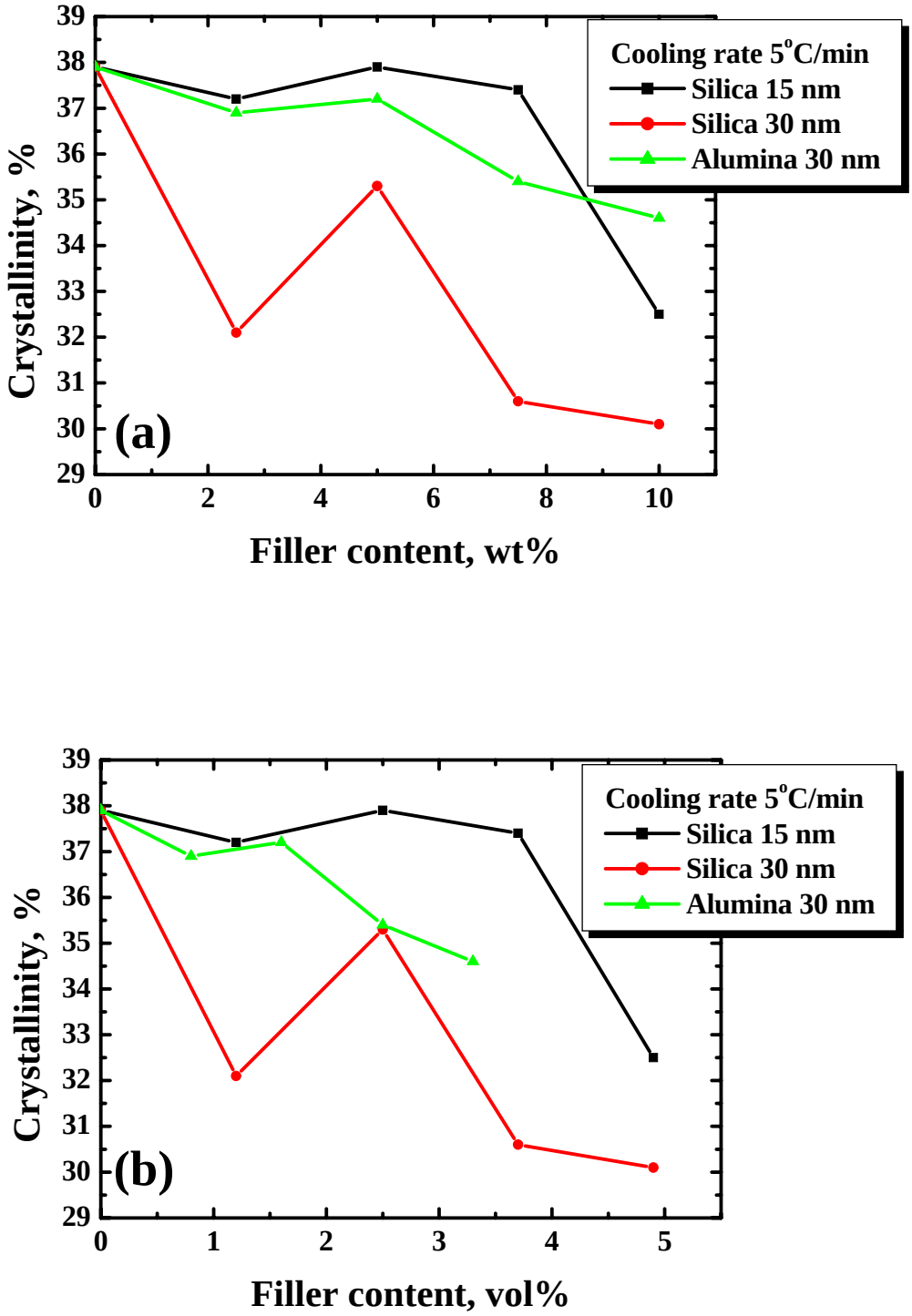

Fig. 3.48 The effects of filler content and dimension on the crystallinity of the PEEK chain segments at a cooling rate of 5 °C/min: (a) filler content in terms of weight percent, wt%, and (b) filler content in terms of volume percent, vol%.

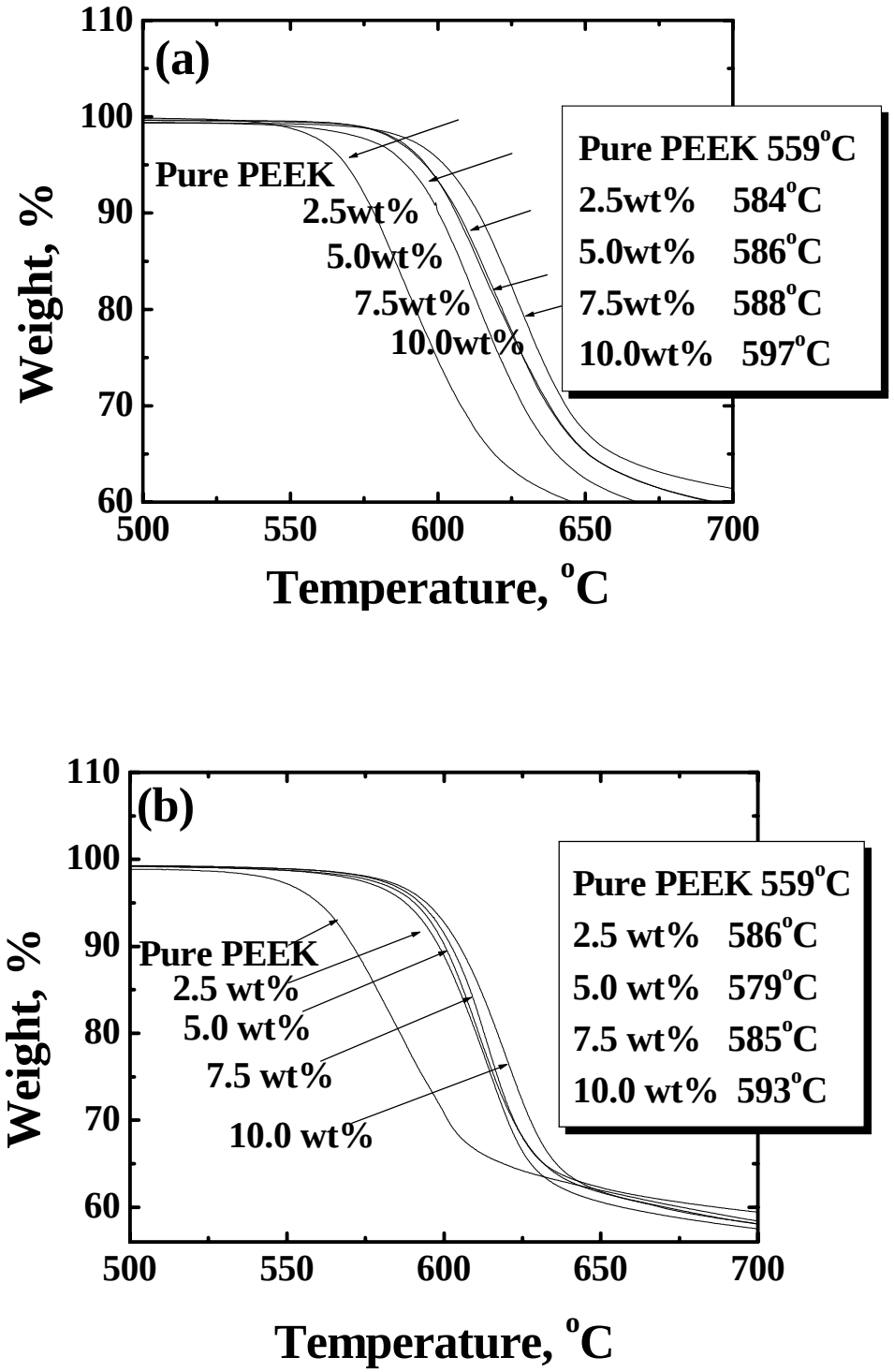

Fig. 3.49 The TGA diagrams of the PEEK nanocomposites filled with 30 nm (a) SiO_2 and (b) Al_2O_3 particles.